Magnetic Resonance Spectroscopic Imaging using Parallel Transmission at 7T

by

Borjan Aleksandar Gagoski

Electrical Engineering and Computer Science
Massachusetts Institute of Technology

Submitted to the Department of Electrical Engineering and Computer Science
in partial fulfillment of the requirements for the degree of

Doctor of Philosophy

at the

MASSACHUSETTS INSTITUTE OF TECHNOLOGY

February 2011

Author .....
Department of Electrical Engineering and Computer Science
January 21, 2011

Certified by .....
Elfar Adalsteinsson
Associate Professor of Electrical Engineering and Computer Science
Associate Professor of Health Sciences and Technology
Thesis Supervisor

Accepted by .....
Terry P. Orlando
Chairman, Department Committee on Graduate Students

Magnetic Resonance Spectroscopic Imaging using Parallel Transmission at 7T

by

Borjan Aleksandar Gagoski

Submitted to the Department of Electrical Engineering and Computer Science
On January 21, 2011, in partial fulfillment of the
requirements for the degree of
Doctor of Philosophy

Abstract

Conventional magnetic resonance spectroscopic imaging (MRSI), also known as phase-encoded (PE) chemical shift imaging (CSI), suffers from both low signal-to-noise ratio (SNR) of the brain metabolites, as well as inflexible tradeoffs between acquisition time and spatial resolution. In addition, although CSI at higher main field strengths, e.g. 7 Tesla (T), offers improved SNR over clinical 1.5T or 3.0T scanners, the realization of these benefits is limited by severe inhomogeneities of the radio frequency (RF) excitation magnetic field (B_1^+), which is responsible for significant signal variation within the volume of interest (VOI) resulting in spatially dependent SNR losses.

The work presented in this dissertation aims to provide the necessary means for using spectroscopic imaging for reliable and robust whole brain metabolite detection and quantification at high main field strengths. It addresses the challenges mentioned above by improving both the excitation and the readout components of the CSI acquisition. The long acquisition times of the PE CSI are significantly shortened (at least 20 fold) by implementing the time-efficient spiral CSI algorithm, while the B_1 non-uniformities are corrected for using RF pulses designed for new RF excitation hardware at 7T, so-called parallel transmission (pTx). The B_1 homogeneity of the pTx excitations improved at least by a factor of 4 (measured by the normalized spatial standard deviations) compared to conventional single channel transmit systems.

The first contribution of this thesis describes the implementation of spiral CSI algorithm for online gradient waveform design and spectroscopic image reconstruction

with standard clinical excitation protocols and applied in studies of Late-Onset Tay-Sachs (LOTS), adrenoleukodystrophy (ALD) and brain tumors.

A major contribution of this thesis is pTx excitation design for CSI to provide spectral-spatial mitigation of the B_1^+ inhomogeneities at 7T. Novel pTx RF designs are proposed and demonstrated to yield excellent flip angle mitigation of the brain metabolites, and also enable improved suppression of the undesired water and lipid signals.

A major obstacle to the deployment of 7T pTx applications for clinical imaging is the monitoring and management of local specific absorption rate (SAR). This thesis also proposes a pTx SAR monitoring system with real-time RF monitoring and shut-off capabilities.

Thesis Supervisor: Elfar Adalsteinsson

Title: Associate Professor of Electrical Engineering and Computer Science
Associate Professor of Health Sciences and Technology

Acknowledgements

I'm done with my PhD. I have closed a chapter of my life which would not be possible without the support of many individuals. The least I can say is that, so far in my life, I have been surrounded with amazing people that enabled me to prosper in every aspect of my life. Here, albeit in only few lines, I try to give out my sincere gratitude to those who have helped me reach the biggest accomplishment of my life to this date.

Elfar Adalsteinsson - my research advisor. His style of work, his guidance, his patience, his way of dealing with issues and his insights (i.e. his "sixth sense") on all the things I encountered (not just in research, but in general), could not have been better in any other advisor that I would have had. While his technical competence and advising is pristine, what is more important is his amazing way of motivating his students. Every week when I had a meeting with him, I came out of his office ready and eager to tackle a problem starting right then, at that moment. He also had great belief in me, at times here at MIT, when I seriously doubted myself. He literally "raised my from the dead", and made a better person in every way possible. The amount of gratitude I cannot express in words. I am convinced that we are going to have a life-long friendship, and I cannot be thankful enough for that fact.

Larry Wald and Polina Golland – members of my PhD committee. Larry, in a way, has been my unofficial co-advisor. While working on the parallel transmission project, I have been having meetings with him regularly. He is undoubtedly one of the greatest minds in his field, and I was honored to work with him. Furthermore, as a remarkable presenter, his comments on all of my oral and written presentations had significantly improved my presentation skills, and I am thankful for that. I would like to thank Polina for her willingness to be on my committee and spent some of her precious time learning about my work. I greatly appreciate all her comments and great attitude throughout the past three years.

My working environment and surroundings were great. The lab groups at MIT and MGH consist of these great people, who are not highly intelligent and smarter than me, but also make me laugh on a daily basis. Kawin and VJ have introduced me to the parallel transmit project, and have warmed me about the "evil ghosts of Bay5", that prevent robust scanning (they were/are right!). Joonsung and Khaldoun have been there with me in Bay5, trying to debug the pTx system, and were great company in the long hours spend at the system. When not in Bay5, I enjoyed the time in the lab with Div, Berkin, Trina, Audrey, Lohith, Padraig, Adam, Dan, Jessica, Christin. I could not ask for nicer and more fun labmates to spend my time with - chatting about MR, or making me smile for random things. Somewhere in between Bay5 and the MIT lab, I was also surrounded by interesting people from Larry's group, working over at Charlestown. Jon, Thomas, Azma, Boris, Christina, Jen, Julien, Veneta and Wei are tremendous individuals and I enjoy having them around. I won't tell the stories here. Here, I would also have to mention the great support that I have received from Siemens employees, particularly Michael, Josef, Ulrich, Franz, Himanshu and Philipp.

Outside school, I have enjoyed most of my free time with MIT crowd or with the Balkan's community in the Boston area. I have known Demba, Zahi, Alex, Obrad, Cathal, Rory, Conor, Andrej, Carlos, ... for years know, and I can not say that I have met more fun people to be around. From time spending in bars, to going to ski trips - it was always a blast, and the time I spent with them made me realize how much these smart people are down to earth, and great to be around. The Balkan's crowd living in Boston area have helped me feel more like home. I am very grateful that I have Beti, Vlatko, Marija, Filip, Adri, Iva (and Jason), Kate (and Steve), Nikola, Sinisha (I am forgetting somebody, I know) as my life-long friends, who always crack me up, and make me relax after the though hours spend in the lab and Bay5.

I could not go without mentioning my friends who I grew up with, back in Macedonia. They define me who I am, my personal character, my way of looking at life. They will always have place in my home wherever I end up living. I am certain that I will have Vaso, Sneze, Gogo, Maja, Kico, Filjo, Tanja, Leko, Eci, Fiki ... as friends for life, and I feel so fortunate about it. Багра, турава од мене ;).

My family has played a tremendous role in my success in life so far. My parents: Lidija i Aleksandar have shown me how parents should love and care for a child, and I only hope I am as good of a parent as they are to me. They have never pushed me to do

anything, yet they have always guided me in life, but me being the one making the decisions. They had faith in me throughout the years, even when I was sent to US at the age of 18 for my studies. I thank them, and love them endlessly, and I am looking forward to being even better grandparents. Also, I would like to thank all the other family members back in Macedonia, as well as the ones that are currently in the US: Mare, Ivan, Aleks, Igor, Ane, Maja, Talija and Kalina.

Last, by certainly not the least, I want to thank my wife-to-be Lepka for all her love and support in the past few years. I am looking forward to the times when we will substitute "skype" with "living together" (happy) (h) (blush). I love her truly and sincerely, and I have not been more certain in my life that I have found the girl of my life. It just feels great. I can't wait to start spending my life with her, somewhere on this Earth, traveling, being happy, and understanding each-other without saying a word ... Зелче, мече, близначе најмое ;)

Watch out world, I am coming.

"Every time I realize how dumb I am, I get smarter"

Borjan A. Gagoski

Cambridge, Massachusetts, USA

THIS PAGE INTENTIONALLY LEFT BLANK

Contents

List of Figures

List of Tables

THIS PAGE INTENTIONALLY LEFT BLANK

Chapter 1

Introduction

1.1 Motivation

Magnetic Resonance Imaging (MRI) is an imaging modality that enables high quality, non-invasive visualization of soft tissue in the human body. In addition to diagnostic imaging with structural MRI, the modality also offers possibilities for monitoring biochemistry *in vivo*. Magnetic Resonance Spectroscopic Imaging (MRSI), also known as chemical shift imaging (CSI) is a technique which obtains spectra of signals, e.g. brain metabolites, from each spatial location of interest. Detection of these signals is based on the MR phenomenon of chemical shift - a subtle frequency shift in the spectrum that depends on the chemical structure of particular compound. Quantitative measure of the amount of these metabolites, including: N-acetyl-L-aspartate (NAA) – a neuronal marker, creatine (Cr) – one of brain's energy suppliers, choline (Cho) – an essential nutrient, or lactate – glycolysis's end product, has great impact in medicine for diagnosing and better understanding of many brain pathologies. For example, deficiency in the amount of NAA is strongly correlated to the presence of a neurodegenerative disease, like the Alzheimer's disease [1-4], multiple sclerosis [5-7], adrenoleukodystrophy (ALD) [8-10], etc. Furthermore, besides a NAA deficiency, the presence of certain types of brain tumor is strongly linked to increased choline levels [11-13], while lactate and lipid resonances are typically found in high-grade gliomas [14-

15]. Increased lactate levels are indicators of abnormal metabolism caused by ischemia [16], and are also reported in stroke [17-19]. Metabolite quantities in general could be abnormal in post-stroke brain tissue [20-22], as well as in some neuropsychiatric disorders [23]. Review papers, like [24-26], give a more detailed survey on spectroscopic imaging, and the role of the brain metabolites in medical diagnosis.

The dominant challenge of proton (^{1}H) CSI as a technique, is the fact that it is inherently hindered by low SNR of the metabolites of interest due metabolite concentrations on the order of 1-10 mM [26-28]. This is in contrast with structural MRI, where water is the primary signal source at ~50M concentration, which for conventional clinical field strengths enables fast scan times (~minutes) and high resolution (~mm), whereas spectroscopic imaging scan times are on the order of 10s of minutes for spatial resolution on the order of 1cm. Beyond the SNR limitations, the much higher concentrations from lipids and water pose problems in practical spectroscopic imaging [29-30]. For instance, spectra at spatial locations near fat tissue suffer from strong lipid contamination that poses significant difficulties to metabolite detection and estimation as the lipids peaks resonate close in frequency to, e.g. the important NAA peak in the brain. Therefore, metabolite detection and estimation requires CSI acquisitions that effectively suppress the strong water [31-32] and lipid [33-37] signals.

SNR in MRI is proportional to the strength of the main field (B_0), the square-root of acquisition time, and the voxel size [38-39]. Thus, an obvious means to improved SNR in CSI without resolution or imaging time tradeoffs is the use of high-field scanners. However, imaging at high field suffers from severe inhomogeneities of the radio-frequency (RF) excitation magnetic field (B_1^+), that manifest as undesired non-uniform spatial SNR distribution and image contrast [40-42]. Moreover, conventional phase-encoded (PE) CSI [30, 43] suffer from long acquisition times that are impractical for volumetric metabolite mapping of spatial resolution supported by the underlying metabolite SNR.

The motivation for this thesis is the development of MRI methodology to overcome these limitations in order to make high field, whole brain CSI clinically more available as a practical and useful tool. To this end, excitations for CSI need to provide uniform spectral-spatial excitation targets of the brain over frequency bandwidth of the metabolites of interest, as well as effectively suppress undesired and interfering water and lipid signals. For signal encoding, the inflexible tradeoffs among acquisition time and

spatial resolution intrinsic to PE CSI need to be overcome, so that volumetric, high resolution whole brain *in vivo* CSI becomes a clinical reality.

1.2 Thesis outline and contributions

In what follows, I present the chapter-by-chapter organization of this dissertation. Chapters 2 and 4 serve as background presentations of material that facilitates the description of the intellectual contributions of this thesis.

Chapter 2, entitled "*Background: Magnetic Resonance Spectroscopic Imaging*", gives a brief overview of the theory and the common acquisition methods of a typical chemical shift imaging (CSI) experiment. This discussion is largely separated into readout and excitation segments, each presenting the most commonly used techniques for current clinical CSI. In addition to this, it also introduces improvements in each of these segments. For example, the concept of time-varying readout gradients is discussed as a way to improve time-efficiency and short CSI acquisition times.

Chapter 3, entitled "*Spiral Spectroscopic Imaging at Clinical Settings at 3T Systems*", presents the spiral CSI algorithm in more details and lists its advantages and tradeoffs. It then presents spiral CSI implementation using the Integrated Development Environment for Applications (IDEA®), which is the Siemens software for custom sequence development. This work has resulted in a Work-In-Progress (WIP) package, which is a mechanism by which Siemens distributes MR software to other research institutions and sites. The use of this package as a tool for the study of LOTS (Late Onset Tay-Sachs) and brain tumors is illustrated. This work has produced the following papers:

- *B. Gagoski*, E-M. Ratai, F. Eichler, G. Wiggins, S. Roell, G. Krueger, J. Lee, and E. Adalsteinsson. 3D Volumetric *In Vivo* Spiral CSI at 7T. In *Proc. Int. Soc. for Magnetic Resonance Imaging (ISMRM)*, page 635, Berlin, Germany, 2007. (submitted)
- *B. Gagoski*, M. Hamm, J. Polimeni, G. Krueger, E-M. Ratai, G. Wiggins, U. Boettcher, J. Lee, F. Eichler, S. Roell and E. Adalsteinsson. Volumetric Chemical Shift Imaging with 32-Channel Receive Coil at 3T with Online Gridding

Reconstruction. In *Proc. Int. Soc. for Magnetic Resonance Imaging (ISMRM)*, page 1608, Toronto, Canada, 2008. (submitted)

- *B. Gagoski*, E-M. Ratai, B. P. Schmidt, E. Adalsteinsson and F. Eichler. 3 Tesla spiral CSI in Late Onset Tay Sachs reveals supratententorial changes in brain metabolism. *Submitted to the 19th Annual Meeting of the Int. Soc. for Magnetic Resonance Imaging (ISMRM), Montreal, Canada, 2011.*
- *B. Gagoski, O. Andronesi,* E. Adalsteinsson and G. Sorensen. Clinical 3D MR Spectroscopic Imaging Using Low Power Adiabatic Pulses and Fast Spiral Acquisition (In preparation for submission to Journal of Radiology)

Chapter 4, entitled "*Background: Acquisitions on 7T Parallel Transmit (pTx) System*", introduces the concept of parallel transmission using multiple RF power amplifiers that can simultaneously play more than one RF waveform, as an efficient way to mitigate B_1^+ inhomogeneity problems at 7T. Furthermore, it describes the data collection process on our 7T parallel transmission (pTx) platform. The main objective of this chapter is to list and fully describe all the necessary steps that are involved in a typical pTx experiment, which when compared to a standard single-channel system, is much more involved in every possible way (from RF pulse designs to patient's safety), particularly in the current early phase of the implementation of this novel technology. The chapter briefly describes B_1^+, B_1^-, and B_0 mapping, followed by the RF pulse design, and ends with the methods for estimation and modeling of the specific absorption rate (SAR).

Chapter 5, entitled "*Real time RF monitoring in a 7T pTx systems*" focuses on the development of the hardware and software methods needed to monitor all the RF waveforms that are simultaneously played during every pTx acquisition in real time. The main purpose of this tool was to instantaneously (~10 ms reaction time) stop the scan if the mismatch between the ideal and measured RF waveforms exceeds the given threshold criterion. The importance of being able to detect these transmission (e.g. broken coil, or other spurious sources of pTx RF errors) or subject related mishaps (e.g. movement changes the loading of the coil), is the fact that any variations in RF waveforms may violate the estimate of the previously simulated local SAR map, and therefore pose concerns related to patient safety. This work resulted in these papers:

- *B. Gagoski*, R. Gumbrecht, M. Hamm, K. Setsompop, B. Keil, J. Lee, K. Makhoul, A. Mareyam, T. Witzel, U. Fontius, J. Pfeuffer, E. Adalsteinsson and L. Wald. Real time RF monitoring in a 7T parallel transmit system. In *Proc. Int. Soc. for*

Magnetic Resonance Imaging (ISMRM), page 781, Stockholm, Sweden, 2010 (submitted)

- *B. Gagoski,* H. Bhat, M. Hamm, P. Hoecht, K. Makhoul, J. Lee, K. Setsompop, L.L. Wald, E. Adalsteinsson. Threshold criteria for real time RF monitoring in 7T parallel transmit system. *Submitted for the 19th Annual Meeting of the Int. Soc. for Magnetic Resonance Imaging (ISMRM), Montreal, Canada, 2011*

Chapter 6, entitled "*7T parallel transmit (pTx) spectroscopic imaging using wideband spokes excitation and pTx-optimized CHESS pulses*", describes RF designs for excitation and water suppression optimized for 7T parallel transmission using chemical shift imaging to mitigate excitation inhomogeneity over a 2-cm thick slice and a 600Hz spectral bandwidth. Water suppression precedes the excitation, and is performed with three spectrally-selective pTx RF pulses optimized for the 8-channel excitation array. The parallel excitation is then demonstrated with a spectroscopy phantom containing physiological concentrations of several major brain metabolites using single-slice, phase-encoded spectroscopic imaging (CSI) acquisitions. Furthermore, the parallel RF excitation is compared with conventional birdcage excitation with equally thick slice selection. The results demonstrate that for fixed imaging parameters, flip angle and excitation target, the parallel RF excitation outperforms the conventional excitation and provides superior spatial uniformity of the metabolites of interest. This work resulted in these papers:

- *B. Gagoski*, K. Setsompop, V. Alagappan, F. Schmitt, U. Fontius, A. Potthast, L. Wald and E. Adalsteinsson. Fast Spectroscopic Imaging Using Uniform Wideband Parallel Excitation on 7T. In *Proc. Int. Soc. for Magnetic Resonance Imaging (ISMRM)*, page 559, Toronto, Canada, 2008 (submitted)
- *B. Gagoski*, K. Setsompop, J. Lee, V. Alagappan, M. Hamm, A. vom Endt, L. Wald and E. Adalsteinsson. Spectroscopic Imaging Using Wideband Parallel RF Excitation at 7T. In *Proc. Int. Soc. for Magnetic Resonance Imaging (ISMRM)*, page 328, Honolulu, HI, USA, 2009 (submitted)

Chapter 7, entitled "*2-shot spectral-spatial parallel transmit excitation for 7T spectroscopic imaging using spiral trajectories*", shows novel methods for designing spectral-spatial RF pulses for simultaneous metabolite excitation *and* joint water/lipid suppression at our 7T eight channel pTx system using chemical shift imaging. More

specifically, the excitation target includes mitigation of B_1^+ inhomogeneities over a 2.5-cm thick slab and a 450Hz of spectral bandwidth. The desired 4-dimensional excitation profile is achieved by playing two spectral-spatial RF pulses in two separate averages with full metabolite SNR, followed by summation of the properly phased data from each average. The performance of the design is demonstrated on a spectroscopy phantom containing physiological concentrations of several major brain metabolites and three-dimensional spectroscopic imaging (CSI) acquisitions using spiral k-space trajectories to speed up the acquisition times. The 2-shot spectral-spatial 4-spoke parallel RF excitation was compared with 2-shot spectral-spatial birdcage equivalent design with equally thick slab selection. The chapter concludes that for fixed imaging parameters, flip angle and excitation target, the 4-spoke design variant outperforms the conventional birdcage excitation and provides superior spatial uniformity of the metabolites of interest, while achieving the same signal suppression over water and lipid frequencies. This work resulted in these papers:

- *B. Gagoski*, K. Setsompop, J. Lee, L. L. Wald and E. Adalsteinsson. 2-shot Spectral Spatial Parallel Transmit Spiral Spectroscopic Imaging at 7T. *Mag. Res. In Med*, in review, 2011. (submitted)
- *B. Gagoski*, K. Setsompop, J. Lee, L. L. Wald and E. Adalsteinsson. 2-shot spectral-spatial spokes excitation using spiral spectroscopic imaging on a 7T parallel transmit system. *Submitted for the 19th Annual Meeting of the Int. Soc. for Magnetic Resonance Imaging (ISMRM), Montreal, Canada, 2011.*

Chapter 8, entitled "*Summary and Recommendations*", summarizes the contents of this thesis and its contributions to the high field spectroscopic imaging community. It also projects possible directions of future research projects.

Dissertation structure: All the readers are assumed to have basic knowledge in MR physics, i.e. the complimentary interaction among the three fields used in every MR scanner: 1. the main magnetic (B_0) field; 2. The RF (B_1) field; 3. the linear gradients' fields (G_x, G_y, G_z). Several excellent texts describe the principles of MRI in detail [44-45]. Readers with limited knowledge in magnetic resonance spectroscopic imaging should definitely get familiar with the basic concepts presented in Chapter 2. Those clinically oriented, should focus their attention to the contents of Chapter 3, as it outlines examples of successful usage of the spiral CSI algorithm on clinical scanners at the Massachusetts General Hospital (Boston, MA). Chapter 4 is useful to the general MR

audience that wants to get familiar with all of what it takes to run a regular pTx acquisition. Although the contents of Chapter 5 are motivated and related to the last part of Chapter 4, the work presented is self contained, and can be understood without any prior reading. Lastly, pTx RF pulse designers will be mostly interested in the contents of Chapter 6 and 7.

Individually, each of the chapters are self contained, and can be read independently, without previously reading any of the others. Exception to this are Chapters 6 and 7 which don't include discussion about the field mapping techniques, and therefore, rely to some extent on the contents presented in Chapter 4.

THIS PAGE INTENTIONALLY LEFT BLANK

Chapter 2

Background: Magnetic Resonance Spectroscopic Imaging

Images of the human body generated using MRI are obtained in a two step process. Firstly, in the excitation phase, the hydrogen spins from particular spatial locations are excited using RF pulse(s), so that the MR signal is produced. In the readout phase, this signal is encoded using linear gradients in the three principal spatial axis (x, y and z), and after taking three dimensional (3D) inverse Fourier Transform (FT), the spatial contents of the tissue imaged can be observed. Further details on the basic physics of MRI, particularly about structural imaging, are given in [46], and will not be further discussed.

The aim of this chapter is to give the background behind the generation and encoding of the signals in a typical CSI experiment. We will immediately introduce the chemical shift phenomenon which is the basis for spectroscopic imaging. We will then reveal the disadvantages of the encoding scheme of the conventional PECSI, and introduce the sampling patterns of a fast CSI algorithm based on spiral-shaped k-space trajectories. At last, we will give overview of the excitation schemes commonly used in CSI, particularly focusing on the spectral aspects of the RF designs.

It is important to note that the work done in this thesis is dedicated on obtaining ^{1}H spectra of the human head, meaning that the spectra presented throughout the chapters span frequency bandwidths in the neighborhood of the resonance frequency of hydrogen (i.e. water). However, it is worth mentioning that ^{13}C [47] and ^{31}P CSI [48] is of significant importance. For example, ^{31}P spectra are used for obtaining quantitative information about chemical compounds like adenosine triphosphate (ATP), phosphocreatine (PCr), and inorganic phosphate (P_I) [49-50]. However, ^{13}C and ^{31}P spectra have significantly lower SNR compared to ^{1}H spectra and therefore are more difficult to detect and quantify. This is mainly because of lower abundance and sensitivity for these nuclei [51-52].

2.1 Chemical shift and the signal equation for CSI

Chemical shift as a MR phenomenon is defined as a subtle frequency shift in the signal that is dependent on the chemical environment of the particular compound. This small displacement of the resonant frequency is due to the shielding created by the orbital motion of the surrounding electrons in response to the main B_0 field. By placing a sample of biological tissue in a uniform magnet, exciting it, recording its free induction decay (FID), and then Fourier transforming the FID, the resultant MR spectrum shows resonances at different frequencies corresponding to different chemical shifts. It is this ability to distinguish different signals at different off-resonances that makes MRI capable of non-invasive physiological evaluation and material characterization of a given volume of interest.

In a presence of B_0, the effective field experienced by a nucleus as part of a certain molecular structure is defined as $B_{eff} = B_0 - B_{0\sigma}$. According to the Larmor relationship, ω is proportional to B_0, and therefore, we have that

$$\omega_{eff} = \omega_0 - \omega_{0\sigma} = \omega \cdot (1 - \sigma) \quad \textbf{(2-1)}$$

where σ equals the shielding constant that depends on the chemical environment, and therefore $\omega_{0\sigma}$ is the displacement of the resonance frequency. This alludes to a fact that is important in CSI, i.e. that *the change in frequency is proportional to the strength of the main magnetic field B_0.* This is the reason why when compared to lower fields, CSI at

higher B_0 further disperses the frequency axis, making the detection and estimation of the metabolites much easier.

For historical reasons, the frequency axis in CSI is, counterintiutively, drawn such that the frequency decreases from left to right and it is given in units of "parts per million", or ppm, relative to the frequency defined by the main field. This axis is centered on the resonant frequency of tetramethylsilane, which is not found in human tissues, but is a chemical that makes for a stable frequency marker in the presence of variations in temperature and acidity, and represents the 0 ppm point. The resonances of all the other molecular structures that are part of the 1H in vivo spectrum are therefore determined relative to this reference point. Note that ppm is a unitless entity and if one wants to convert the ppm axis in the units of Hertz (Hz), then 1ppm = $(\varphi/2\pi)\cdot B0\cdot 10\text{-}6$ Hz. Here, $(\varphi/2\pi)$ is the gyromagnetic ratio and is equal to 42.576 MHz ·T-1 for 1H imaging.

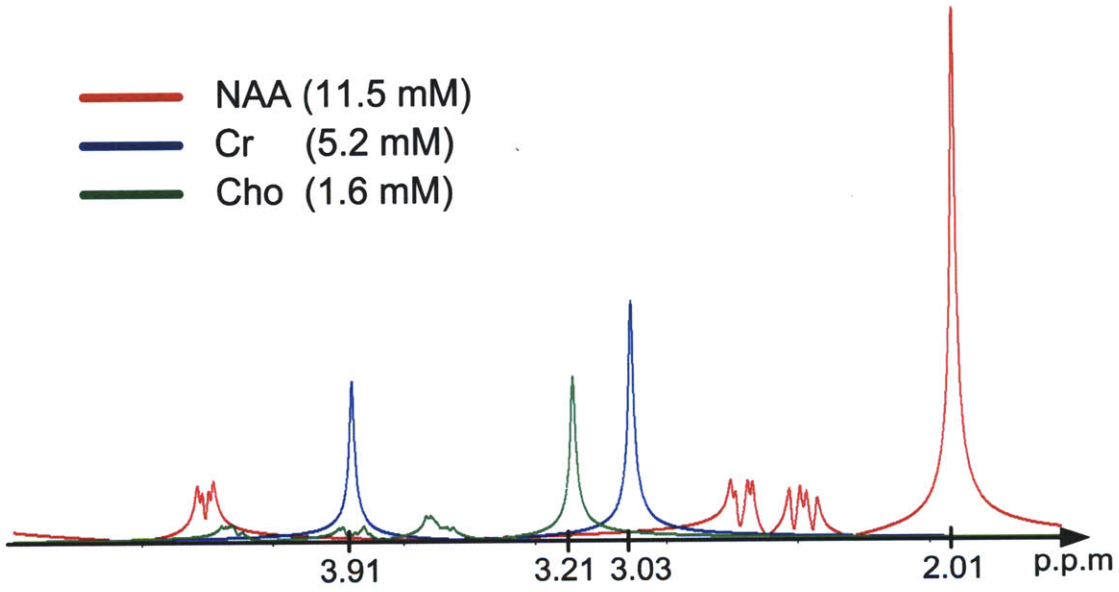

Figure 2-1: Simulated, noise-free 7T 1H MR spectra of the three dominant brain metabolites observed in vivo by proton spectroscopy: NAA, Cr and Cho showing the effects of the chemical shift phenomenon. Based on their chemical structure, different molecular structures experience different shielding, and therefore resonate at different frequencies. The nuclei that produce the main singlet of NAA experience different effective B_0 magnetic field compared two peaks of the Cr molecule.

Figure 2-1 shows simulated, noise-free 7T spectrum of the three important brain metabolites: N-acetyl-L-aspartate (NAA), creatine (Cr), and choline (Cho), using the SpinEvolution® software (Griffin Group, Department of Chemistry, MIT). The simulation was performed using physiological concentrations of these metabolites (11.5 mM for NAA, 5.2 mM for Cr, and 1.6 mM for Cho). Here we can see, for example, that most of

the NAA signal is concentrated in the singlet observed at 2.01 ppm. Creatine on the other hand, has two distinct peaks (singlets) located at 3.03 ppm and 3.91 ppm (referred to as Cr1 and Cr2, respectively). This means that compared to the hydrogen atoms found in the creatine molecule, the protons that are part of NAA's chemical structure experience less shielding. That is why the main peak of NAA deviates less from the reference frequency (i.e. 0 ppm) relative to the Cr peaks.

2.1.1 The signal equation for spectroscopic imaging

From what has been said in the last section, it is clear that CSI acquisitions, in addition to spatial encoding, need to also acquire samples as a function of time in order to obtain spectral information. To better explain the origins of the signals that are to be encoded, it is instructive to review the derivation of the signal equation for the case of spectroscopic imaging. The derivation presented followed closely that of Dwight Nishimura [45].

Leaving out the frequency axis for the time being, and considering only a three-dimensional (3D) space of interest, one can imagine a tiny "magnetic oscillator" rotating at frequency $\omega=\varphi B$ (φ is the gyromagnetic ratio and B is the main magnetic field) at each spatial location (x,y,z). Modeling these magnetic oscillators as having (constant in time) magnitude m(x,y,z) and (variable in time) phase $\phi(x,y,z,t)$, the signal seen by the receive coils, i.e. the transverse magnetization, is given by

$$\boldsymbol{s(t) = \iiint_{x,y,z} m(x,y,z) \cdot e^{-i\phi(x,y,z,t)}\, dx\, dy\, dz} \qquad \textbf{(2-2)}$$

Bearing in mind that frequency is the time rate of change in phase, and that it is proportional to the applied field B(x,y,z,t) one can write the following:

$$\boldsymbol{\phi(x,y,z) = \int_0^t \frac{d}{dt}\phi(x,y,z,\tau)d\tau = \int_0^t \omega(x,y,z,\tau)d\tau = \gamma \int_0^t B(x,y,z,\tau)d\tau} \qquad \textbf{(2-3)}$$

knowing that $B(x,y,z,t) = B_0 + G_x(t)x + G_y(t)y + G_z(t)z$ and that k-space is defined as the time integral of the gradients, i.e.

$$\boldsymbol{k(t) = \frac{\gamma}{2\pi}\int_0^t G(\tau)d\tau} \qquad \textbf{(2-4)}$$

the signal equation given in $\boldsymbol{s(t) = \iiint_{x,y,z} m(x,y,z) \cdot e^{-i\phi(x,y,z,t)}\, dx\, dy\, dz}$

(2-2) becomes

$$s(t) = \iiint_{x,y,z} m(x,y,z) \cdot e^{-i[k_x(t)x+k_y(t)y+k_z(t)z]}\, dx\, dy\, dz \qquad \textbf{(2-5)}$$

t=x,y,z m(x,y,z)·e−i[kxtx+kyty+kztz]dxdydz (2-5) and the signal equation in MRSI is the consideration of a frequency axis in order to account for the chemical shift phenomenon. Therefore, defining $k_f(t)=t$, the signal equation in MRSI becomes

$$s(t) = \int_x \int_y \int_z \int_f m(x,y,z,f) \cdot e^{-i[k_x(t)x+k_y(t)y+k_z(t)z+k_f(t)f]}\, dx\, dy\, dz\, df \qquad \textbf{(2-6)}$$

t=x y z f m(x,y,z,f)·e−i[kxtx+kyty+kztz+kftf]dxdydzdf (2-6) is a four-dimensional (4D) Fourier Transform (FT) of the excited object and its spectral contents. From this, it is clear that the inclusion of the temporal variable adds another dimension to the imaging problem compared to structural imaging. This formulation clearly depicts volumetric CSI acquisition and reconstruction as a four-dimensional sampling problem.

2.2 Encoding in CSI

2.2.1 Phase-encoded CSI

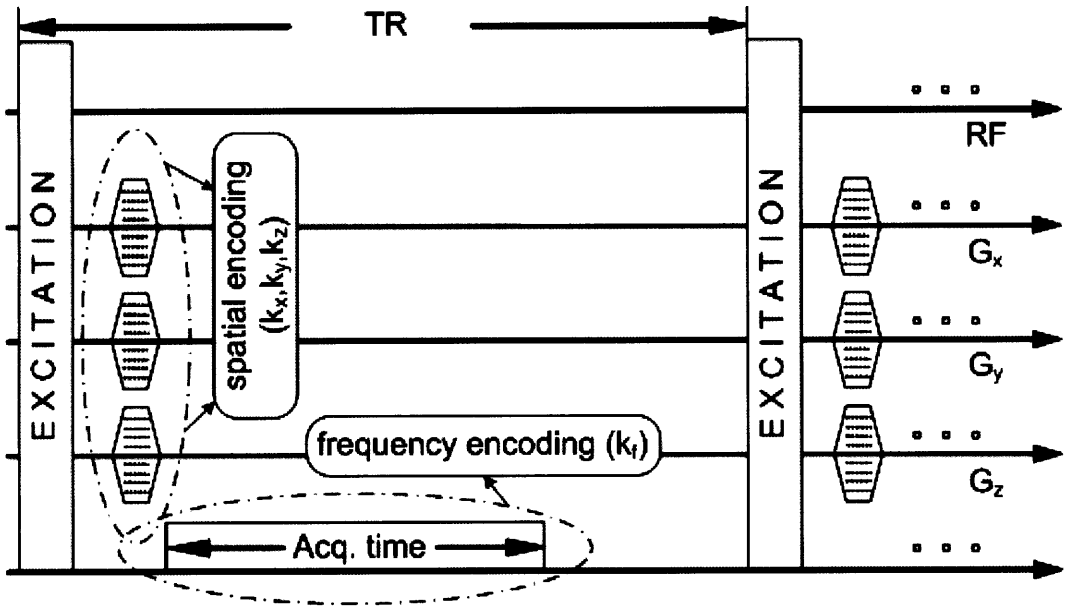

Figure 2-2: Encoding scheme for conventional, phase-encoded CSI acquisition. The spectral contents of each spatial frequency - phase-encoded one repetition period (TR) at a time - are acquired in a rather long readout period (several hundred milliseconds). The imaging time is dependent on the number of points that need to be collected in (kx,ky,kz) such that at least one TR is required for each resolved voxel, and can

therefore be impractically long for in vivo acquisitions of even modest (x,y,z) = (16,16,16) matrix sizes, which results in 2.3 hours at TR=2s.

Conventional, phase-encoded, CSI encodes the excited signal in the 4D spectral-spatial space in a straightforward, naïve way [30, 43]. It acquires FID (time encoding) for one spatial frequency at a time, i.e. per repetition period (TR). It uses the linear gradients (G_x, G_y and G_z) to traverse to a particular location in the (k_x,k_y,k_z) space prior to switching on the analog-to-digital converter (ADC), that then acquires samples along the k_f axis (Figure 2-2). While the limit for achieving certain spectral bandwidth is unconstrained (the ADC sample rates are in orders of μs), the spatial resolution requirements impact the time spent for the acquisitions. In other words, FOV, spatial resolution and imaging time *are not independent* parameters in conventional CSI, since going to higher resolutions inherently means collection of more (k_x,k_y,k_z) points, and hence more TR periods. This inflexible coupling between scan time and resolution parameters is impractical for even modest 16^3 spatial k-space positions, since this example of volumetric acquisition with TR = 2s will take about 2.3 hours – clearly a prohibitive time for *in vivo* experiments.

2.2.2 Time-varying readout gradients in CSI

As mentioned previously, spectral bandwidth (BW) is said to come "for free" in PE CSI, since the sampling rates that the currently used ADCs can reach, is in the orders of μs - far beyond the spectral BW requirements needed for CSI. As a matter of fact, all the resonances that are present in the *in vivo* ^{1}H spectrum are bandlimited to at most 10ppm, which means that the Nyquist rate along the frequency axis is at least Δk_f = 1/10ppm. At 3T, 10ppm ≅ 10·123.1Hz < 1250Hz, which means that spectral sampling of Δk_f = 1/1250Hz = 0.8ms is more than enough to capture all the spectral contents of potential interest. Furthermore, the hardware of the linear gradients (G_x, G_y and G_z) has undergone major improvements in the last two decades, allowing possibilities for fast k-space traversing. Nevertheless, the PE CSI takes absolutely no advantage of the gradients' potential, suggesting that a method involving efficient k-space sampling with time-varying readout gradients could overcome the rigid constraints on minimum acquisition time in PE CSI. Practically speaking, for 3T CSI, at least some part (if not all) of (k_x,k_y,k_z) space can be acquired during Δk_f.

This basic idea was first identified by Mansfield [53], and exploited in different forms by many for over 20 years [54-67]. In general, the approaches differ in the ways the spatial k-space is sampled (and later reconstructed), given the spectral BW limits. Some algorithms like the echo-planar spectroscopic imaging (EPSI) [66, 68] use conventional phase-encoding to acquire samples in (k_x,k_y), and play time-varying, echo-planar gradients during the long readout period to simultaneously encode the (k_z,k_f) space. In this case, 3D volumetric CSI data is obtained in acquisition times of a single slice PE CSI.

Even further reduction in acquisition times can be achieved if time-varying gradients are simultaneously played along two spatial directions. Adalsteinsson et al [67] have proposed time-efficient CSI algorithm based on spiral k-space trajectories. The idea of traversing the (k_x,k_y) space in a spiral manner makes excellent use of available gradient amplitude and slew rate (Figure 2-3a). In this encoding scheme, spiral trajectories are repeatedly playing during long readout period, simultaneously acquiring samples in (k_x,k_y,k_z) per TR (Figure 2-3b). For 3D volumetric acquisitions, phase-encoding is performed along the k_z axis (Figure 2-3c).

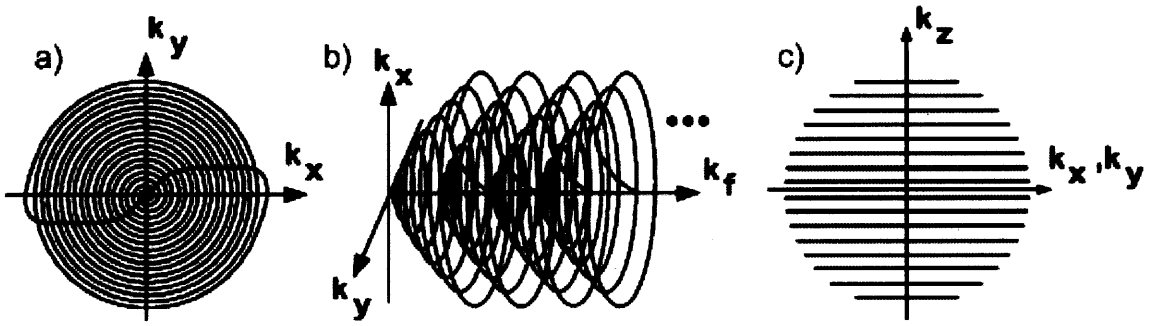

Figure 2-3: Encoding scheme of the spiral CSI algorithm; a) Sampling in the (kx,ky) plane is done with spiral-shaped trajectories; b) Spiral trajectories are repeatedly played in a long readout period for simultaneous encoding in of (kx,ky,kf) space within one TR; c) For volumetric acquisitions, phase-encoding is done along the kz axis.

2.3 Excitation in CSI

The readout explained above is preceded by excitation section, which excites the spatial volume of interest, mitigates all metabolites of interest (spectral mitigation), and suppresses the undesired water and lipid signals. There are different excitation modules, i.e. series of RF pulses that achieve the excitation demands of a CSI experiments. These can be broadly classified into three categories: 1. Preparation module, which

mainly deals with suppression of the water and/or lipid signals; 2. Localization module, which usually follows the preparation modules, and limits the excitation volume to a defined 3D space; and 3. Multi-dimensional, spectral-spatial RF pulses, which provide simultaneous excitation along two or three dimensions of the (x,y,z,f) space.

Before giving an overview of the mentioned modules, it is instructive to briefly touch upon how selective RF pulses work. An intuitive way to understand this is given by what is known as the "small tip angle approximation" [69]. If RF pulse is played out with accompanying gradient, the spatial region excited corresponds to the Fourier transform of the function obtained from values of the RF pulse, at excitation k-space locations defined by the gradient,

$$\boldsymbol{m_{xy}(\bar{r}) = i\gamma m_0 \int_0^T b_1(t) e^{i\bar{r}\bar{k}(t)} dt} \qquad \textbf{(2-7)}$$

where $m_{xy}(\bar{r})$ is the spatial region excited, $b_1(t)$ is the RF pulse envelope, and $\bar{k} = -\gamma \int_t^T \bar{G}(s)\, ds$ defines the k-space space waveform accompanying $b_1(t)$. In other words, the RF pulse will deposit energy onto excitation k-space at positions determined by the gradient, and the Fourier Transform of this function will produce the excited area/volume of interest [69]. For example, if the z gradient (G_z) and the RF pulse take the shape of a trapezoid and a sinc-like function, respectively, the resulted excited region will be a rectangular-shaped function along the z spatial dimension. Note that the pre-winding lobe is half the area of the main trapezoidal lobe (i.e. when the RF is played), and the reason for that is the center of the RF to be played at excitation $k_z = 0$.

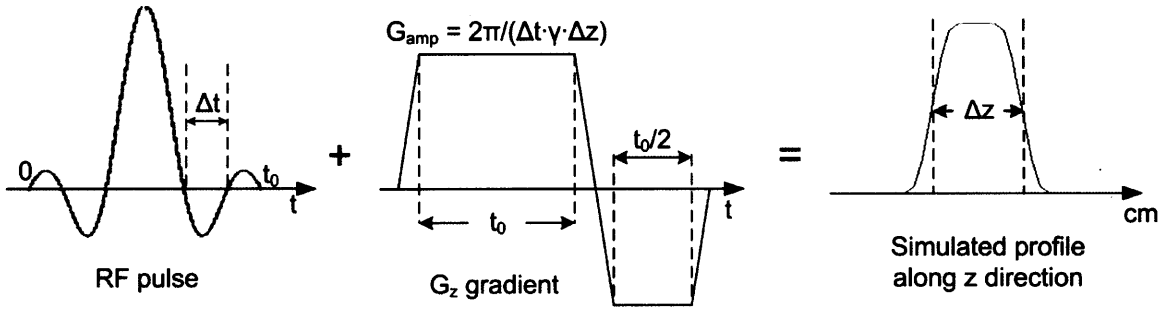

Figure 2-4: Spatially selective RF pulses. Trapezoid gradient is played on the z gradient channel and a truncated sinc function is played on the RF channel. The gradient amplitude and duration are given as a function of γ and the RF pulse parameters. The simulated excited profile has a rectangular-like shape along z axis.

Figure 2-4 shows a simulated profile as a result of a RF pulse and slice selective gradient. Increasing the time-bandwidth product (TBWP) of the pulse will improve the

sharpness of the excited profile. The amplitude and the duration of the slice selective gradient are given as function parameters of the RF pulse and the gyromagnetic ratio γ, as shown. Spectral selectivity is achieved when there is not any gradient played during the RF, and the spectral bandwidth of the frequency profile is a function of the TBWP and the duration of the RF pulse.

2.3.1 Preparation Modules for Water and Lipid Suppression

The preparation module precedes the localization part of the CSI excitation scheme, and its main purpose is to suppress as much of the dominant water signal as possible, mainly using spectrally-selective-only RF pulse. Some preparation modules also try to suppress the lipid signals as well, but given the proximity of the NAA resonance to the lipid peaks, these are only feasible for higher field CSI applications. The initial attempt of water suppression was introduced by [31] and was called CHEmical Shift Selective imaging (CHESS). It simply played a single Gaussian-shaped spectrally selective 90^0 pulse (centered on the water resonance) immediately followed by dephasing, spoiler gradient (G_s). The excitation module was played immediately following G_s.

At the end of the Gaussian pulse, all the water spins will be taken to the transverse plane leaving residual amounts of the M_z component. At the end of G_s, two things will happen: 1. most of the M_{xy} magnetization will be dephased; and 2. some amount of the M_z component will re-grow according to tissue's T_1 relaxation constant(s). However, since the duration of G_s is short compared to most of the tissues' T_1 constants, the amount by which the M_z component has re-grown is almost negligible. Therefore, the excitation pulse (played right after G_s) excites only the small residual M_z component, and hence noticeable water suppression factors are achieved.

The limitations of this technique is that, due to RF field (B_1^+) inhomogeneities particularly pronounced at higher B_0, the water suppression (i.e. the residual M_z) is not uniform as a function of space. Water Suppression enhanced through T1 effects (WET) [32], and others [70-71], have tried to address this issue. WET plays a series of spectrally-selective RF pulses spaced τ milliseconds apart, which incrementally decreases (from one pulse to the next) the M_z component of the water signal across the entire region of interest. Given B_1^+ map, τ, and several T_1 values of tissues in the head (e.g. cerebrospinal fluid, white and gray matter, etc), it finds the optimal set of flip angles

of the spectrally selective pulses, in order to achieve uniform water suppression across the brain.

An example of a typical *in vivo* B_1^+ map acquired at 3T is given in Figure 2-5a, showing the slight central brightening present at this field strength. Assuming, for simplicity, that all the tissues in the head have the same T_1, the optimal set of flip angles from a three-pulse suppression module that would minimize the water's M_z component is $(\alpha1, \alpha2, \alpha3) = (72^0, 90^0, 138^0)$. Figure 2-5b shows the timing diagram of three spectrally selective pulses separated τ milliseconds apart. For this example, τ = 30ms and T_1 = 500ms. Lastly, Figure 2-5c shows the simulated residual M_z component of the water right before the beginning of the α_2 (left image), α_3 (middle image) and excitation pulse (right image). As expected, the continuous decrease of M_z after each of the three pulses is clearly noticeable. The maximum and mean percentage of residual M_z relative to the steady state longitudinal magnetization before the excitation pulse was calculated to be 2.1% and 0.76%, respectively.

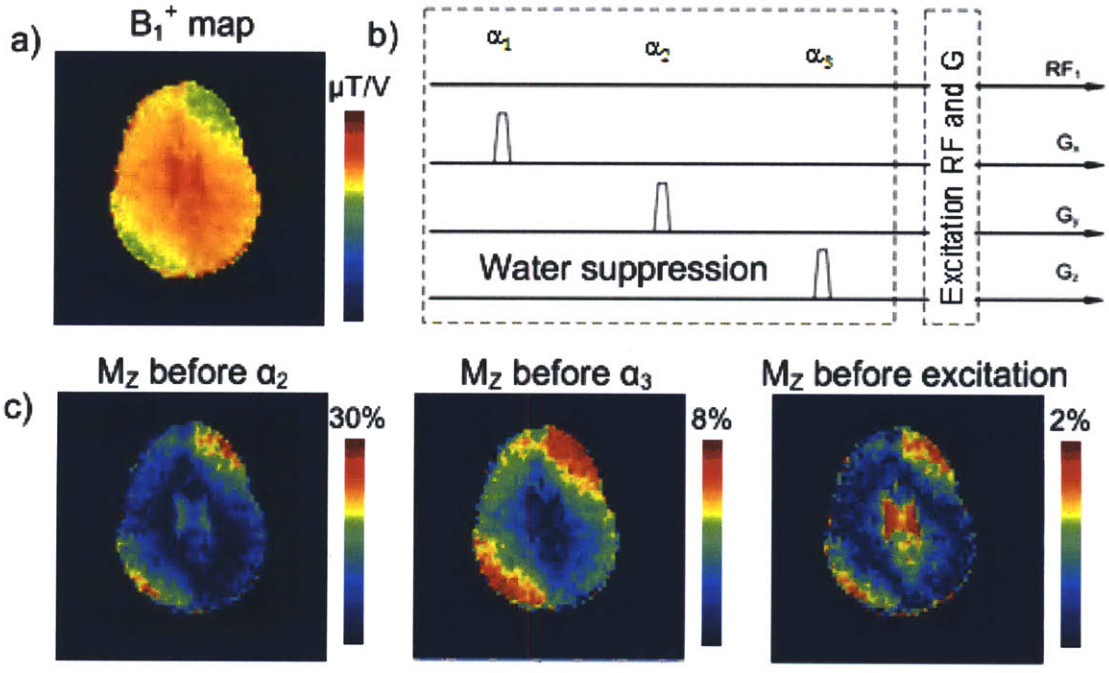

Figure 2-5: WET. a) Estimated *in vivo* B_1^+ map at 3T; b) Timing diagram of a three-pulse water suppression module, where the spectrally-selective-only pulses are separated τ ms apart; c) Residual M_z component maps before the beginning of the α_2 (left image), the α_3 (middle image), and the excitation pulse (right image, showing a step-wise decrease of the residual M_Z after the application of each water-suppression pulse, with spatial variation in performance based on inhomogenous B_1^+

As mentioned previously, the preparation module can also be used to suppress the lipid signals. Balchandani et al [72] used spectrally selective adiabatic pulses [73-76] to

invert the lipid signals prior to the CHESS module in a way that most of the lipid signals are nulled at the time of excitation. This was demonstrated on 7T platform, where the frequency dispersion is increased enough so that the adiabatic pulses reliably excite the lipid signals (at 1.3ppm and 0.9ppm), but not the neighboring NAA peak (at 2.0ppm). In general, it is very difficult to use spectrally selective pulses for lipid suppression for field strengths lower than 3T with spectral cutoffs that do not account for spatial variations in main field homogeneity.

In the case when spectral selectivity between the lipid and NAA is a challenge, a way to suppress the lipid signals is to play non-selective inversion adiabatic pulse [77-78], which inverts all the spins across space and frequency. Then, knowing the T_1 relaxation constant(s) of the lipid signals, the excitation pulse is played at inversion time (TI) when the longitudinal component of the lipid signal is close to zero. The drawback of this method is that some of the metabolites' signals will be lost, as they have been affected by the inversion pulse as well. Since the T_1 constants of the metabolites are longer than those of the lipid signals, the SNR loss of the metabolites signals ranges between 15-20%.

2.3.2 Spatial localization

The main purpose of the spatial localization module is to excite the desired 3D spatial volume of interest over which the metabolite quantification is to be evaluated. Almost all of the excitation schemes curve out a box within the FOV by playing a series of RF pulses, each of which excites a slice in different spatial orientation (i.e. x, y, z). Specifically, the Point RESolved Spectroscopy (PRESS) excitation pattern [79] plays the [90^0-180^0-180^0] train of pulses which slice-selects about the x, y and z axis, respectively. STimulated Echo Acquisition Mode (STEAM) excitation [80-81] on the hand, play the [90^0-90^0-90^0] train of pulses, again selecting slices in x, y and z, respectively. While STEAM is capable of exciting small VOIs effectively (particularly important for single voxel experimens), the PRESS excitation provides somewhat sharper slice selection, and is more useful in CSI acquisitions with long echo times (due to the refocusing of the effects of 180^0's).

Slice selective adiabatic refocusing pulses have also been extensively used as a spatial localization module, due to their ability to provide extremely sharp slice-selection. GOIA (Gradient Offset Independent Adiabaticity) [82-83] or FOCI (Frequency Offset

Corrected Inversion) [84-86] pulses have been used in LASER (Localized Adiabatic Selective Refocusing) [87-88] excitation schemes. The train of the adiabatic RF pulses in a LASER sequence, usually starts off with a no selective adiabatic 90^0 pulse, which is then followed by a series of adiabatic 180^0's that slice-select along the three spatial axis. The excellent slice selectivity of these RFs comes at a cost of high voltage demands for the 180^0 pulses, and therefore higher Specific Absorption Rate (SAR) values. As a matter of fact, for some slice thicknesses and shorter TR (~1s), the FOCI 180^0 pulse violate the SAR limits.

In clinical settings, it is a common practice to prescribe the excitation box of the localization module wholly within the brain in order to avoid any excitation of the lipid signals coming from the skull. In other words, although the excited box might not even touch (include) the skull, imperfections in the slice-profiles (particularly for PRESS and STEAM, and much less for LASER) can cause even slight mitigation of the lipids which would cause considerable contamination of the metabolite signals. Therefore, outer-volume-suppression (OVS) bands [89] are usually prescribed on top of the skull tissue (outside the excitation box). In essence, these 90^0 pulses excite the selected skull regions, after which gradient crushers de-phase all of the transverse magnetization. Since the OVS bands and the crusher gradients immediately precede the excitation (PRESS, STEAM, LASER, etc), no magnetization of the saturated region is left at the time of excitation. Therefore, the saturated part of the VOI is not going to be excited.

2.3.3 Multi-dimensional, Spectral-Spatial RF designs

All of the excitation modules mentioned so far are composed out of RF pulses which are selective in one spatial dimensional only, and are therefore referred to as 1-D pulses. More involved designs include selectivity along one additional axis (spectral or spatial), which for CSI related applications is most likely to be the frequency axis. The goal of these two-dimensional, spectral-spatial excitation schemes is to provide excitation profiles that are spatially selective over particular slab thickness (usually along the z axis), while in the same time achieving spectral selectivity that would suppress the water and/or lipid signals, but mitigate the metabolites of interest. In signal processing terminology, this pulses fall under the category of 2D low pass filter designs.

The concepts of simultaneous spectral-spatial RF excitation have been explored extensively in the past [90-93]. The basic idea behind designing a spectral-spatial pulse

is given in Figure 2-6, and can be summarized in three steps: 1. Create the spectrally selective RF pulse, given the spectral bandwidth requirements (i.e. determining the extent of the pass band, transition band and the stop band); 2. Given the spatial requirements (slices thickness and sharpness), design the *spatial selective RF pulse that has the same length as the sampling period of the spectral pulse*; 3. Create a train of N spatially-selective pulses, which is then modulated by the N-samples-long shape of the spectrally selective pulse.

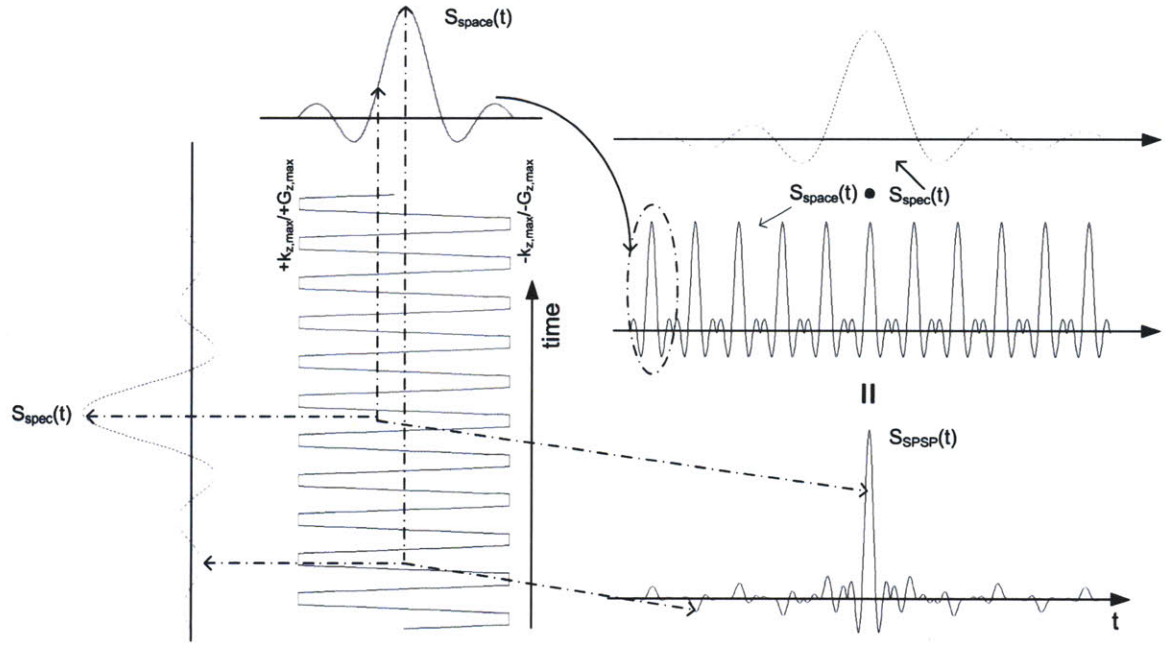

Figure 2-6: Generating a spectral-spatial RF pulse. Its shape is determined by multiple repetitions (in time) of the spatially-selective RF pulse, modulated by the shape of the spectrally-selection function.

Figure 2-7a shows an example of a 25ms-long spectral-spatial RF pulse (N = 50 samples) and the accompanying G_z gradients for 7T CSI. The pulse was designed to excite 3-cm thick slab in z and 400Hz of spectral bandwidth, but to also suppress most of the signals at -620Hz and +400Hz (these parameters were determined for metabolite mitigation and water/lipid suppression at 7T, respectively). The 2D Bloch simulation in Figure 2-7b shows the magnitude of the desired (z-f) excitation profile. Figure 2-7c and Figure 2-7d show the cross-section across the spatial axis (f = 0), and across the frequency axis (for z = 0), respectively.

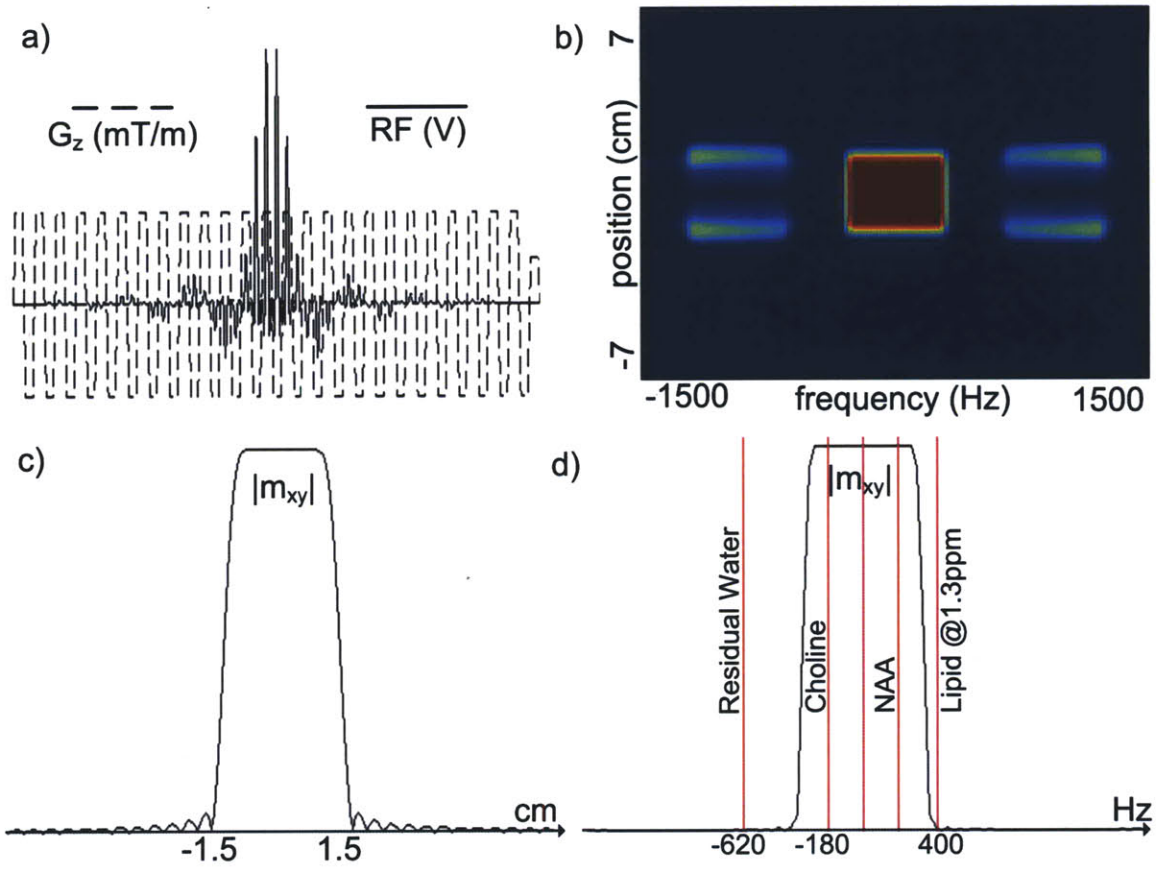

Figure 2-7: a) The shapes of the G_z gradient (dashed line) and the real part of the RF pulse (solid lines) used for spectral-spatial excitation; b) Bloch simulation showing the resulting (z-f) profile; c) Cross-section across the spatial axis (f = 0), showing the 1D slice selection profile; d) Cross-section across the frequency axis (z = 0), showing the 1D spectral profile;

Chapter 3

Spiral Spectroscopic Imaging on Clinical 3T Siemens Systems

As briefly mentioned in Section 2.2.2, an efficient way to address the inherently long acquisition times of the conventional, phase-encoded (PE) chemical shift imaging (CSI), is by using time varying gradients during the long acquisition readout periods, so that in addition to sampling the time (k_f) axis, samples are simultaneously acquired along one or two spatial axis. The spiral CSI algorithm, introduced by Adalsteinsson et al [65, 67-68], uses 2D spiral-shaped k-space trajectories that are repeatedly played during the long acquisition window, to simultaneously collect samples in the 3D (k_x,k_y,k_f) space in each repetition period (TR). The spiral-shaped trajectories are formed by playing sinusoidal gradient waveforms simultaneously along G_x and G_y axes. Figure 2-3 in Section 2.2.2 depicts the sampling scheme of the spiral CSI encoding.

The work presented in this chapter involved full implementation of the spiral CSI algorithm on Siemens® MRI scanners. Given any set of CSI parameters, the developed spiral CSI software package designed the appropriate spiral trajectories in real time, provided on-line reconstruction of the spirally-acquired k-space samples, and returned the Cartesian-grid-resampled spectroscopic data on the standard Spectroscopy Tool® Task Card installed on every Siemens scanner. The main premise in mind was to allow

the clinically-oriented population to take advantage of algorithm's time-efficiency, so that 3D volumetric spectroscopic acquisitions become reality in clinical settings.

This chapter will start by providing a brief introduction discussing the sampling patterns involved in the spiral CSI, mainly focusing on the concept of interleaving. It will then elaborate on the most important steps involved in the development of the spiral CSI algorithm on Siemens MR platforms. In order to show the reliability of the developed spiral CSI engine, we will then present side-by-side comparisons of phantom and *in vivo* spectroscopic data acquired using the PE and spiral CSI readouts for fixed imaging parameters. Lastly, we will show preliminary data from two clinical applications using the spiral CSI engine. The first one is collaboration with Dr. Eichler (Department of Neurology, MGH, Boston, MA) where we explore the metabolite contents in different part of the brain of patients diagnosed with the neurodegenerative disease called Late-Onset Tay Sachs (LOTS). The second is a collaboration with Dr. Andronesi and Dr. Sorensen (Department of Neurology, A. A. Martinos Center for Biomedical Imaging, MGH, Boston, MA), where the 3D spiral CSI readouts were applied in a study on brain tumor patients.

3.1 Introduction: Temporal and Angular Interleaving

The primary constraint of the sampling requirements in spiral CSI, is that different time samples of the same (k_x,k_y,k_z) point need to be separated by time period not longer than $\Delta k_f = 1/FOV_f$, where FOV_f is the readout spectral bandwidth (Hz). The number of k_f points acquired during the long acquisition window (e.g. 320ms) determines the spectral resolution. For small enough objects, i.e. for small spatial FOV and/or smaller resolution parameters, it might be possible to design spiral trajectories that are shorter then Δk_f. In this case, one would be able to acquire single slice spectroscopic data *in only one TR*.

Nevertheless, given more realistic spatial resolution and FOV parameters (e.g. 0.5cc over 24cm), and given the physical limitations of the maximum allowable gradient amplitude and slew limits, in most of the cases it is impossible to traverse certain k-space volume in Δk_f seconds. To overcome this constraint, the spiral CSI algorithm plays different subparts (interleaves) of the of desired (k_x,k_y,k_f) space in every subsequent TR period. Hence the number of acquired TRs will increase with more demanding (i.e. higher) spectral-spatial imaging requirements. There are two types of interleaving – angular and temporal, each of which will be discussed next.

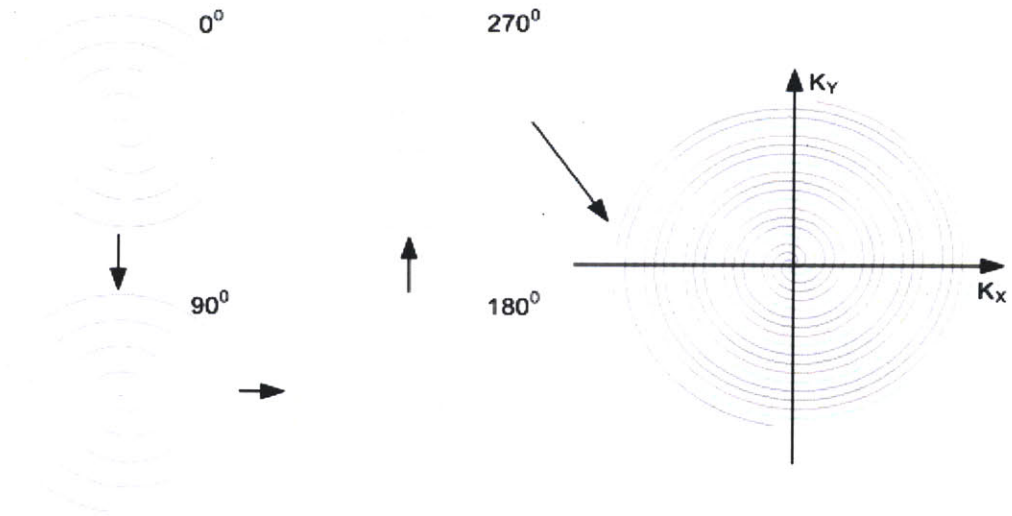

Figure 3-1: Decomposing spiral k-space trajectory into $N_A = 4$ angular interleaves. After being undersampled by a factor of 4, the spiral lobes are sequentially rotated by $2\pi/N_A$ radians.

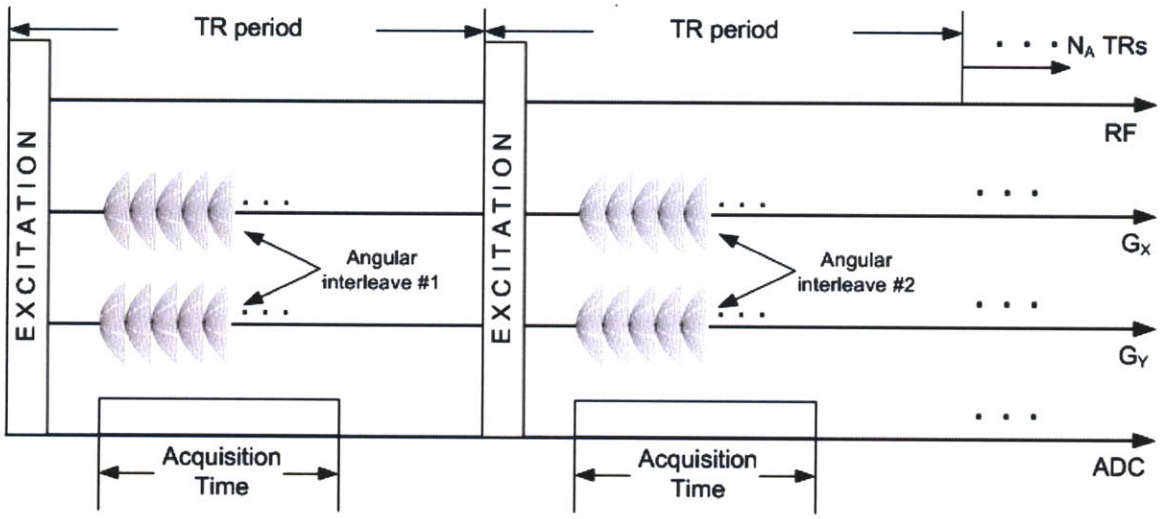

Figure 3-2: Timing diagram showing 2 out of the $N_A = 4$ angular interleaves shown in Figure 3-1. In one TR, samples of all time (k_f) points of a subset of (k_x,k_y) samples are acquired. The rest of the (k_x,k_y,k_f) space is collected in subsequent TRs. For this example, single slice spectroscopic imaging is acquired in 4 TRs.

With angular interleaves, commonly used in structural spiral MRI, the desired k-space spiral trajectory is divided, or decomposed into spiral trajectories (angular interleaves) that are sparser than the original one (Figure 3-1). Being sparser also means being shorter in duration. The duration of an angular interleave is now a design parameter, and has to be shorter or equal than Δk_f (if shorter than Δk_f, the trajectory is padded with zeros, until its duration is equal to Δk_f). If certain k-space spiral trajectory can be decomposed in N_A angular interleaves, then a single slice spectroscopic data is acquired in N_A TRs. An informative observation about angular interleaving is that *in one*

TR we sample all the time (k_f) points of only a subset of (k_x,k_y) samples (i.e. the ones included in the particular angular interleave). The timing diagram of the angular interleaving is given in Figure 3-2.

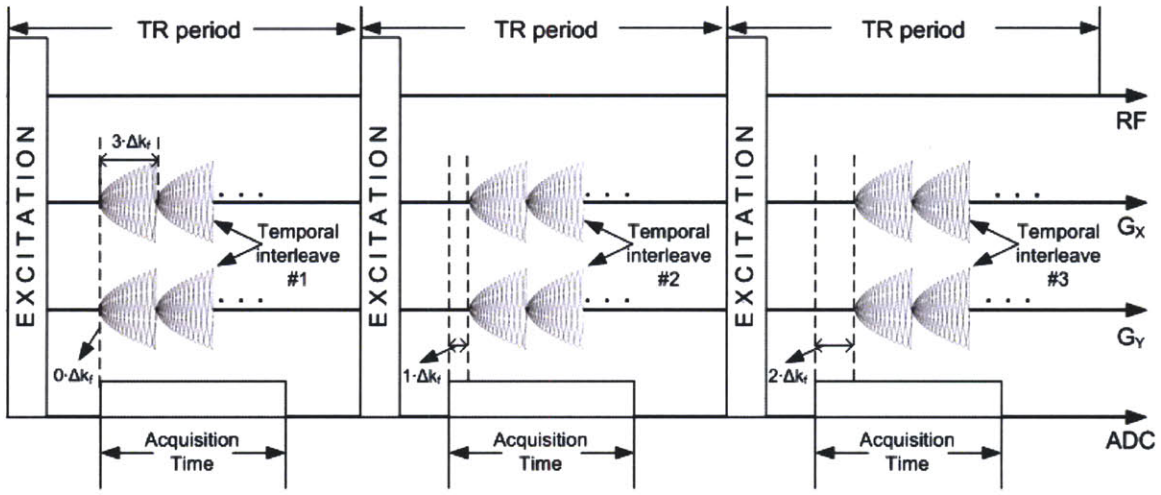

Figure 3-3: Timing diagram describing the concept of temporal interleaves for the case of N_T = 3. Each temporal interleave played in different TRs, delays the start of the readout gradients relative to the ADC window by $n \cdot \Delta k_f$ seconds (n = [0, 1, 2]) in every subsequent TR. The length of one spiral lobe has to be an integer multiple of Δk_f the temporal sampling time (uniform temporal sampling is obtained).

A different way of decomposing the designed (k_x,k_y,k_f) is temporal interleaving. Here, the original spiral trajectory is kept unchanged, and is repeatedly played during the long acquisition time. However, in this case, looking at the data acquired in one TR, samples in (k_x,k_y) are separated apart much more than Δk_f seconds, and therefore the spectral bandwidth requirements are violated. To fulfill the gaps along the k_f axis, the readout gradients are started $n \cdot \Delta k_f$ seconds later relative to the ADC window in every subsequent TR. Here n = [0, 1, …, N_T-1], where N_T is the number of temporal interleaves needed to satisfy the spectral BW design parameters. A design parameter in this case is that the *total length of the spiral trajectory is an integer multiple of Δk_f*, in order to be sure that the single slice spectroscopic data acquired in N_T TRs has *uniform sampling along the k_f axis*. The timing diagram of the temporal interleaves concept is given in Figure 3-3 for the case of N_T = 3. Here in TR #1, for every (k_x,k_y) sample, we get the 1st, 4th, 7th, etc., time samples. In TR #2 and TR #3, all of (k_x,k_y) points get the 2nd, 5th, 8th, etc., and 3rd, 6th, 9th, etc., time samples, respectively. Since the length of spiral lobes is $3 \cdot \Delta k_f = N_T \cdot \Delta k_f$, uniform sampling along k_f axis is guaranteed.

Up to this date, the spiral CSI algorithm is one of the most time-efficient spectroscopic imaging techniques. Even at high field strengths, where the acquisition

times are inherently longer due to the more demanding spectral bandwidth limits caused by the increased frequency dispersion, the spiral CSI provides order of magnitude speed-up factors compared to the widely used PE CSI readouts. Table 1 shows comparisons of the scan times (for TR = 2s) of the PE CSI and spiral CSI for single slice spectroscopic data set at spectral bandwidths of 600Hz, 1200Hz and 3000Hz, corresponding to ~10ppm at 1.5T, 3T and 7T, respectively. The comparison was done on acquisitions with FOV_{XY} = 24cm encoded over matrix size of (x,y) = (32,32), for an isotropic voxel size of 0.56cc. The maximum amplitude and slew rate of the gradients in the spiral designs was set to conservative 10mT/m and 120mT/m/ms. It is clear that spiral CSI trades off acquisition times with spectral bandwidth, but even for the 3000Hz spectral bandwidth designs, we still get ~26 fold decrease in scan time, which is an improvement that make *in vivo* studies feasible.

Spectral BW (FOV_f)	2D Spiral CSI	2D PE CSI	Speed up factor
600 Hz (1.5T)	16s	2048s = 34.1min	170.2
1200 Hz (3.0T)	30s	2048s = 34.1min	68.3
3000 Hz (7.0T)	80s	2048s = 34.1min	25.6

Table 1: Comparisons of the overall scan times for single slice spiral CSI and PECSI acquisitions for three different spectral bandwidths corresponding to three field strengths. The times are given assuming TR = 2s. Even at the upper limits of spectral bandwidths, the spiral CSI offers orders of magnitudes decrease in acquisitions times.

At last, it is instructive to note that SNR in MRI does not depend on the number of samples acquired, but only on the voxel size and the square root of the time spend on acquiring the signal [38-39], or more specifically, $SNR \cong V_{size} \cdot \sqrt{T_{acq}}$. Therefore, there is not any inherent SNR loss due to the usage of the spiral CSI encoding. The only SNR loss is due to the decease of the acquisition time which can be addressed by averages of the single slice scans, or, even better, extending the encoding to 3D, volumetric acquisitions. For example, 32 slices spiral CSI data (enough to encode the entire head) for FOV_f = 1200Hz, with take only 16 minutes (TR = 2), which, while long, is an acceptable scan time for many *in vivo* measurements.

3.2 Implementing Spiral CSI on Siemens Platforms

The process of implementing the spiral CSI algorithm on Siemens MR scanners involved C++ programming under the Integrated Development Environment for Applications (IDEA®), a set of C++ libraries and classes provided by Siemens, that enables researchers to program (almost) any desired acquisition and on-line reconstruction schemes. Therefore, the development of spiral CSI algorithm under IDEA can be in general divided into two major programming tasks:

- Implementation of a spiral CSI sequence, i.e. generation of a executable (installed on the scanner) which has been compiled from a C++ code that, given the user defined imaging parameters (on the scanner), designs the spiral k-space trajectories in real time.
- Implementation of the reconstruction algorithm that takes the spirally acquired data, re-grids [94] it on Cartesian-grids and outputs the resulting spectroscopic data in the format required by the Siemens Spectroscopy Toolbox® Task Card, used to evaluate metabolites' contents on the scanner.

Further details regarding these two programming projects are given next.

3.2.1 The spiral CSI sequence

The new sequence, abbreviated as 'csi_se_spiral', was based on Siemens' product CSI sequence, where the phase-encoded readouts were replaced with the time-efficient spiral trajectories. The interface of the sequence protocol, listing all the imaging parameters that could be changed by the operator, remained equivalent to the one in the original PE CSI product sequence. This included the values of the spatial FOVs, the spectral BW, the size of the (x,y,z,f) matrix, the ability to prescribe outer volume saturation (OVS) bands, to change the TR and TE, to acquire data using multi-channel coil arrays, etc. In addition, extra parameters specific to the spiral CSI (e.g. gradient delays) could be also modified from the protocol task card.

For a given spatial imaging parameters, 'csi_se_spiral' designed constant density spiral k-space trajectories, which were then played in N_A angular and N_T temporal interleaves, i.e. in ($N_A \cdot N_T$) TRs. The values of N_A and N_T were optimized based on the user-defined spectral parameters, such that the length of the rewinder gradients, played

at the end of each repeatedly acquired spiral lobes, is minimized. The acquired rewinder gradient's samples, which is required so that the spiraled-out k-space trajectory is brought back to $(k_x,k_y) = 0$, are not used in the reconstruction, and therefore longer rewinder lengths imply larger SNR loss (hence the need to minimize the rewinder's length). The trajectories calculated were based on a constant density spiral design, which as a function of k-space radius, keeps the distance between the spiral windings equidistant (see e.g. Figure 3-1).

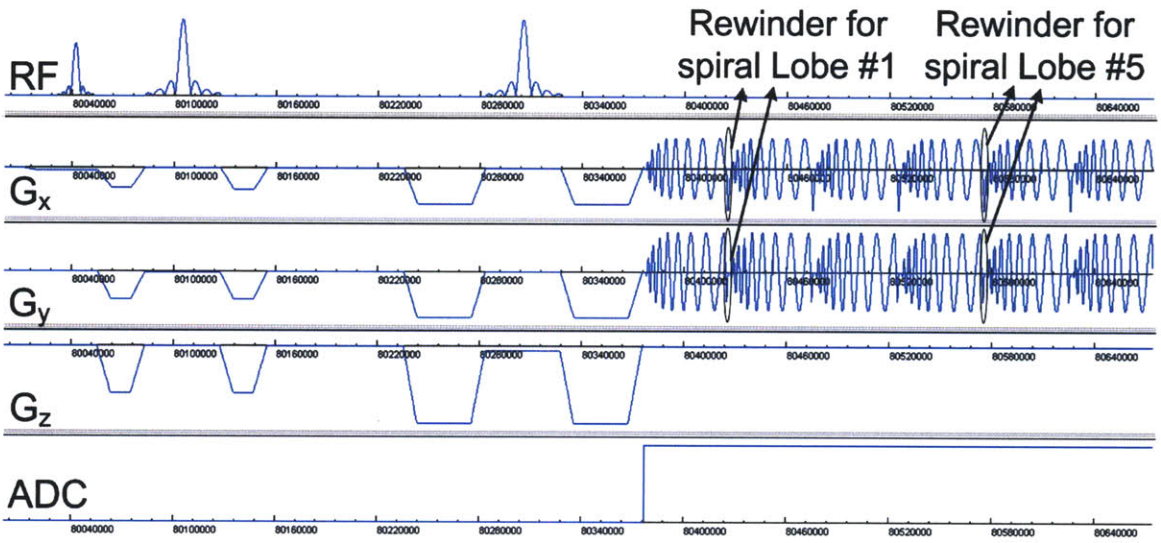

Figure 3-4: IDEA simulation of the spiral CSI sequence, showing the spiral readouts appended to a standard PRESS-box excitation. For the given spectral-spatial imaging parameters, the sequence generated spiral trajectories of length 5ms, 8% of which belongs to the rewinder gradients (identified on the figure for the 1st and 5th spiral lobe).

Figure 3-4 shows the timing diagram obtained from IDEA simulation of 'csi_se_spiral', demonstrating its ability to successfully append the designed spiral CSI readouts to the conventional PRESS-box excitation scheme (TE = 40ms). For this particular example, the spiral trajectories were calculated to encode the (x,y,f) = (32x32x 256) space, over FOV_{xy} = 24cm (voxel size = 0.56cc) and FOV_f = 800Hz. The total duration of each spiral lobe (including the rewinder) was 5ms, and with $N_T = 4$ and $N_A = 2$, the rewinder gradient accounted for only 8% of the spiral lobe length. Figure 3-4 clearly identifies the rewinder gradients of the 1st and 5th spiral lobe within the 320ms-long acquisition window (not completely shown). With TR=2s, the total duration of this single-slice spectroscopic acquisition was only 20 seconds.

3.2.2 The online gridding reconstruction

The spectral-spatial k-space data acquired from all receive channels using the sequence 'csi_se_spiral' was fed to the reconstruction computer running under the Image Calculation Environment® (ICE), where the executable 'IceProgramSpiralCSI' was used for reconstruction. The main task of the C++ code used to compile this executable was to develop the functions and classes needed to efficiently re-grid the spirally acquired k-space data onto Cartesian grids. Hence, the core of the developed code was the 2X gridding routine [94], performed using Kaiser-bessel kernel with window width W=6 and shape parameter β = 13.86. Note that the sequence ('csi_se_spiral') ordered the acquisition of the spectroscopic data such that the angular interleaves were in the inner loop of the running kernel. In other words, before acquiring the (k_x,k_y,k_f) samples of the, e.g. third temporal interleave, the samples of *all* angular interleaves for the second temporal interleave were acquired first. This ordering improved the reconstruction efficiency, as it enabled 'IceProgramSpiralCSI' to perform the 2X gridding on all the (k_x,k_y) samples for the given temporal interleave, while the (k_x,k_y) samples of the next temporal interleave were being acquired in parallel.

Technically, gridding should be employed along the k_f axis as well, as the majority of the k_f samples are not acquired at times which are integer multiples of $\Delta k_f = 1/FOV_f$. Specifically, 'csi_se_spiral' acquires samples every 10μs (this is the used sampling rate of the analog-to-digital receiver), while Δk_f is usually in orders of ms (e.g. for FOV_f = 1000Hz, Δk_f = 1ms). However, instead of k_f gridding (which can be time consuming), appropriate phase correction was applied to all the k_f samples that don't fall on the spectral Cartesian grid. This correction exploits the Discrete Fourier Transform shifting property, which states that non-integer delays in time domain can be corrected for by applying a phase term in the frequency domain of the form $\exp(-i2\pi t_0 f)$, for all t_0, even if $t_0 < \Delta k_f$. Note that this phasing was done prior to (k_x,k_y) gridding.

Given the nature of the spiral encoding, potential delays between the gradients and the ADC event block can results in *spatial* rotation and blurring. Using already developed gradient characterization methods [95], we found out that on several scanners this delay was ~8μs on both X and X gradients. 'IceProgramSpiralCSI' used this delay to properly correct the k-space trajectories and to assure correct reconstructions.

Once re-gridded, the Cartesian (x,y,z,f) samples from each of the receive coil array's elements, were optimally combined using an estimation of the coil sensitivities'

complex weights. These weights were obtained from a short pre-scan, which is a standard sequence on all Siemens scanner. The coil combination for the sample at (x_c,y_c,z_c,f_c) from an acquisition using N_C receive coil elements is given by

$$S_{x,y,z,f} = (C^H D)/\sqrt{C^H C} \quad \textbf{(3-1)}$$

where C^H ([1xN_C]) is the Hermitian vector of the complex weights from all the coils at (x_c, y_c,z_c,f_c), and D ([N_Cx1]) is the vector holding the samples from all the coils at (x_c,y_c,z_c,f_c).

The reconstruction times for even the "data-heavy" acquisitions were reasonable. For example, the reconstruction of 3D volumetric spiral CSI acquisition with isotropic voxel size of 0.25cc and using 32-channel receive coil array, was finished ~45 seconds after the end of the acquisition. Note that this time would have been much longer had the reconstruction not started in parallel with the acquisition. The reconstruction of the data acquired at lower resolutions or using less receive elements, finished instantaneously after the end of the acquisition. Finally, the single data set, holding the coil combined, Cartesian gridded (x,y,z,f) samples was sent to the Spectroscopy Toolbox Task Card for spectral analysis of the metabolites detected.

3.3 Verifying the spiral CSI reconstruction

In this section we compare phantom and *in vivo* 3T spectroscopic data acquired and reconstructed using: 1. the developed Siemens spiral CSI software package; and 2. The Siemens product PE CSI sequence. Same imaging parameters were prescribed on both sequences, which included acquisition of 3D CSI data using (x,y,z,f) = (16x16x8x512) samples, encoded over FOV_{XY} = 16cm^2, FOV_Z = 8cm and spectral bandwidth of FOV_f = 1200Hz. Hence, the overall isotropic voxel size was 1cc. Using the option for elliptical k-space sampling, the total duration of the PE CSI sequence was 10min (TR = 1s). In order to provide a more fair comparison in terms of SNR, the spiral CSI sequence used 12 averages for a total scan time 9.6min (TR = 1s). For the *in vivo* acquisitions, TR of 2s was used.

To emphasize the benefit of the fast encoding, the spiral CSI sequence was used to acquire an additional, higher resolution spectroscopic data set. With FOV_{XY} = 16cm^2, FOV_Z = 8.8cm, FOVf = 1200Hz, and the 4D encoding matrix set to (x,y,z,f) = (22x22x12x512), the voxel size of this acquisition was an isotropic 0.38cc. The overall

scan took 4.8min (2 averages, TR = 1s). Due to SNR constraint, this acquisition was only employed in phantom, and not *in vivo*. For all the acquisitions, both the PE, and the spiral CSI readouts were appended to a LASER excitation scheme [88], which provides significantly improved localization profile compared to the traditional PRESS-box excitation (TE = 45ms). All experiments were performed using the standard Siemens' 32-channel receive coil array.

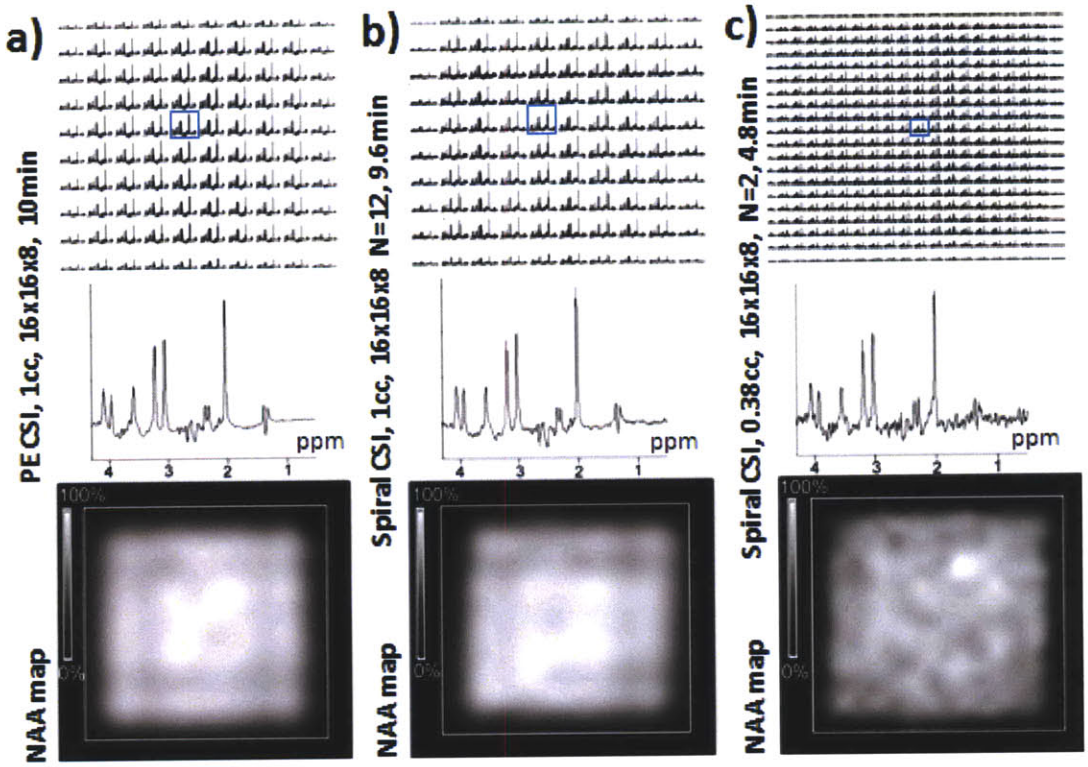

Figure 3-5: Phantom 1cc, 3D CSI, 10min acquisitions using a) PE CSI readout; b) Spiral CSI readouts (12 averages), showing equivalent results; c) 0.38cc, 4.8min 3D spiral CSI acquisition, demonstrating a flexible setting for scan time and voxel size that is possible with time-varying readout gradients. Reduction in voxel size and imaging time results in natural SNR tradeoffs as evident when panel c) is compared to those shown in a) and b).

Figure 3-5 shows side-by-side phantom comparisons of the spiral and PE CSI acquisitions from the middle slice of the 3D data sets (5^{th} slice for the 1cc, and 7^{th} slice for the 0.38cc scans). The 17-cm diameter spectroscopy phantom used for the experiments, contained physiological concentrations of the following brain metabolites [96]: 12.5 mM N-acetyl-L-aspartate (NAA), 10.0 mM creatine (Cr), 3.0 mM choline (Cho), 12.5 mM Glutamate (Glu) and 7.5 mM myo-inositol (mI). The volume of interest (VOI)-box that was excited by the LASER pulses was of size (x,y,z) = (10x10x4)cm^3. All spectral grids and NAA maps shown were generated by the Spectroscopy Toolbox Task

Card. Visually comparing the data presented in Figure 3-5a and Figure 3-5b, we see that the two employed encoding schemes yield equivalent results, as expected. Closely looking at the sample spectrum shown in the middle, we do see that the Spiral CSI acquisition in Figure 3-5b is slightly lower in SNR. However, this is not surprising, having in mind that the acquired data belonging to the rewinder gradients was not used in the reconstruction, alluding to the fact that the spiral CSI acquisition effectively spent less time acquiring data. However, SNR is not an issue, not just in this case, but also in the shorter, higher resolution (0.38cc) scan shown in Figure 3-5c. Here, the spectral quality (middle image) is quite reasonable, and the NAA map shown in Figure 3-5c is considered reliable, far from the level of being compromised.

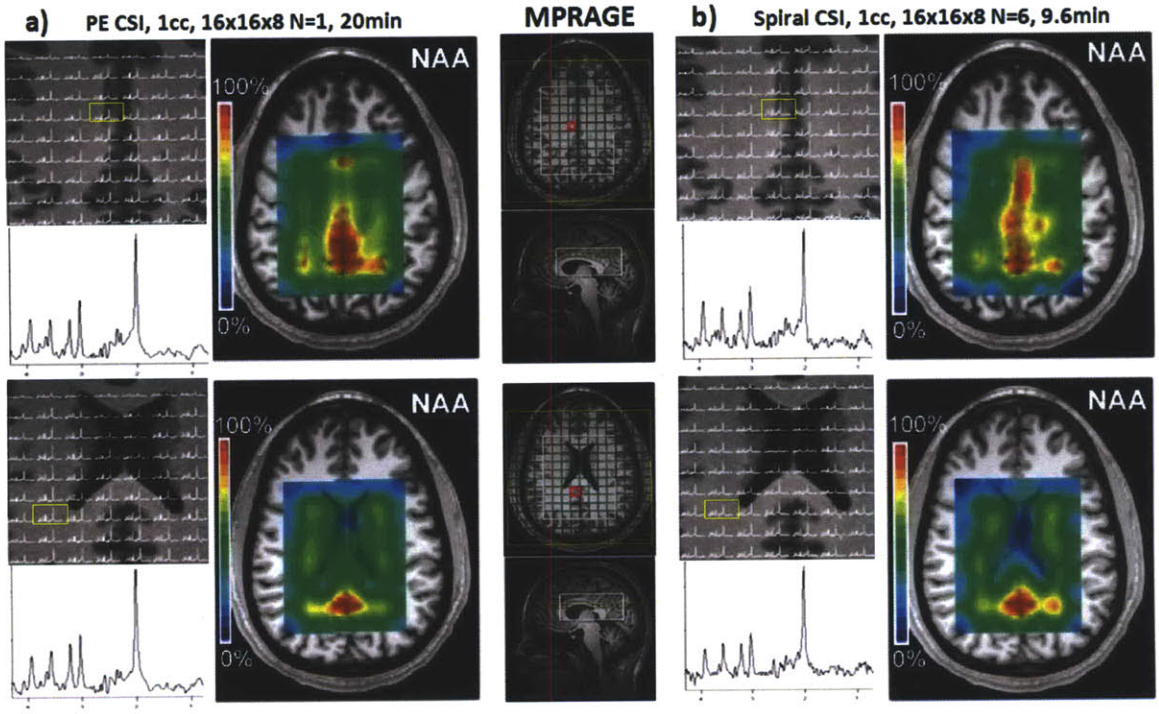

Figure 3-6: In vivo 1cc, 3D CSI scans using a) PE CSI readout acquired in 20min (TR = 2s); b) Spiral CSI readouts acquired with 9.6min (6 averages, TR 2s), demonstrating the expected tradeoffs, i.e. shorter imaging time results in reduced SNR for a fixed voxel size.

Figure 3-6 shows the *in vivo* comparisons between PE and spiral CSI readout. The 3D, 1cc protocols, described before, were employed on a healthy volunteer, who has signed the consent forms approved by the Institutional Review Board (IRB) of our institution. The volume of interest (VOI)-box excited by the LASER pulses was of size (x,y,z) = (10x8x4)cm^3, and was prescribed wholly inside the brain, in order to avoid lipid contamination from the skull. No OVS bands were used, and TR = 2s. Again, visual

inspection of the data from two different slices, above the ventricles (top row), and in the ventricles (bottom row), alludes to their equivalence. Reduction of the number of averages for the spiral CSI acquisition to 6, yielded patient-friendlier scan time (10min). In the same time, it did not compromise the spectral quality in terms of SNR.

3.4 Spiral CSI in Clinical Settings

The spiral CSI package is currently installed on number of 3T Siemens scanners at the Massachusetts General Hospital (Boston, MA, USA). This provides the ability for employment of the 3D fast readouts of the spiral CSI in clinical trials. Currently, there are two brain diseases that are being metabolically evaluated using the spiral CSI package: 1. Late-onset Tay Sachs (LOTS); and 2. Brain tumor (glioblastoma multiformey). The first one is a collaboration with Dr. Eichler (Department of Neurology, MGH, Boston, MA), while the second one is in collaboration with Dr. Andronesi and Dr. Sorensen (Department of Neurology, A.A. Martinos Center for Biomedical Imaging, MGH, Boston, MA). At this time, these studies are at their initial steps, so only preliminary data are presented.

3.4.1 Spiral CSI in Late-onset Tay Sachs (LOTS)

Late-onset Tay Sachs (LOTS) is a rare lysosomal storage disorder resulting from mutations of the subunit of the lysosomal enzyme ß-hexosaminidase A, which catalyzes the degradation of GM2 ganglioside [97]. On conventional MRI, supratentorial brain structures appear completely normal. However, on postmortem examination, gangliosides are found throughout deep cerebral nuclei. Previous attempts to explore the metabolite contents on LOTS were performed by Inglese et al. [98], using single slice phase-encoded CSI. In this study, we set out to investigate metabolic abnormalities in individual supratentorial brain regions volumetrically, using 3D spiral CSI at 3T.

We applied the fast readouts of the spiral CSI in 2 patients with LOTS (2 men, age range 38-45 years) and 3 healthy age matched controls on a 3T Siemens MRI system (all signed the consents forms approved by the IRB of our institution). The imaging exams consisted of a 3-plane localizer, and 3D T_2 and T_1 (MPRAGE) weighted acquisitions. The spiral CSI acquisitions used constant density spiral trajectories appended to a standard PRESS-box excitation placed wholly within the brain over 5cm

thick slice-selective slab. Six outer-volume saturation (OVS) bands were used to minimize lipid contamination. With FOVxy = 24cm, FOVz = 12cm and encoding matrix of (x,y,z) = (32,32,16), the overall isotropic voxel size was 0.42cc. The spectral bandwidth was 1.2 KHz, encoded over 512 samples along the frequency axis. The spiral designs used gradient slew rate and amplitude of 120 mT/m/ms and 10mT/m, respectively, for a total imaging time of 16.5 minutes (TR = 2s, TE = 144ms, 2 averages).

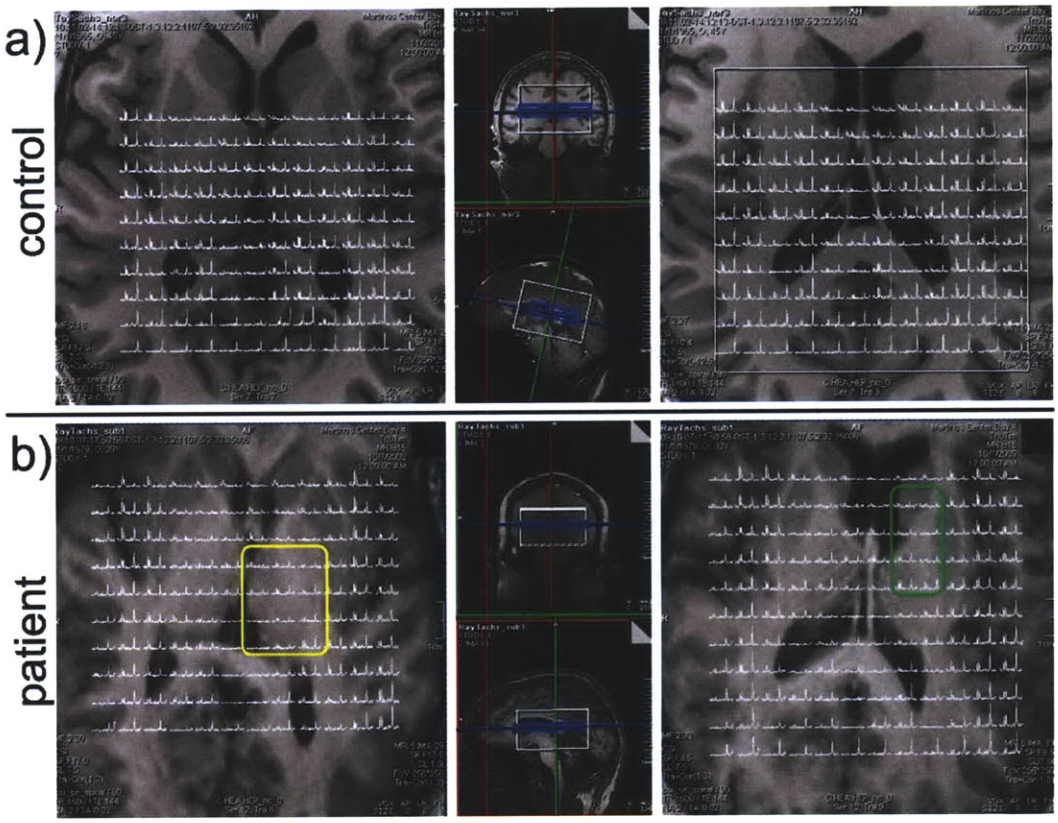

Figure 3-7: Spectral grids from two matching slices from 3D spiral CSI acquisitions on a) LOTS patient and b) control subject (age matched) overlaid on high resolution T_1 weighted acquisitions. It was found that, when compared to controls, LOTS patients had significant elevations in Cho/Cr within the thalamus (yellow box, bottom left image) and basal ganglia (green box, bottom right image).

Five brain regions were assessed (basal ganglia, thalamus, corpus callosum, occipital and parietal cortex) and metabolite ratios (NAA/Cr, Cho/Cr) of spectra in 3 voxels per brain region were measured. For statistical analysis, a mean ratio was calculated for each brain region and metabolite. Overall differences between LOTS and healthy subjects were assessed with repeated measure (brain region) ANalysis Of VAriances (ANOVA)s. Additionally, differences within each brain region were analyzed with a multivariate ANOVA.

Figure 3-7 show spectral grids from two matching slices of a 3D spiral CSI acquisition from one control (Figure 3-7a) and one patient (Figure 3-7b). All supratentorial brain structures appeared normal on structural imaging. However, metabolic abnormalities were found throughout the neuroaxis. Cho/Cr of LOTS patients was significantly elevated compared to normal controls (122%, $p<0.01$). A subsequent ANOVA revealed elevation in basal ganglia (121%, $p=0.05$), and thalamus (127%, $p<0.01$). Reductions in NAA/Cr were found in the cortex (79%) and basal ganglia (87%) but did not reach statistical significance. There was a trend within the corpus callosum towards reduced NAA/Cr (79%) and elevated Cho/Cr (123%).

3.4.2 Spiral CSI in brain tumors

The potential of CSI is significant for improving diagnosis or treatment follow up in clinical conditions of brain tumors [11, 99], where invasive (biopsies) and other serial metabolic imaging (e.g. Positron Emission Tomography) investigations are limited. Employment of volumetric CSI acquisitions using the spiral CSI readouts, appended to the LASER [88] localization excitations, could potentially provide more insight compared to the routinely used single voxel spectroscopy, or single slice PE CSI acquisitions..

3D spiral CSI of brain was performed on five healthy volunteers (three males and two females, 21-30 years, median age 26) and five patients with brain tumors (4 males and 1 female, 24-65 years, median age 59.5). The selected patients were diagnosed by histopathology to have glioblastoma multiforme (GBM) prior to MRS investigation. The inclusion criteria were to have a tumor that has at least 1 cm diameter on the contrast enhanced T_1 weighted image. Exclusion criteria were tumors that presented large areas of blood products due to post biopsy hemorrhage. In addition to the CSI scans, two T1 (MPRAGE) weighted acquisitions were acquired. The first one was used as a reference to the second, which was acquired post-Gd (Magnevist) contrast administration. All subjects signed the consent forms approved by the IRB of our institution.

With $FOV_{XY} = 16cm^2$, $FOV_Z = 8.8cm$, FOVf = 1200Hz, and the 4D encoding matrix set to (x,y,z,f) = (22x22x12x512), the voxel size acquired using the spiral CSI readout was set to the isotropic 0.38cc. The overall scan was only 4.8min using 2 averages and TR = 1s. The rather short TR was used due to the limited time allocated to the overall protocol, which was limited by the clinical schedule to 45 minutes. The LASER excitation scheme (TE = 45ms) was prescribed wholly within the brain, covering a VOI of size

(x,y,z) = (8x8x4)cm^2, enough to both include the tumor and the symmetrical contralateral brain, and not to excite the skull.

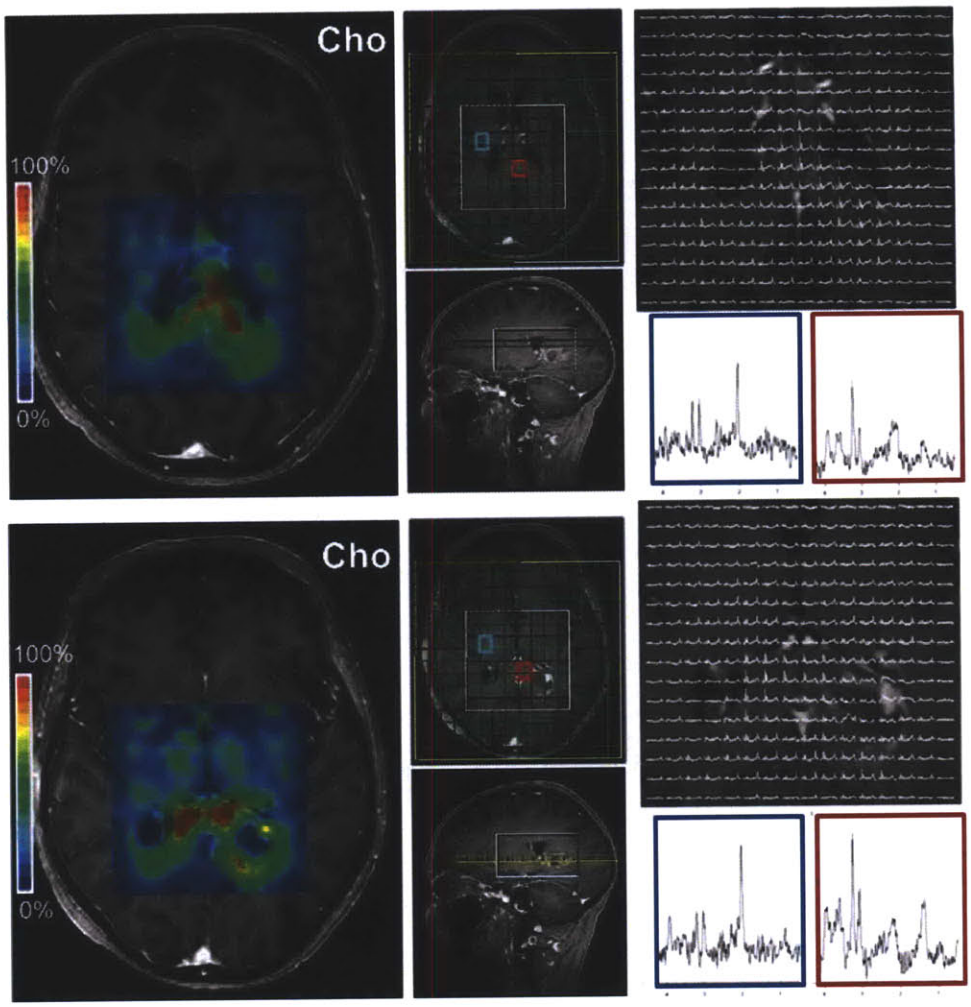

Figure 3-8: 3D spiral CSI from a patient with a brain tumor (GBM). The spectral grids and examples of spectra from voxels located in the healthy brain (outlined in blue) and in the tumor (outlined in red) are shown for two slices. The decrease of the NAA and the increase of choline is evident in brain tissue.

Figure 3-8 show spectra for two of the slices which corresponded to the middle of the enhancing tumor and above the enhancing margin. The positions of the FOV and VOI for each slice are shown on axial and sagittal MPRAGE cross-sections. Examples of spectra from voxels in the healthy brain (blue outlined) and tumor (red outlined) indicate some NAA decrease, but more importantly, a significant choline increase. Due to the high resolution of the spectroscopic data, the choline maps shown for both slice positions provide solid separation between the areas of high choline tumor metabolism and the area of necrosis or ventricles. Importantly, the choline maps show active tumor beyond the margins of the contrast enhancing region.

3.5 Conclusions

For any user specified spectral-spatial imaging parameters, the spiral CSI software package calculated the constant density spiral trajectories in real time, acquired the non-uniformly sampled spectroscopic k-space data, and reconstructed it on Cartesian grids in a time-efficient manner. Due to its usefulness in obtaining volumetric CSI data in acquisition times permissive for clinical *in vivo* measurements, we have given the developed code to Siemens Healthcare (Erlangen, Germany), in order to officially release it as a Work In Program (WIP) package. The WIP package is a form of software release that Siemens (with an authorization of the code developer), can distribute to research and clinical sites so it can be more widely used. All the necessary documentation, including a User Manual, has already been written, and soon, this WIP can be used by any research lab using Siemens scanners.

Furthermore, the results presented in this chapter showed successful employments of the spiral CSI software package on 3T Siemens scanners in clinical settings. Our preliminary studies in LOTS patients reveal alterations in supratentorial metabolism within brain regions that appear normal on conventional MRI. The decreases in NAA/Cr and increases in Cho/Cr presented may reflect neuroaxonal injury and gliosis respectively, consistent with previous reports on the pathology of LOTS.

In the brain tumor studies, we have shown that 0.38cc volumetric CSI is feasible in only ~5min of scanning, a time which allows its routine employment during every clinical scanning session. Furthermore, due to its volumetric coverage, the proposed acquisition can be particularly useful for obtaining metabolite information in the cases where the brain tumor is spread across multiple brain regions.

More spiral CSI acquisitions on various patient populations are underway. Besides the mentioned LOTS and GBM brain tumor patients, we are also starting a pediatric study exploring the metabolite distribution on children (4-12 years old) who are genetically preconditioned to be diagnosed with X-linked adrenoleukodystrophy (ALD). Previous studies [10, 100] have shown that spectroscopic imaging is able to identify impending or beginning degeneration in white matter (characteristic for ALD), that still appears normal on conventional MRI. Therefore, the premise in this pediatric study is to use spiral CSI as a technique for earlier prediction of lesion progression on MRI in X-linked adrenoleukodystrophy.

Chapter 4

Background: Acquisitions on 7T Parallel Transmission (pTx) Systems

4.1 Motivation

The complexity of a given excitation target determines the duration of the designed RF waveforms. RF pulses that are too long yield excitation patterns that are degraded not only by B_0, T_1, or T_2 effects. Therefore, it is always desirable to design RF waveforms that achieve the target excitation in the least amount of time possible. Moreover, certain desirable excitation targets for clinical imaging (e.g. arbitrary shaped saturation bands, spectral-spatial excitations with curved spatial profile) are practically impossible to achieve on the current MR systems.

Recently, parallel transmission (pTx) systems with independent control over the amplitude and phase on each of the N excitation channels, have been successfully demonstrated as means to reduce RF duration of spatially tailored excitation patterns compared to single-channel implementations. All of the work shown in the chapters that follow was performed on a 7T MAGNETOM Siemens scanner equipped with eight independent transmit channels. This system is part of the A.A. Martinos Center for Biomedical Imaging at the Massachusetts General Hospital (MGH). Since the process of

data acquisition on pTx systems is more complicated than on conventional single-Tx systems, the main purpose of this background chapter is to give an overview of that process. Specifically, it starts by briefly describing the hardware components involved, followed by the techniques used to estimate the field maps (B_0, B_1^+ and B_1^-). Next, it will touch upon the pTx RF design algorithms, concentrating mostly on the, so-called "spokes" RF pulse waveforms. Lastly, it will emphasize the importance of monitoring and management of the local specific absorption rates (SAR) in pTx systems, which naturally motivates the work presented in the next chapter.

4.2 pTx Hardware

Unlike the conventional single-Tx scanners, pTx system have multiple transmit channels. Our 7T Siemens scanner uses eight independent RF Power Amplifiers (RFPAs), each capable of transmitting 800W of power with maximum transmit voltage of 200V. Furthermore, the system is equipped with high-performance head-insert gradients, capable of reaching maximum gradient amplitude and slew rate of 80mT/m and 400mT/m/ms, respectively. Each of the RFPAs' output is connected to a directional coupler (called TALES® on the Siemens systems) which monitors the forward and reflected power in real time, and detects possible RFPAs mishaps. The signals from the RFPAs are connected through the coil feeder panel to the custom made transmit coil array. The received signals from the RX-coil are sent to the receiver, after going through optional 20dB attenuation (controls the 'low/high' gain of the receiver). Rough schematic of the system layout (including the path for signal reception) is given in Figure 4-1a.

A desirable feature of pTx is orthogonality of the spatial B_1^+ profiles (greater orthogonality allows greater acceleration factors). Hence, the TX-coil array is built to reduce coupling among coil elements. The most common way to achieve the desired decoupling is via capacitive means [101]. Figure 4-1b shows the 8-channel TX gapped loop array used in all the experiments shown in this thesis, except for the results shown in Chapter 6, where we used the 16-channel TX strip-line array (Figure 4-1c). When the former coil array was used, a separate 8-channel receive coil array was used for signal reception (which can be seen inside the TX array in Figure 4-1b). These coil arrays were build by our collaborators from the RF lab at the A.A. Martinos Center for Biomedical Imaging, MGH [102].

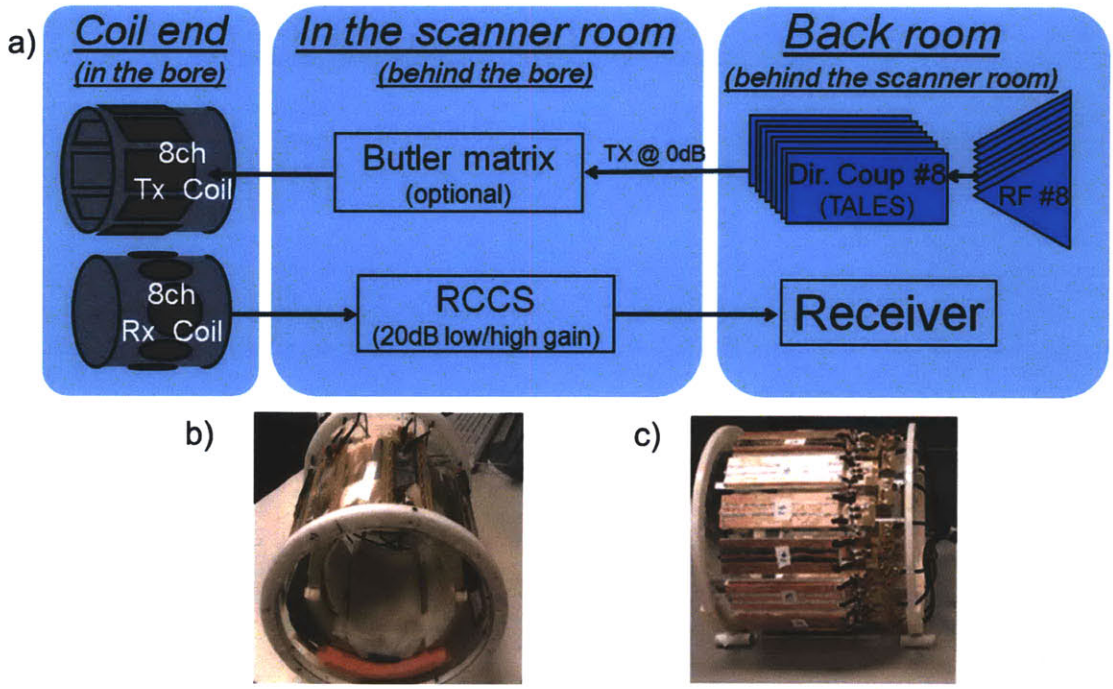

Figure 4-1: a) Schematic of the 8-channel pTx system and b) the 8-channel transmit coil array used for most of the experiments in this thesis; c) The 16-channel strip-line coil array used for the work presented in Chapter 6.

4.3 B_1 and B_0 field mapping

Estimation of the transmit (B_1^+) fields is a requirement for pTx experiments. Furthermore, the accuracy of the maps' estimates is essential for achieving the designed spectral-spatial excitation patterns on the scanner. For further experimental accuracy, it is also highly desirable to get an estimate of the main field's (B_0) inhomogeneities, as many excitation targets, particularly for CSI applications, are sensitive to B_0 effects. Hence, every pTx experiment starts with the "field mapping session", which consists of a series of acquisitions that are ideally short in time, and provide reliable and accurate estimate of the B_1^+ and B_0 fields.

Estimation of the B_0 field is fairly straightforward and fast. It requires data acquisition at two echo times, say TE_1/TE_2 = 5ms/6ms, yielding two images, Im_{TE1} and Im_{TE2}, respectively. The estimated B_0 field at a particular spatial location (x,y), is then given by $B_0(x,y) = \varphi(x,y)/(2\pi \cdot \Delta TE)$, where φ is the phase term of $Im_{TE1} \cdot conj(Im_{TE2})$, and $\Delta TE = TE_2 - TE_1$. The B_0 map is given in units of Hertz, and gives the deviations from the resonant frequency (~297.18Hz at 7T) as a function of space. Note that in order to get a

good phase estimate at all spatial locations, the dual-echo acquisitions are usually performed on a uniform transmit mode, like the birdcage mode. Furthermore, since the B_0 estimate calculation depends on the difference of the two echo times, the repetition times (TR) of the sequence used can be made short, making the B_0 estimation process fast. An example of an in vivo B0 map is given in Figure 4-2a.

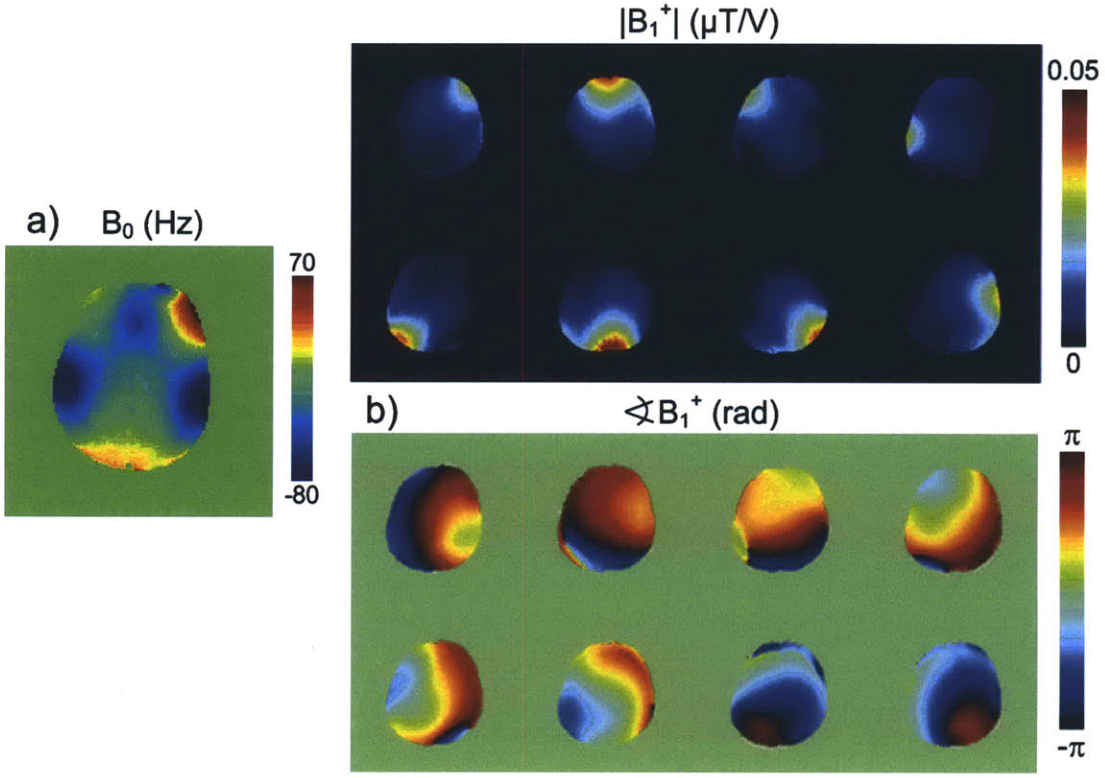

Figure 4-2: a) Estimated *in vivo* B0 map; b) *In vivo* B_1^+ maps (magnitude and phase) of the 8 elements of the transmit coil array (shown in Figure 4-1b) estimated using the methods described in [103].

Compared to single-Tx systems, B_1^+ mapping of the individual TX elements in parallel transmission is more involved, mainly because of the severely inhomogeneous (i.e. localized) spatial profiles of the transmit coil array's elements. Hence, conventional magnitude-based B_1^+ mapping techniques, such as the multi-angle method [104-105], saturation angle method [106-107], or Actual Flip-angle Imaging (AFI) [108], have poor SNR or require acquisition of more images if applied on one transmit channel at a time. The B_1^+ mapping method that was used for all the pTx experiments done in this thesis can be thought of as a hybrid between the ones shown in [107] and [104]. In essence, it requires two sets of acquisitions and several calculation steps that at the end generate estimates of both the transmit (B_1^+) and receive (B_1^-) profiles. Next, I give a brief explanation of the methods used (more details can be found in [103]).

The first acquisition collects eight low flip angle images (one per each transmit channel) which are used to create a combined mode by linearly combining them, such that the maximum to minimum ratio of the combined image is minimized. The purpose of this step is to avoid dynamic range problems when estimating the B_1^+ at locations with low SNR. The intensity of each of these images is given by:

$$\boldsymbol{I_n(x,y) = \rho(x,y)RX(x,y)\sin(\theta_n(x,y)),\ \ n = [1 \ldots 8]} \qquad \textbf{(4-1)}$$

where $\rho(x,y)$ is the tissue density, $RX(x,y)$ is the coil's receive profile and $\theta_c(x,y)$ is the flip angle map of the n-th channel, to be estimated.

Then, a second acquisition operated in the combined mode (by simultaneously transmitting through all transmit channels scaled by the amplitude and phase terms found earlier) obtains: 1. A reference, low flip angle image of the combined mode, or $I_{ref}(x,y) = \rho(x,y)RX(x,y)\sin(\theta(x,y))$; and 2. Several (m) saturation images, each acquired with different flip angle of a saturation pulse that precedes the excitation, or $I_{sat}(x,y) = \rho(x,y)RX(x,y)\sin(\theta(x,y))\cos(m\theta_s(x,y))$. In $I_{ref}(x,y)$ and $I_{sat}(x,y)$, $\theta(x,y)$ and $\theta_s(x,y)$ are the flip angles of the excitation and saturation, respectively. Since at least one saturation image is acquired, $\theta_s(x,y)$ can be estimated by fitting a cosine curve to $I_{sat}(x,y)/I_{ref}(x,y)$ for every (x,y) position. Once $\theta_s(x,y)$ is known, it is straightforward to get the excitation flip angle map of the combined mode $(\theta(x,y))$, as well as the product of $\rho(x,y)RX(x,y)$. Lastly, knowing $\rho(x,y)RX(x,y)$ we go back to $\boldsymbol{I_n(x,y) = \rho(x,y)RX(x,y)\sin(\theta_n(x,y)),\ \ n = [1 \ldots 8]}$ (4-1) and the individual flip angle maps $(\boldsymbol{\theta_n}(x,y))$ for all transmit channels can be obtained.

Example of *in vivo* B_1^+ maps (magnitude in μT/V, phase in radians) estimated using the procedure described, is shown in Figure 4-2b (magnitude/phase in top/bottom of the figure). Note that these methods assume that we operate in a regime without any T_1 effects. To fulfill this constraint, the set of saturation images ($m = 5$ for this example) were acquired with TR of 20s (i.e. > 5 time more than the longest T_1 measured in the head). The TR of the low flip angle acquisitions on the other hand, was set to 2s, due to the fact that excitation of several degrees does not tip the magnetization to an extend that can cause T_1 weighting effects. Therefore, the total time to acquire all the images needed to calculate the B_1^+ map was estimated to (5·20s + (8+1)·2s) = 118s or less than 2 minutes, which is an acceptable time for *in vivo* acquisitions.

Once the estimates of both the B_0 and the B_1^+ maps are obtained, they are then used as inputs of the pTx RF pulse design algorithms. The next sections discuss the RF pulse design methods that are mostly related to the work in this thesis.

4.4 pTx RF pulse design methods

All of the pTx RF pulse design algorithms use the extra degrees of freedom provided by the additional transmit channels (i.e. the extra RFPAs) to "accelerate" a given single-channel excitation, such that the resulting RF pulse durations are R times shorter and the quality of the resulting excitation target is not compromised. R represents the acceleration factor, such that R < N.

Most of the currently used pTx pulse design methods are based on the Transmit SENsittivity ENcoding (SENSE) algorithm [109-111]. While the original SENSE algorithm [112] was developed to speed up the readout portion of the MRI experiment by using the sensitivity maps of the receive coils arrays, Transmit SENSE uses the spatial patterns of the B_1^+ (transmit) profiles of the transmit coil array to speed up (shorten) the excitation schemes. Having N transmit channels, the formulation of the spatial excitation profile given in equation $\boldsymbol{m_{xy}(\bar{r}) = i\gamma m_0 \int_0^T b_1(t) e^{i\bar{r}\bar{k}(t)} dt}$ (2-7) extends to:

$$\boldsymbol{m_{xy}(\bar{r}) = i\gamma m_0 \sum_{n=1}^{N} S_n(\bar{r}) \int_0^T B_{1,n}(t) e^{i\bar{r}\bar{k}(t)} dt} \quad \textbf{(4-2)}$$

where $S_n(\bar{r})$ is B_1^+ sensitivity profile for the n-th transmit channel. Discretizing in both space and time, and still assuming the low tip angle approximation [69], $\boldsymbol{m_{xy}(\bar{r}) = i\gamma m_0 \sum_{n=1}^{N} S_n(\bar{r}) \int_0^T B_{1,n}(t) e^{i\bar{r}\bar{k}(t)} dt}$ (4-2) can be formulated as $m = Ab$, where A incorporates the B_1^+ coil profiles modulated by the Fourier kernel due to the excitation k-space traversal, m is the (spectral-) spatial target profile, and b contains the RF waveforms. Therefore, in its essence, the pTx RF design is an optimization problem that tries to find the estimates of b, (i.e. the N RF waveforms) that give the best target excitation m, given A, and a particular cost function. One way to solve for b is by using conventional least squares (LS) optimization, i.e. $b = arg_b \min [\|Ab - m\|^2 + \lambda(b)]$, where $\lambda(b)$ is the regularization term that can be used to control the integral of the RF pulse and its peak voltage.

For many imaging applications, the phase profile of the excited region is not of a particular interest. Taking advantage of this observation, Setsompop et al. [113] have proposed the magnitude least square (MLS) optimization of b, i.e. :

$$\boldsymbol{b} = \boldsymbol{arg_b min}\,[\||\boldsymbol{Ab}| - \boldsymbol{m}\|^2 + \boldsymbol{\lambda(b)}] \quad \textbf{(4-3)}$$

In [113] it was shown that for a given RF pulse shape, the MLS design outperformed the LS equivalent by achieving more uniform magnitude excitation profile, at a cost of less uniform phase profile, which, as mentioned previously, is not critical in many *in vivo* applications.

4.4.1 pTx spokes RF waveforms

Imaging at high field strength (e.g. 7T) suffers from severe B_1 inhomogeneities that manifest as a significant signal variation within the volume of interest (VOI) resulting in non-uniform spatial SNR distribution and image contrast [40-42]. Parallel transmission has the utilities to *robustly* correct for these non-uniformities. The most commonly used pTX excitations that yield uniform excitation are the so-called "spokes" RF pulses, where multiple sinc-shaped RF pulses are played at particular locations in excitation k-space.

The idea behind the spokes excitation is that, rather than using the conventional way of playing a single sinc pulse (which, in a low-flip-angle view of RF excitation, deposits RF energy only at DC in excitation k-space), correcting for the B_1^+ inhomogeneities can be better achieved if multiple sinc pulses are played at different excitation k-space frequencies (DC can be also included), so that the final excitation is a better representation of the excitation target's spectral contents. Figure 4-3 shows an example of a typical 4-spokes pTx excitation scheme. G_x and G_y gradients (Figure 4-3b) are used to traverse the k_x-k_y excitation space and get to the desired k-space locations (shown in the top image of Figure 4-3a). At these times, the slice selective RF-sinc pulses (accompanied by G_z gradient for slice selection) are played on each of the 8 transmit channels. RF energy is only deposited along excitation k_z, and for particular (k_x,k_y) positions (as shown by the bold vertical lines in Figure 4-3a), and no RF is played between spokes. The MLS optimization given in $\boldsymbol{b} = \boldsymbol{arg_b min}\,[\||\boldsymbol{Ab}| - \boldsymbol{m}\|^2 + \boldsymbol{\lambda(b)}]$ (4-3) finds the best amplitude and phase terms for each spoke on each TX channel (total of 4·8=32 complex coefficients), such that the mitigated B_1^+ profile is as uniform as possible.

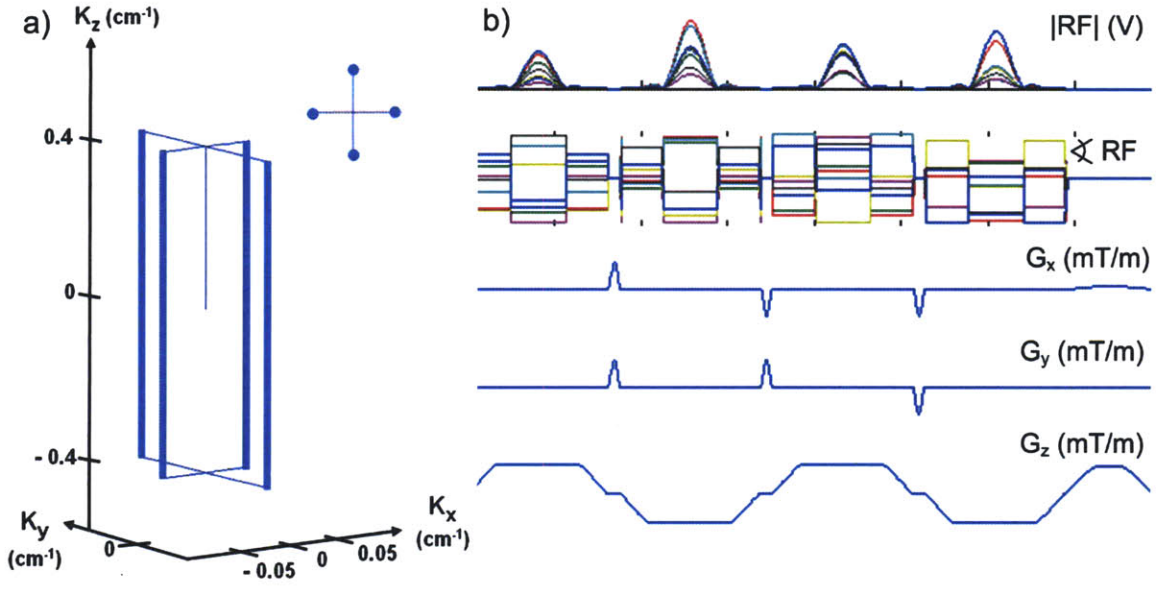

Figure 4-3: a) The excitation k-space trajectory for a 4-spoke excitation. b) The RF and the gradient shapes for the same excitation. G_x and G_y gradients are used to get to a desired k-space locations (shown in the top image of a)), at which times the slice selective RF-sinc pulses (accompanied by G_z gradient for slice selection), are played on each of the 8 transmit channel. The MLS design finds the best amplitude and phase terms for each spoke and each TX channel (total of 32 complex coefficients), such that B_1^+ mitigation is as uniform as possible. (Figure under a) courtesy of Setsompop [113]).

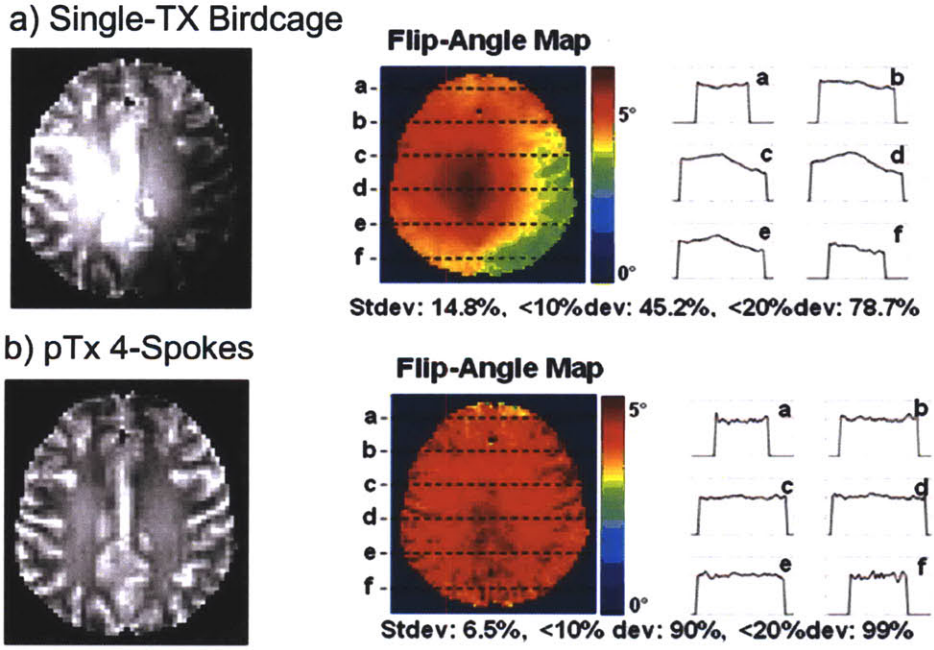

Figure 4-4: B1+ comparison between a) the conventional birdcage (BC) excitation (routinely done on a single-channel systems), and b) the pTx 4-spokes RF excitation. The superiority of the 4-spokes pTx excitation with respect to many uniformity metrics (shown on the right of each image), is evident. (Figure courtesy of Setsompop [104]).

Figure 4-4 shows an *in vivo* comparison between the conventional single-Tx, single sinc birdcage excitation and the pTx 4-spokes RF design. The spatial signal dropout due to excitation RF inhomogeneities in Figure 4-4a is clearly demonstrated, as is the excellent mitigation shown in Figure 4-4b. Looking at the measured flip angle maps shown on the right of the figure, the pTx 4-spokes mitigation provides superior uniformity over the conventional birdcage excitation with respect to several defined metrics. The pTx spokes excitation schemes using the MLS optimization algorithm was the core engine behind all of the RF pulse designs developed for the purposes of this thesis.

4.4.2 Wideband spokes excitation

The spokes excitation mentioned, achieved successful B_1^+ mitigation for the water resonance, but offer inadequate frequency bandwidth to be of use for CSI applications in the brain where the RF design must incorporate B_1^+ mitigation over a wider spectral bandwidth for a proper metabolite excitation. In order to fulfill this extra requirement, [114] proposed an extension to the spokes-based design by extending the $m = Ab$ formulism to N_F specified off-resonances, such that b is now obtained by solving the concatenated set of equations, i.e.

$$\begin{bmatrix} \boldsymbol{m}_{f_1} \\ \boldsymbol{m}_{f_2} \\ \vdots \\ \boldsymbol{m}_{f_{N_F}} \end{bmatrix} = \begin{bmatrix} \boldsymbol{A}_{f_1} \\ \boldsymbol{A}_{f_2} \\ \vdots \\ \boldsymbol{A}_{f_N} \end{bmatrix} \cdot \boldsymbol{b} \qquad \textbf{(4-4)}$$

Figure 4-5 shows the performance of the pTx wideband spokes against the conventional spokes and single-Tx birdcage excitation. The excitation target for all three excitations was a uniform slice-selective B_1^+ mitigation over a 5-cm thick slice and 600Hz of spectral bandwidth. The vertical axis on the figure presents the normalized standard deviation across the entire volume of interest, and represents a metric for spatial uniformity. While the RF shimming method provides equal performance across all frequencies, it is hindered by poor spatial uniformity. Conversely, the conventional spokes achieve pristine spatial uniformity on resonance, but suffer greatly for all off-resonances. At the end, the wideband spokes sacrifices some uniformity compared to the conventional spokes at 0Hz, at the benefit of maintaining that uniformity across the entire target spectral bandwidth (i.e. 600Hz). Variants of this excitation (among other

proposed) were used for the spectroscopic imaging acquisitions presented in Chapter 6 and Chapter 7.

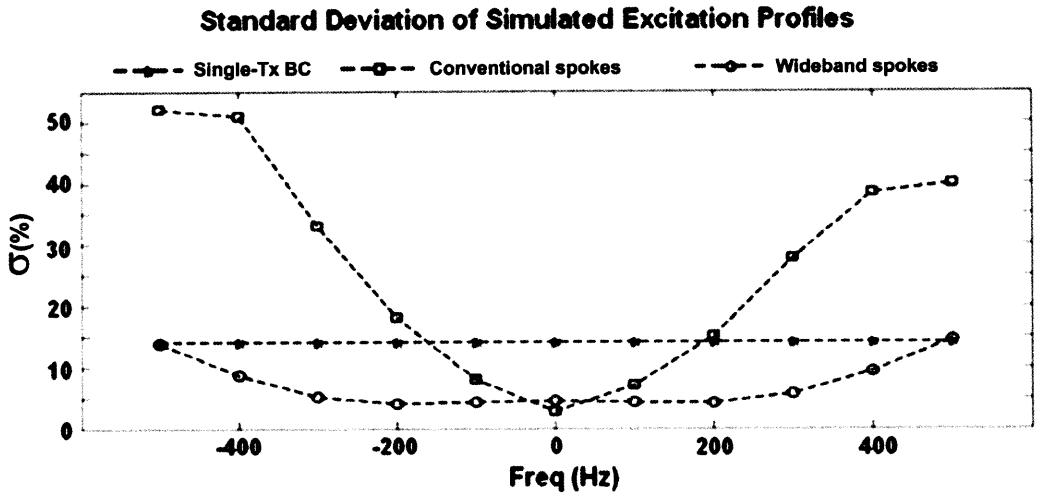

Figure 4-5: Comparing the performance of the wideband spokes against the conventional spokes and single-Tx birdcage (BC) excitation schemes. It can be seen that the wideband spoke excitation sacrifices some uniformity compared to the conventional spokes at 0Hz, at the benefit of maintaining that uniformity across 600Hz of spectral bandwidth (Figure courtesy of Setsompop [114]).

4.5 SAR modeling and simulations

Patient safety concerns in MRI are related to the measure of specific absorption rate (SAR), i.e. the rate at which energy is absorbed by the human tissue when exposed to the RF field played during the excitation phase of an MRI experiment. Therefore, prior to employing the designed excitation to the subject, it is required that this excitation is SAR-checked. Mathematically, the local (spatial) distribution of SAR is given by

$$SAR(\bar{r}) = \frac{\sigma(\bar{r})}{2 \cdot \rho(\bar{r}) \cdot TR} \int_0^{TR} \|E(\bar{r}, t)\|_2^2 \, dt \qquad \textbf{(4-5)}$$

where TR is the time between two consecutive excitations, $\sigma(\bar{r})$ is the conductivity and $\rho(\bar{r})$ is the density of the tissue at location $\bar{r}$, and $E(\bar{r}, t)$ is the electric field generated by the transmit coil $E_c(\bar{r})$, scaled by the RF samples transmitted at each time point, $b(t)$. If L_b is the duration of $b(t)$, then $L_b \leq TR$, and the ratio L_b/TR is known as the duty cycle.

The Food and Drug Administration (FDA) and the International Electrothecnical Commission (IEC) impose limits on: 1. The maximum value of local SAR for 1g ($SAR_{Local-1g}$) [115] or 10g ($SAR_{Local-10g}$) [116] of tissue; and 2. The maximum value of global (averaged) whole-body or whole-head SAR (SAR_{Global}) [115-116]. Table 2 shows the

local and global SAR values for a human head. Looking at $SAR(\bar{r}) = \frac{\sigma(\bar{r})}{2 \cdot \rho(\bar{r}) \cdot TR} \int_0^{TR} \|E(\bar{r},t)\|_2^2 \, dt$ (4-5), the global SAR values are obtained by simply averaging $SAR(\bar{r})$ over all $\bar{r}$, while the 1-gram and 10-gram local SAR maps are obtained by finding the 1-gram and 10-gram volumes surrounding each $\bar{r}$ and then averaging $SAR(\bar{r})$ over all $\bar{r}$ within the cube.

	SAR_{Global}	$SAR_{Local\text{-}1g}$	$SAR_{Local\text{-}10g}$
IEC	3.2 W/kg	/	10 W/kg
FDA	3 W/kg	8.1 W/kg	/

Table 2: IEC and FDA limits for the local and global SAR

r=σ(r)2·ρ(r)·TR0TRE(r,t)22dt (4-5), but now Er,t is the superposition of the electric fields generated by each transmit coil scaled by the RF pulses played on each coil. For N transmit coils, we have

$$E(\bar{r},t) = \sum_{n=1}^{N} b_n(t)\, E_n(\bar{r}) \quad \textbf{(4-6)}$$

Currently, there does not exist a safe and reliable way to directly measure local SAR in humans. Therefore, various electromagnetic (EM) software packages are currently exploited to simulate the electric fields using human models which consist of high resolution conductivity and density maps of the human body. REMCOM® (State College, PA, USA) and SEMCAD® (SPEAG, Zurich, Switzerland), use finite-difference time-domain (FDTD) methods to calculate $E_n(\bar{r})$ - the E field's spatial distribution of the n-th element of the previously modeled transmit coil array. Calculating the complete set of E fields for all the transmit channels can be time consuming, i.e. ~24 hours for 8 coils, on a high-end graphical processing unit (GPU) card. Figure 4-6a shows the conductivity map of the "Ella" model ("Virtual Family", ITIS, Zurich, Switzerland), where the red (blue) colors represent tissues with highest (lowest) conductivity. Figure 4-6b shows the magnitude of axial E fields from the iso-center position of the 8-channel transmit coil array loaded with the Ella head model. For completeness, Figure 4-6c shows the magnitude of the x, y and z vector components of E fields, shown in Figure 4-6b.

Given the simulated E fields, using $\sigma(\bar{r})$ and $\rho(\bar{r})$ from the head models, and REF _Ref277420687 \h $SAR(\bar{r}) = \frac{\sigma(\bar{r})}{2 \cdot \rho(\bar{r}) \cdot TR} \int_0^{TR} \|E(\bar{r},t)\|_2^2 \, dt$

r,t=n=1NbntEn(r) (4-6), one can easily calculate the spatial

SAR distribution for a given pTx RF excitation, $[b_1(\bar{r}) \ldots b_n(\bar{r})]$. This is important, since the calculated values of the maximum local and global SAR are used to determine the minimum TR that is allowed to be used in the sequence, such that the pre-defined IEC limits are not exceeded.

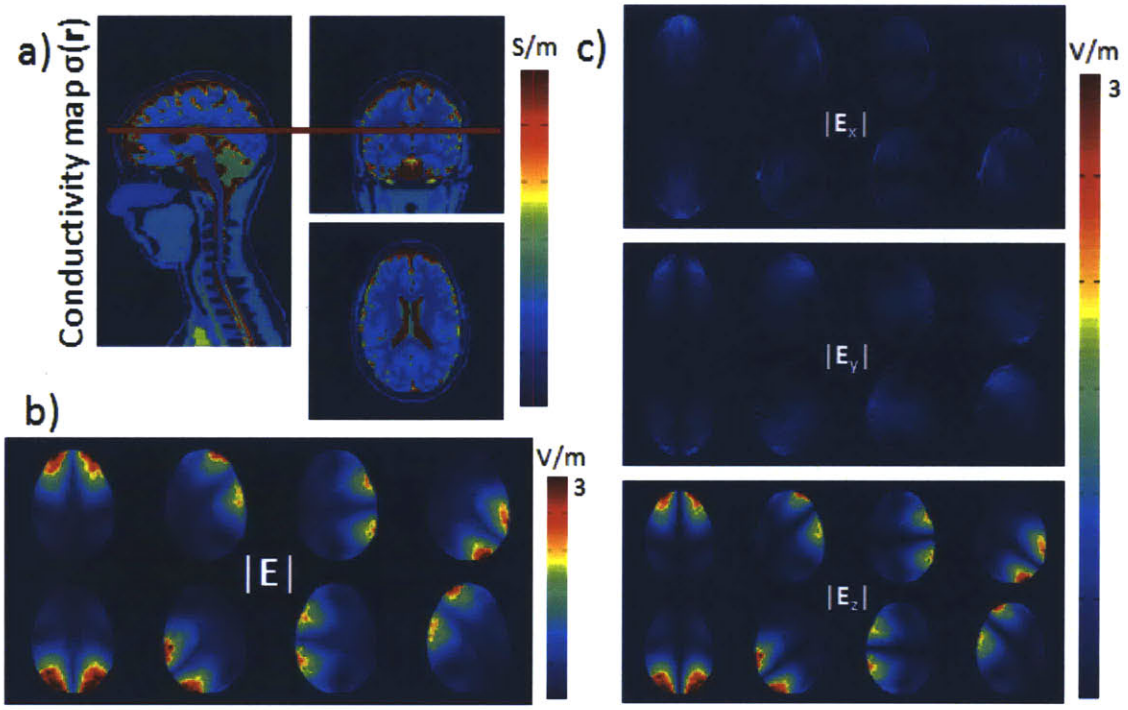

Figure 4-6: a) Conductivity maps, $\sigma(\bar{r})$ of the Ella human model; b) The magnitude of the axial E field vectors for the iso-center position of the 8-channel transmit coil array, loaded with the Ella model; c) The magnitude of the x, y, and z component of the E vector shown in b).

Local SAR depends on the superposition of the electric fields from all the RF waveforms played, therefore, in parallel transmission, assuring patient safety relative to SAR, requires monitoring of the RF waveforms being played on each transmit channel, ideally in real time. This is going to be the main topic of discussion in the chapter to follow.

Chapter 5

Real-Time RF Monitoring in a 7T Parallel Transmit System

5.1 Motivation

In conventional single-Tx system, patient's safety related to SAR is monitored by estimating the delivered power to the tissue averaged over 10s and 6 minute periods. The difference between the measurements of the (forward) power sent by the RF power amplifier (RFPA) and the (reflected) power reflected by the transmit coil, gives an estimate of the power delivered to the tissue, and therefore, indirectly of the amount of tissue heating caused by the given RF excitation. These power measurements are performed by directional couplers (i.e. the TALES units on Siemens platforms) which are placed right next to the RFPA (see Figure 4-1). The system then compares the TALES values to the limits defined by the International Electrotechnical Commission (IEC) (shown in Section 4.5 above), and decides whether the acquisition is patient safe or not. In the latter case, the scan is automatically stopped, and patient safety is assured.

Monitoring the power averaged over given time period is necessary and sufficient requirement for guaranteeing patient safety in single-Tx system. However, this is not the case in parallel transmission. While *lower* TALES values are *always* safe for a patient

scanned on single-Tx system, this is not the case for pTx acquisitions. Since the local SAR distribution in pTx depends on the superposition of the electric fields from all the RF waveforms played, lower TALES values measured on one or more TX channels alter the local SAR maps in a way that does not necessarily imply lower maximum value of the previously simulated local SAR map (as shown in Section 4.5). For example, if one RFPA gets defective during a given pTx acquisition and delivers only half the power, that might actually increase (and possibly shift) the maximum value of the local SAR distribution. Therefore, given the TALES values only, i.e. the measured power averaged over given period of time (e.g. 10s, or 6min), it is hard to draw rational conclusions on whether the given pTx acquisition assures patient's safety or not.

Having said this, there is a need of including an additional layer of monitoring in the transmit chain of each TX channels, in order to better ensure the validity of the simulated SAR estimation. Since the local SAR distribution depends on the RF waveforms being played on each TX channel (as described by $\boldsymbol{E}(\bar{\boldsymbol{r}}, \boldsymbol{t}) = \sum_{n=1}^{N} \boldsymbol{b_n}(\boldsymbol{t})\, \boldsymbol{E_n}(\bar{\boldsymbol{r}})$ (4-6)), it makes sense for this enhanced monitoring system to include measurements of the actual complex RF waveforms monitored for each individual transmit element.

The two most common ways to implement real-time RF monitoring include the usage of directional couplers, or, the so-called pick-up loops. The latter involves placing small wire loops (~5ms in diameter) in near proximity of each transmit coil element, in order to "pick-up" the currents induced by the RF waveforms played. Previous successful attempts to use pick-up loops for RF monitoring are given in [117-118]. The work presented in this chapter however, focuses on the implementation of the real-time RF monitoring system using directional couplers.

The objective of the work presented in this chapter was to develop a fully functional, real-time RF monitoring system using directional couplers, that tracks and compares RF waveforms on each TX-channel to the expected digital pulse waveforms and shuts down the scan in the event of a mismatch due to e.g. a broken coil, RF amplifier failure, phase discrepancies, or other spurious sources of pTx RF errors. Furthermore, it investigated subject-to-subject variation in excitation coil array monitoring parameters and used these findings to propose threshold criteria that identified the detected RF mismatches that could potentially be harmful to the subject being scanned. Calibration of the cut-off values needed in the threshold algorithm was done empirically by monitoring the RF

signals in 15 *in vivo* measurements. The performance of the proposed algorithm was then tested for different types of RF pulses in undisturbed and purposely disturbed acquisitions. Once the given proposed threshold was exceeded, the measurement was successfully stopped in real time with at most 10 ms latency.

5.2 pTx system layout with real time RF monitoring

Eight directional couplers (DiCos) were used to measure the forward and reflected power to an 8-channel transmit coil array for our MAGNETOM 7T (Siemens Healthcare, Erlangen, Germany) with an 8-channel prototype pTx system. Compared to the directional couplers already present in the Siemens systems (i.e. the TALES units), which remained to measure the power averaged over 10s and 6min time periods, these newly added DiCos were placed as close to the transmit coil elements as possible. Our original system's layout shown in Figure 4-1, is now updated to include the DiCos in the TX-RX chain, as shown in Figure 5-1. Here, it can been seen that the received monitoring signals were attenuated by 60dB at the receiver, which was the level necessary to allow transmission at 200V simultaneously on all 8 channels without clipping artifacts. The value of 200V was the maximum voltage that each of the 8 RFPAs could deliver. After being fed to the standard receiver, the monitored signals were processed by the online scanner image calculation environment, which is able to stop the sequence at a time when predefined error thresholds are reached. The shutdown reaction time is guaranteed to be less than 10 ms.

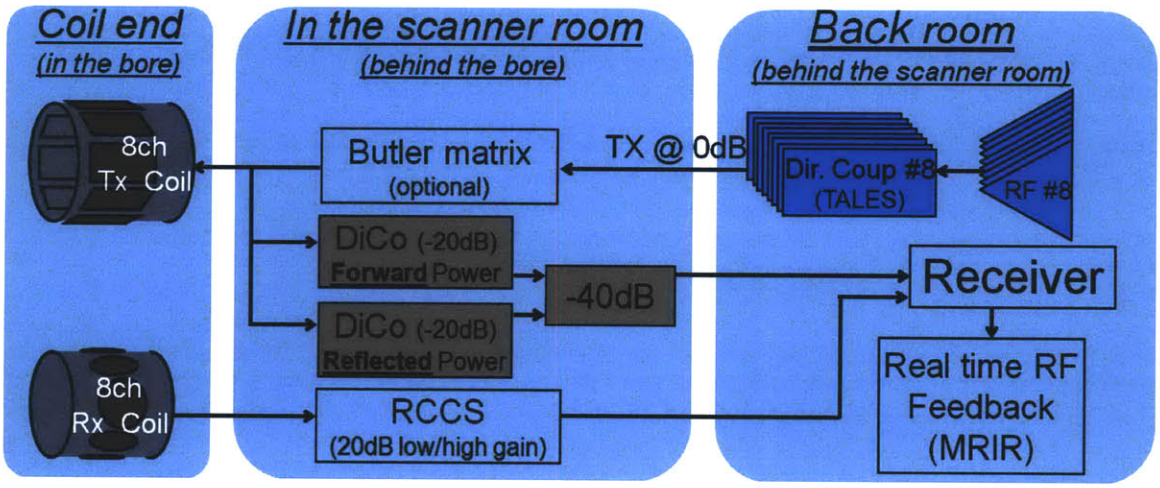

Figure 5-1: Schematic of the 8-channel pTx system including the real time monitoring system using directional couplers that measure the forward and reflected power close to the transmit coil array. The 60 dB

attenuated monitored signals were fed to the standard receiver, and processed by the online image calculation environment capable of stopping the acquisition in real time if the error thresholds are reached.

5.3 The coupling matrix

Transmission of RF on TX-channel *k* generates non-trivial monitoring signals on all 8 channels due to coil coupling. To account for these coupling effects and resolve independent pTx waveforms by observation of the monitoring signals from the DiCos, a separate calibration step preceded the pTx exam to estimate the full complex-valued 8x8 coupling matrix. Note that the coupling patterns are different for the forward and reflected monitored signals, so two separate matrices are estimated. Row *k* (*k*=1…8) of each coupling matrix is generated by playing an RF pulse on channel *k*, and receiving forward/reflected data through all 8 DiCos, followed by a least-squares estimate of 8 complex-valued weights that relate the forward/reflected transmission to the DiCos, and populate row *k* of the correlation matrix, $\boldsymbol{\alpha}_{FWD}/\boldsymbol{\alpha}_{REF}$. The estimated waveforms are then $\mathbf{b}_{est\_FWD}(t) = TX_{vol} \cdot \mathbf{b}(t) \cdot \boldsymbol{\alpha}_{FWD}$ and $\mathbf{b}_{est\_REF}(t) = TX_{vol} \cdot \mathbf{b}(t) \cdot \boldsymbol{\alpha}_{REF}$, each expressed as an Nx8 matrix (N=number of RF samples), where $\mathbf{TX}_{vol}$ is the maximum voltage and $\mathbf{b}(t)$ are the ideal Nx8 pTx waveforms.

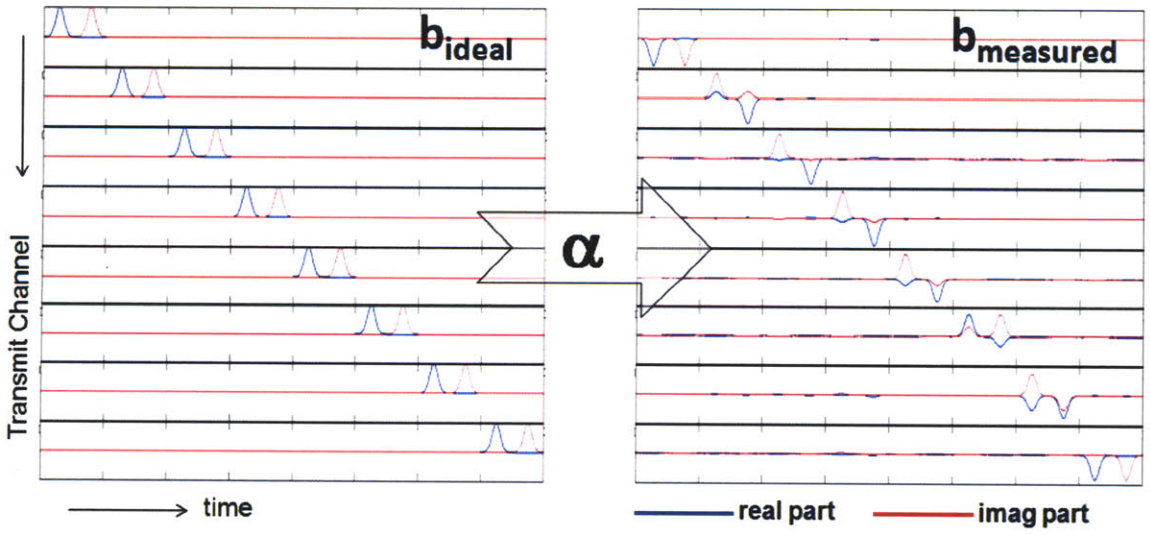

Figure 5-2: The complex [8x8] alpha matrix transforms the ideal waveforms (left) to the monitored signal (right) in the minimum least-square sense.

Figure 5-2 shows the pTx RF excitation used to calculate the alpha matrices. The left image shows Gaussian pulses that were played simultaneously on all 8 TX-channels ([1600x8]). Two Gaussian pulse per transmit channel were played, each of them being

either purely real (blue) or purely imaginary (red). The monitored signals (forward in figure shown) received by the 8 DiCos are shown on the right image ([1600x8]). Then, the alpha matrix is the [8x8] complex-valued matrix that transforms the ideal waveforms (left) to the monitored signal (right) in the minimum least-square sense. The pTx sequence that acquired the data necessary to calculate the alpha matrix, consisted of 32 repetitions (TR = 100ms) of the excitation shown on the left of Figure 5-2, for a total scan time of only 3.2s. This sequence was part of the adjustments portion of the pTx session. While only one TR is really needed to get the coupling matrix, the 32 acquired measurements provided better fits for α_{FWD} and α_{REF}.

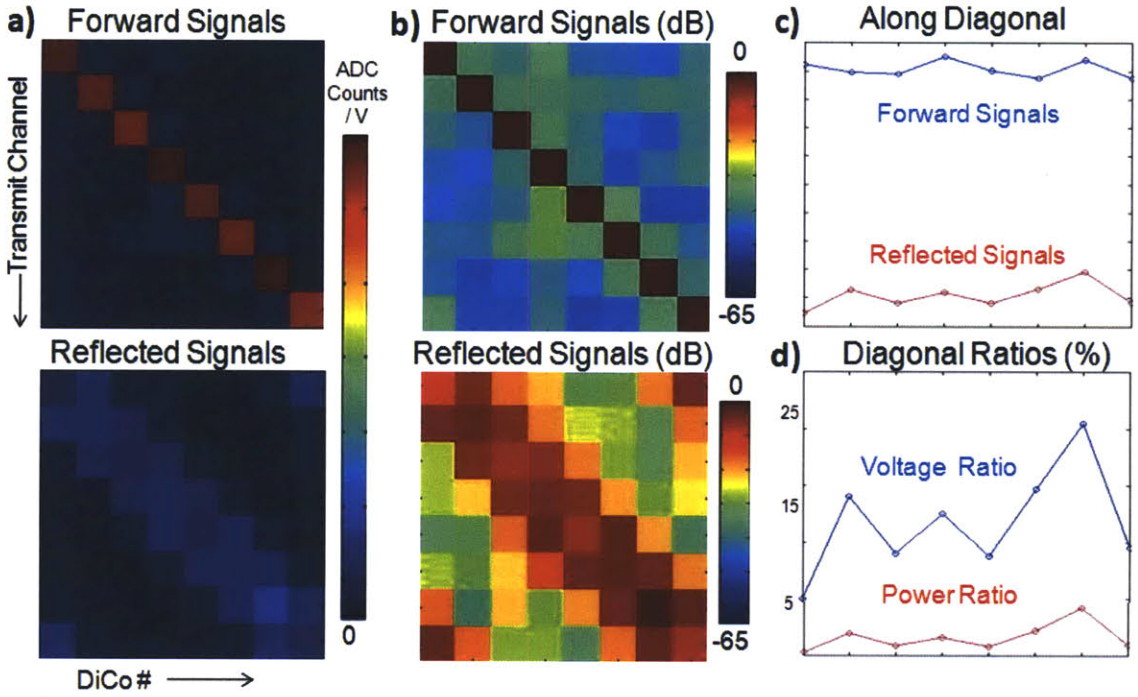

Figure 5-3: a) Examples of the magnitude forward and reflected signals alpha matrix (top and bottom image, respectively); b) Same matrices from a) shown on dB scale; c) One dimensional plots along the diagonal for the forward and reflected power matrices shown in a) (forward = blue line, reflected = red line); d) The voltage and power ratios of the curves shown in c).

Sample examples of alpha matrices are given in Figure 5-3, showing the expected, predominately diagonal pattern. The top and bottom image of Figure 5-3a show the magnitude of α_{FWD} and α_{REF} scaled to the same maximum value. The units of the alpha matrix are given in ADC (or receiver) counts per unit voltage. Figure 5-3b shows a dB plot of the matrices given in Figure 5-3a, seeing that the off-diagonal terms of α_{FWD} are at least 25dB lower in magnitude compared to the diagonal terms, alluding to decent de-coupling of the transmit coil array's elements. Furthermore, Figure 5-3c presents a 1-D

plot of the diagonal terms of α_{FWD} and α_{REF} (blue and red curves, respectively), which ratio is labeled as the "Voltage Ratio" in Figure 5-3d (shown in blue). Squaring the voltage ratio, gives us the power ratio between the diagonal terms of α_{FWD} and α_{REF} (shown in red, Figure 5-3d), which represents a measure of the amount of reflected power observed in our transmit coil array. It is important to note that the sub 5% reflection seen in Figure 5-3d is in correspondence to the amount of reflection observed in this coil array on the bench.

5.3.1 Subject-induced variability in the monitoring signals

Any threshold criteria used to determine the extent to which the monitored DiCos' signals deviate from the ideal RF waveforms, and to decide whether the transmitted RF excitation is reliable or not, would require some cut-off values that would discriminate between the "erroneous" and the "reliable" samples. Calibration of these cut-off values needed in the threshold algorithm was done empirically by monitoring the RF signals in 15 *in vivo* measurements. The goal here was to investigate the subject-to-subject variation in excitation coil array monitoring parameters and use these findings to propose reasonable threshold criteria (discussed later in the chapter), that stop the acquisition if the mismatch between the ideal and observed RF signals is large enough so that patient safety is in question.

The values of the coupling matrices α_{FWD} and α_{REF} vary from one subject to the next due to modulation of the array couplings by loading differences. This is particularly true for the values of α_{REF}. In order to quantify this variability, we collected α_{FWD} and α_{REF} for each of the 15 different subjects scanned, who were asked to position, remove and then re-position their head in the array three times. We analyzed the calibration matrix for the delivered power, $\alpha = (\alpha_{FWD} - \alpha_{REF})$. Defining $\alpha_{mean\_archive}$ as the mean among all the $15 \cdot 3 = 45$ α's, we calculated the [15x3] (15 heads; 3 measurements per head) maximum error vector ε_{max_α}, such that

$$\varepsilon_{max\_\alpha}[n,m] = \max\left[\left|\frac{(\alpha_{n,m} - \alpha_{mean\_archive})}{\alpha_{mean\_archive}}\right|\right], n = [1 \dots 15],\ m = [1,2,3] \qquad \textbf{(5-1)}$$

where $\alpha_{n,m}$ is the m-th alpha matrix measured on the n-th subject. The three plots given in Figure 5-4a show the values from each of the three columns of ε_{max_α}, i.e. the maximum error values in each of the three alpha matrices, measured for every subject. Taking the mean of these three vectors, gives us the maximum error values for each

subject averaged over the three measurements. Looking at this plot, we see that the maximum error value is 4.65% (on subject 3). Adding a slight safety-buffer margin to the calculated error maximum, we declared ***ε_{max} = 5%*** *to be considered as the upper limit of the range of variability present in our monitoring system.* This cut-off value was used in the threshold algorithm to identify the potentially erroneous RF samples.

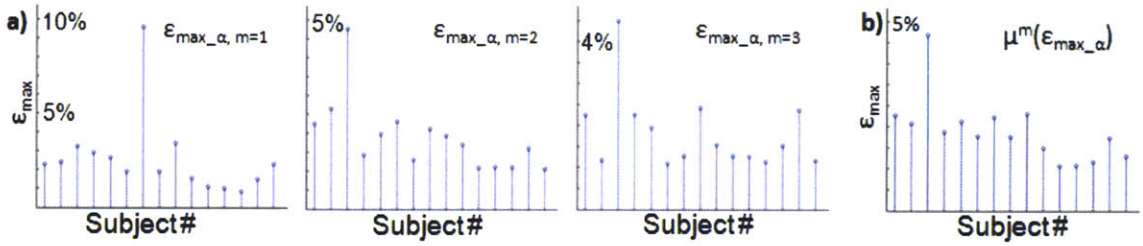

Figure 5-4: a) Three plots showing the three columns of ε_{max_α}, i.e. the maximum error values among all 15 subjects for each of the three measurements performed per subject; b) The [1x15] error vector formed by taking the mean of ε_{max_α} along the second dimension.

Since the coupling matrices do vary slightly from subject-to-subject, and since the pTx acquisition used to calculate $\boldsymbol{\alpha}_{FWD}$ and $\boldsymbol{\alpha}_{REF}$ takes only 3.2s, every new pTx session started with an acquisition of $\boldsymbol{\alpha}_{FWD\_curr}$ and $\boldsymbol{\alpha}_{REF\_curr}$ for the subject being scanned. These matrices, together with ε_{max} were used in the threshold algorithm to be discussed next. Moreover, the value of ε_{max} was used to verify whether our hardware is in a normal, operable state, by calculating the maximum error value between $\boldsymbol{\alpha}_{curr}$ = ($\boldsymbol{\alpha}_{FWD\_curr}$ - $\boldsymbol{\alpha}_{REF\_curr}$) and $\boldsymbol{\alpha}_{mean\_archive}$, i.e. ε_{max_curr} = max[|($\boldsymbol{\alpha}_{curr}$ - $\boldsymbol{\alpha}_{mean\_archive}$) / ($\boldsymbol{\alpha}_{mean\_archive}$)|]. If $\varepsilon_{max\_curr} > \varepsilon_{max}$, we question the state of our hardware and abort the session overall (the subject is not scanned, and the hardware is brought back to the bench). If $\varepsilon_{max\_curr} < \varepsilon_{max}$, we claim that our hardware is in operable state, and we proceed with our experiments.

5.4 The threshold algorithm

For a given set of pTx RF pulses **b**(t), played at a maximum transmit voltage, TX_{vol}, the forward and reflected measured RF signals from the DiCos ($\mathbf{b}_{m\_FWD}$(t) and $\mathbf{b}_{m\_REF}$(t), respectively) are compared against $\mathbf{b}_{e\_FWD}$(t) = $TX_{vol}\cdot\mathbf{b}(t)\cdot\boldsymbol{\alpha}_{FWD\_curr}$ and $\mathbf{b}_{e\_REF}$(t) = $TX_{vol}\cdot\mathbf{b}(t)\cdot\boldsymbol{\alpha}_{REF\_curr}$, by defining the normalized complex error matrix

$$\varepsilon(t) = \frac{[b_{m\_FWD}(t) - b_{m\_REF}(t)] - [b_{e\_FWD}(t) - b_{e\_REF}(t)]}{[b_{e\_FWD}(t) - b_{e\_REF}(t)]} \qquad \textbf{(5-2)}$$

The size of $\boldsymbol{\varepsilon}(t)$ is [N_S x 8], where N_S is the number of samples in the pTx excitation, and 8 is the number of used transmit channels. Then, the proposed threshold algorithm does the following *for every TR of pTx acquisition*:

- Finds $\mathbf{v}_{ind\_\varepsilon}$, the vector of indexes of all RF samples in $\boldsymbol{\varepsilon}(t)$ that exceed the empirically obtained ε_{max} = 5%;
- For the RF samples *at the indexes* $\mathbf{v}_{ind\_\varepsilon}$, assumes the worst case scenario when all the E fields sum constructively, so the maximum 10g-avg local SAR, $SAR_{10g\_local\_curr}$, is further derated by a local SAR term;
- *Stops the measurement in real time if the minimum TR calculated based on new SAR estimate is longer than the TR being used.*

5.4.1 Finding $\mathbf{v}_{ind\_\varepsilon}$

At any given time sample t_0, $\boldsymbol{\varepsilon}(t_0)$ is a [1 x 8] complex vector. If *either the real or imaginary part of any of these 8 samples* exceeds ε_{max} = ±5%, that it is said that the pTx excitation at time t_0 is erroneous. The index of this RF sample is then included in $\mathbf{v}_{ind\_\varepsilon}$. We further define $\varepsilon_{\%}$ to be the fraction of RF samples that exceed ε_{max} = 5%. $\varepsilon_{\%}$ is calculated by dividing the length of $\mathbf{v}_{ind\_\varepsilon}$ with N_S.

5.4.2 Derating the simulated maximum local SAR value

Prior to the pTx acquisition with the given RF excitation, the local SAR distribution, $SAR_{10g\_local\_curr}$, was calculated as described by $\boldsymbol{SAR}(\bar{r}) = \frac{\sigma(\bar{r})}{2\cdot\rho(\bar{r})\cdot TR}\int_0^{TR}\|\boldsymbol{E}(\bar{r},t)\|_2^2\,\boldsymbol{dt}$

(4-5) and $\boldsymbol{E}(\bar{r},t) = \sum_{n=1}^{N}\boldsymbol{b_n}(t)\,\boldsymbol{E_n}(\bar{r})$

(4-6) in Section 4.5. Since the RF samples at time points given in $\mathbf{v}_{ind\_\varepsilon}$ are "not to be trusted", for the vector of RF samples $\mathbf{b}_\varepsilon(t) = \mathbf{b}(\mathbf{v}_{ind\_\varepsilon})$ we assume the worst case scenario when all the E fields from the 8 RF pulses sum constructively, so that the maximum 10g-avg local SAR, $SAR_{10g\_local\_curr}$, is further derated by a local SAR term $SAR_{10g\_local\_\varepsilon}$, such that

$$\boldsymbol{SAR_{10g\_local\_\varepsilon}} = \boldsymbol{P_\varepsilon}/\left(\boldsymbol{r_{worst\_case}}\cdot\boldsymbol{m_{head}}\right) \quad \textbf{(5-3)}$$

where $P_\varepsilon = \sum \boldsymbol{b}_\varepsilon(t)^2/50\Omega$ (50Ω is the assumed impedance), r_{worst_case} is the worst case $SAR_{10g\_local}/SAR_{global}$ for the TX-array used and is typically ~60 [119] and m_{head} = 4kg is the mass of the head. Since $SAR_{10g\_local\_\varepsilon}$ is calculated only for the samples that

constitute a fraction of the total pTx excitation, which fraction is given by the value of of $\varepsilon_{\%}$, then $SAR_{10g\_local\_derated}$, the derated maximum 10g-avg local SAR is given by

$$\boldsymbol{SAR_{10g\_local\_derated} = SAR_{10g\_local\_\varepsilon} \cdot \varepsilon_{\%} + (1 - \epsilon_{\%}) \cdot SAR_{10g\_local\_curr}} \quad \textbf{(5-4)}$$

5.4.3 Stopping the measurements

For a currently designed pTx excitation, the maximum global SAR (SAR_{global_curr}), and the maximum 10g-avg local SAR ($SAR_{10g\_local\_curr}$) values are calculated for 100% of duty cycle (see $\boldsymbol{SAR(\bar{r}) = \frac{\sigma(\bar{r})}{2 \cdot \rho(\bar{r}) \cdot TR} \int_0^{TR} \|E(\bar{r}, t)\|_2^2 \, dt}$ (4-5) for details). Given the IEC-defined values (see Table 2) for the global and 10g-avg local SAR limits, SAR_{global} and SAR_{10g_local}, respectively, we say that the current pTx excitation is local SAR limited if ($SAR_{10g\_local\_curr}$ / SAR_{global_curr}) > (SAR_{10g_local} / SAR_{global}). Otherwise, the pTx excitation is global SAR limited. Then, the minimum TR value that would not violate the IEC-defined limits for *both global and local SAR* will be: 1. TR_{min} = ($SAR_{10g\_local\_curr}$ / SAR_{10g_local})·L_{RF} if the pTx excitation is local SAR limited, and 2. TR_{min} = (SAR_{global_curr} / SAR_{global}) ·L_{RF} if the excitation is global SAR limited. L_{RF} is the duration of the pTx excitation given in seconds.

Since almost all the pTx excitations are local SAR limited, the derated maximum 10g-avg local SAR given in $\boldsymbol{SAR_{10g\_local\_derated} = SAR_{10g\_local\_\varepsilon} \cdot \varepsilon_{\%} + (1 - \epsilon_{\%}) \cdot SAR_{10g\_local\_curr}}$ (5-4) can be used to calculate a new estimate of the minimum TR, i.e. $TR_{derated}$ = ($SAR_{10g\_local\_derated}$ / SAR_{10g_local})·L_{RF}. Then, the final task of this threshold algorithm is to *compare $TR_{derated}$ with the TR_{used}, i.e. the TR being used in the current sequence, and to stop the scan in real time if $TR_{derated} > TR_{used}$.*

5.5 Results

The feasibility of the proposed threshold criteria was tested on pTx excitations using spokes and spiral trajectories. Table 3 presents the performance of the RF monitoring for four acquisitions in undisturbed and purposely disturbed settings, by showing the values for: $SAR_{10g\_local\_curr}$ (abbreviated as SAR_{curr}), $SAR_{10g\_local\_derated}$ (abbreviated as $SAR_{derated}$), TR_{min}, TR_{used}, $TR_{derated}$ and finally the percentage of RF samples with

monitored error values greater than ε_{max} = 5%, $\varepsilon_{\%}$. Note that the values presented were taken from the "worst performing" TR, i.e. the TR with maximum length $\mathbf{v_{ind\_\varepsilon}}$.

The TR used in each of the four acquisitions was $TR_{used} = 1.2 \cdot TR_{min}$, where TR_{min} was calculated as described above. Then, the last column in Table 3 shows the decision of the threshold algorithm for the given acquisition, such that the scan is stopped if the percent of TR increase due to $TR_{derated}$ is greater than 20%, i.e. if $TR_{derated} > TR_{used}$.

The abbreviations of the pTx acquisitions shown in the first column of Table 3 mean the following:

- *pTx1* – undisturbed acquisition using 4-spokes pTx excitation, designed for 30^0 flip angle (L_{RF} = 4.1ms, TX_{vol} = 170V);
- *pTx2* – undisturbed acquisition using spiral-shaped pTx excitation, designed for 40^0 (L_{RF} = 6.42ms, TX_{vol} = 180V);
- *pTx3_dstr* – pTx excitation using 4-spokes trajectories (same RF design used in pTx1), disturbed by purposely adding 0.25m of extra cable on TX-channel #7, in order to change its phase.
- *pTx4_dstr* – pTx excitation using spiral trajectories (same RF design used in pTx2), disturbed by purposely placing a small titanium piece next to the TX-coil element #4, in order to change its tuning.

pTx Exc.	SAR_{curr}	$\varepsilon_{\%}$	$\varepsilon_{\%} \cdot SAR_{derated}$	TR_{min}	TR_{used}	$TR_{derated}$	*Stop?*
pTx1	15.9 W/kg	0%	0 W/kg	6.52 ms	7.82 ms	6.52 ms	NO
pTx2	24.6 W/kg	1.1%	0.77 W/kg	15.75 ms	18.9 ms	16.06 ms	NO
pTx3_dstr	15.9 W/kg	29.3%	422.54 W/kg	6.52 ms	7.82 ms	138.8 ms	YES
pTx4_dstr	24.6 W/kg	12.4%	331.8 W/kg	15.75 ms	18.9 ms	226.1 ms	YES

Table 3: Summary of the performance of the proposed threshold algorithm, for 4 different scans acquired under undisturbed and disturbed conditions using both 4-spokes and spiral pTx excitation trajectories; See the text for more details.

Figure 5-5 and Figure 5-6 show overlaid plots of the measured (blue) and predicted (red) RF waveforms for the excitations 'pTx1' and 'pTx2', respectively. The waveforms (real or imaginary part shown), randomly chosen from different TRs, present the quality of the match between the blue and red curves, which is not surprising and expected, given the fact that these measurements were performed under normal, undisturbed

conditions. Therefore, as seen in Table 3, the real time monitoring system did not stop the scans, as the $TR_{derated}$ did not exceed TR_{used}. While none of the monitored RF samples in 'pTx1' exceeded the cut-off value of ε_{max} = ±5%, this was the case for only 1.1% of the monitored RF samples in 'pTx2'. Note that in pTx2, most of the samples identified as "erroneous" were towards the end of the pulse, where the RF waveform abruptly changed its amplitude (from low to high, or vice versa).

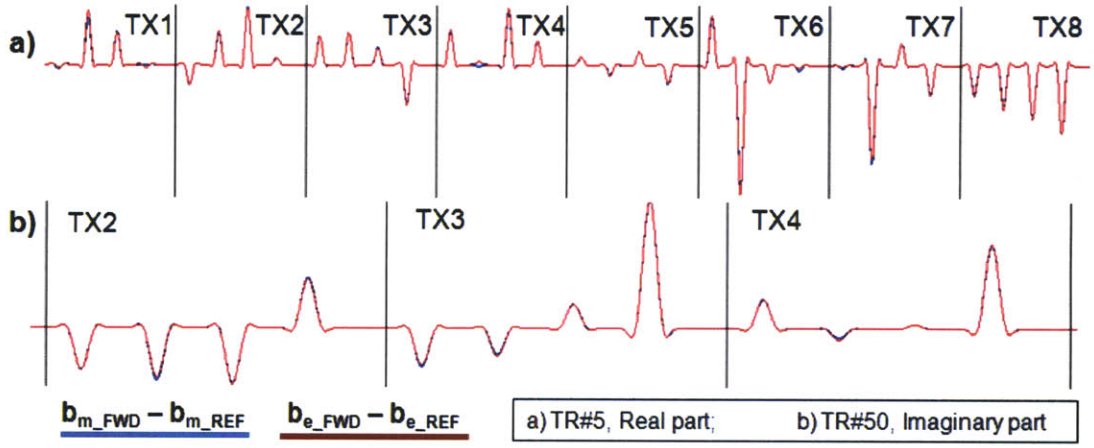

Figure 5-5: Overlaid plots of the monitored (blue) and predicted (red) RF waveforms from acquisition ***pTx1*** for a) the real part of the RF samples from TR#5 (TX1-TX8); b) the imaginary part of the RF samples from TR#50 (TX2-TX4);

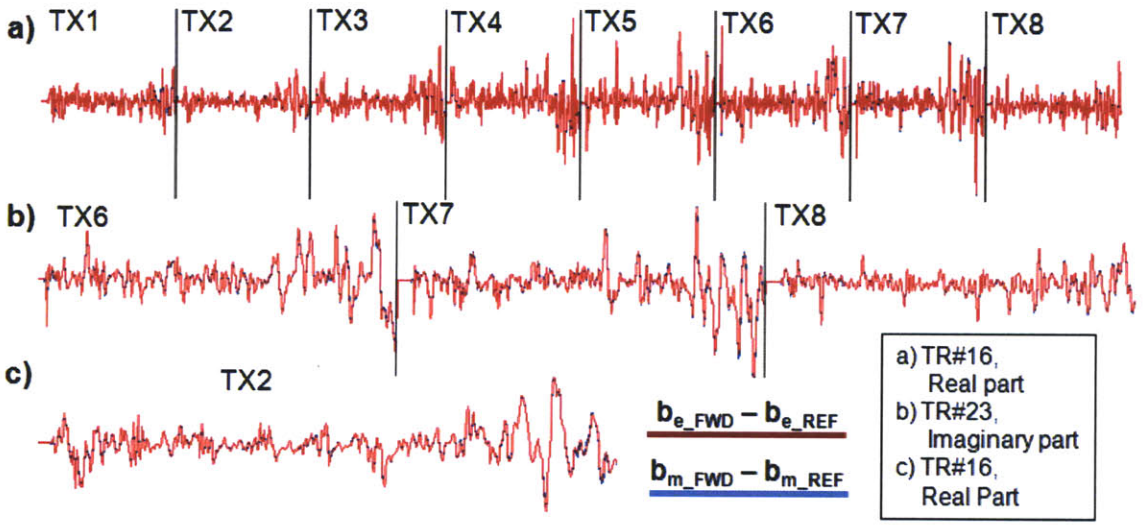

Figure 5-6: Overlaid plots of the monitored (blue) and predicted (red) RF waveforms from acquisition ***pTx2*** for a) the real part of the RF samples from TR#16 (TX1-TX8); b) the imaginary part of the RF samples from TR#23 (TX6-TX8); b) the imaginary part of the RF samples from TR#16 (TX2 only);

Figure 5-7 presents the performance of the RF monitoring for the excitation 'pTx3_dstr', where the phase on TX-channel #7 was purposely altered by adding 0.25m

long cable in its transmit path. The black crosses ('x') in Figure 5-7a, overlaid onto the magnitude plot of the ideal RF waveforms, **b**(t), identify the indexes of the RF samples which the threshold algorithm identified them as erroneous. While, not surprisingly, most of the RF samples played on TX-channel #7 have exceeded the error bar of $\varepsilon_{max} = \pm 5\%$, note that, due to coil coupling, some of the samples of RF waveforms played on the neighboring coils have also been classified as erroneous. Figure 5-7b shows the magnitude and phase overlaid plots of $\mathbf{b}_{m\_FRW}(t) - \mathbf{b}_{m\_REF}(t)$ (blue) and $\mathbf{b}_{e\_FRW}(t) - \mathbf{b}_{e\_REF}(t)$ (red) for the 6th, 7th and 8th TX-channel, where one can clearly see observe the phase jump introduced to TX-channel #7. For this purposely disturbed acquisition, $\varepsilon_{\%} = 29.3\%$ and $TR_{derated}$ is almost 18 times longer than TR_{used}. As expected, the threshold algorithm has successfully caught the introduced phased jump on one of the TX-channels, and has rightfully stopped the acquisition.

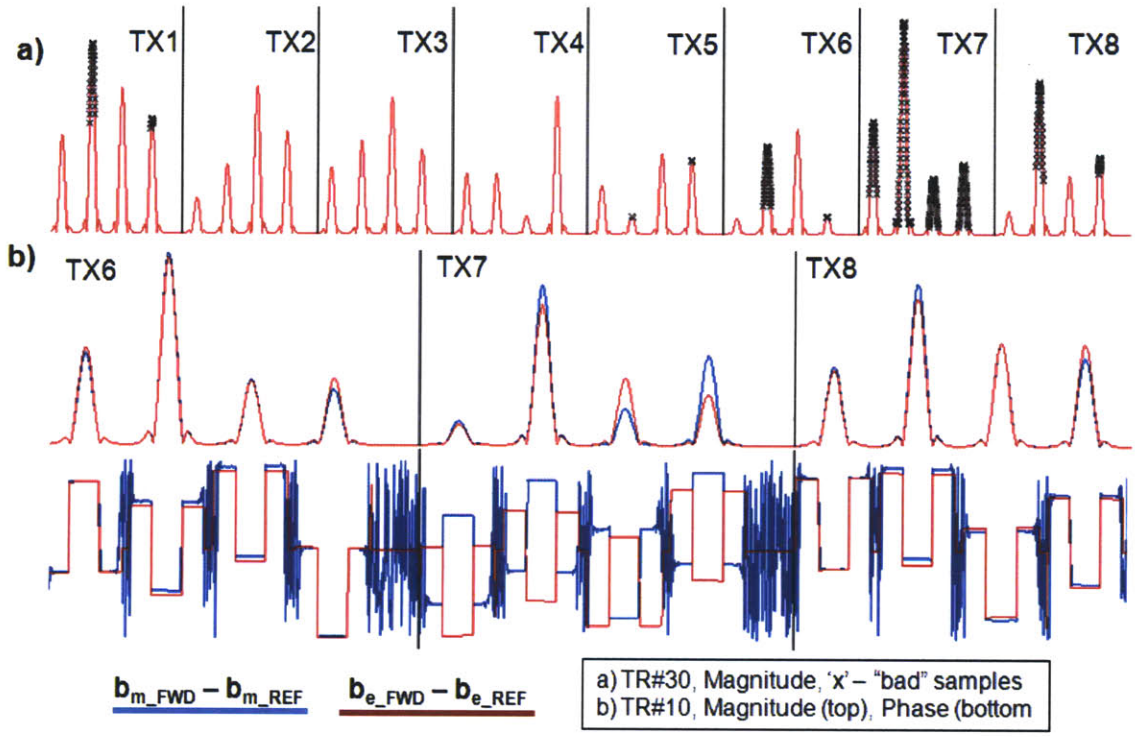

Figure 5-7: Results from RF monitoring of the purposely disturbed acquisition ***pTx3_dstr***, where the phase of TX-channel #7 was purposely altered. a) The black crosses ('x') identify the indexes of the erroneous RF samples, most of which are on the RF waveform played on TX7; b) Magnitude (top) and phase (bottom) overlaid plots of the predicted (red) and measured (blue) RF waveforms, clearly demonstrating the phase jump introduced on TX7.

At last, Figure 5-8 shows the results from the RF monitoring for the excitation 'pTx4_dstr', where the tuning of transmit array's 4th element was purposely changed by purposely placing a small titanium piece in its vicinity. Similarly to the plots shown for

'pTx3_dstr', Figure 5-8a plots black crosses ('x') onto the monitored RF samples which have deviated more than ε_{max} = ±5% from the ideal shapes. Again, not surprisingly, the majority of the crosses are concentrated on the TX-channel that has been disturbed (TX4 in this case). While Figure 5-8b shows that the match between the measured and predicted waveforms is very good for the RF waveforms played on the 6th, 7th and 8th (showing the real part of the signals), even an eye comparison of the waveforms on TX4 reveals noticeable differences. The last raw of Table 3 shows that $\varepsilon_{\%}$ = 12.4%, and that calculated numbers of the derated maximum 10g-avg local SAR have caused $TR_{derated}$ to be ~12 time longer than TR_{used}.

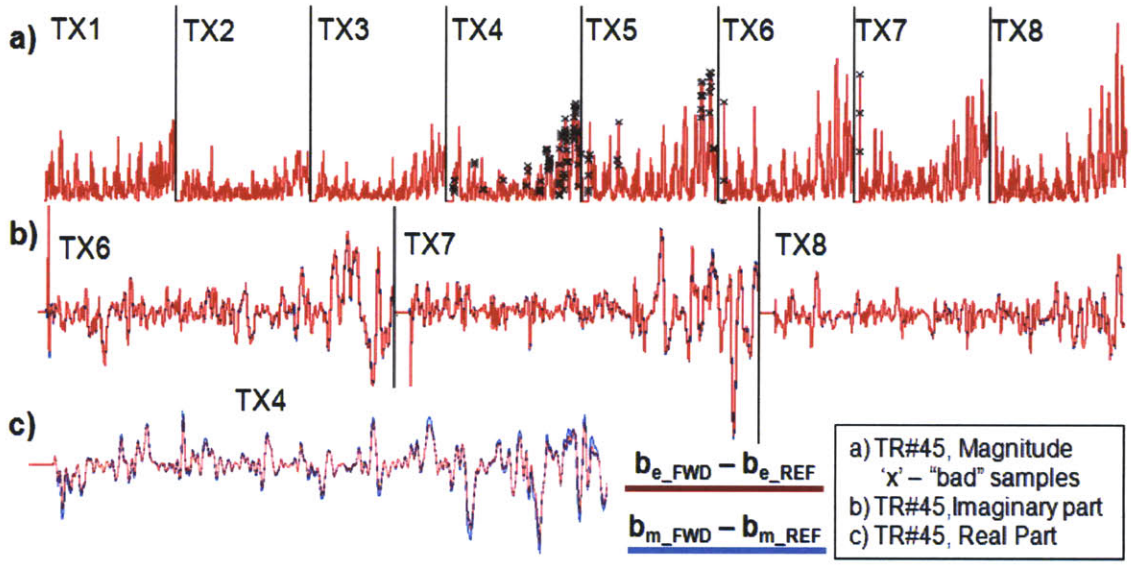

Figure 5-8: Results from RF monitoring of the purposely disturbed acquisition ***pTx4_dstr***, where the tuning of the 4th element of the TX-array was purposely changed by putting a small piece of titanium in its vicinity. a) The black crosses ('x') identify the indexes of the erroneous RF samples, most of which are concentrated around samples of the RF waveform played on TX4; While the match between the predicted (red) and measured signals (blue) on the 6th, 7th and 8th channels is within the limits (b), this is not the case for the waveforms on TX4 (c).

As mentioned previously, the values given in Table 3 are from the one TR with the most erroneous RF samples, i.e. where the length of $\mathbf{v}_{ind\_\varepsilon}$ is largest. Nevertheless, it is instructive to also show the performance of the RF monitoring throughout all the TRs. The value of $TR_{derated}$ is directly depended on the value of $SAR_{10g\_local\_derated}$, which on the other hand scales proportionally to the value of $\varepsilon_{\%}$ (the larger the percentage of the erroneous samples, the larger the value of $SAR_{10g\_local\_derated}$). Therefore, to judge the stability of the RF monitoring system, it would be enough to show the values of $\varepsilon_{\%}$ for all the TRs in a given acquisitions. Figure 5-9 plots the values of $\varepsilon_{\%}$ for all the TRs in the acquisitions of 'pTx2', 'pTx3_dstr' and 'pTx4_dsrt'. The blue/red samples in the graphs

represent the values of $\varepsilon_{\%}$ calculated using the error index vector $\mathbf{v}_{ind\_\varepsilon\_real}/\mathbf{v}_{ind\_\varepsilon\_imag}$, for which the real/imaginary part of the error matrix $\boldsymbol{\varepsilon}(t)$ exceeds the error bar of $\varepsilon_{max} = \pm 5\%$. The black samples on the head, represent the values of of $\varepsilon_{\%}$ calculated using the error index vector $\mathbf{v}_{ind\_\varepsilon}$ (introduced in Section 5.4.1), which takes the non-repeating union of $\mathbf{v}_{ind\_\varepsilon\_real}$ and $\mathbf{v}_{ind\_\varepsilon\_imag}$.

Figure 5-9a and Figure 5-9b shows the great consistency of the RF monitoring system using the proposed threshold criteria for the acquisitions 'pTx2' and 'pTx3_dstr'. As seen in Figure 5-9c, the values of $\varepsilon_{\%}$ for 'pTx4_dsrt' experience a slight fluctuation (±0.5%), which could be a consequence of playing a rapidly changing RF waveform under the given disturbed conditions. In any case, given the small range of fluctuation, we consider this possible and normal. Note that for 'pTx1', $\varepsilon_{\%} = 0\%$ (hence, not shown).

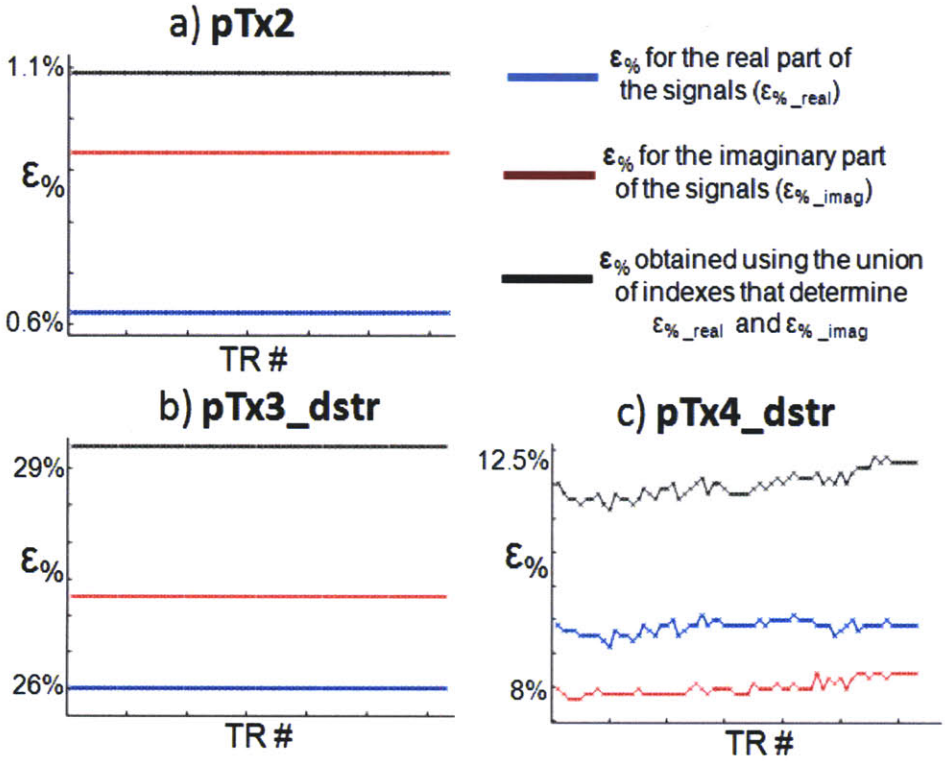

Figure 5-9: The performance of the RF monitoring for a) 'pTx2' b) 'pTx3_dstr' and c) 'pTx4_dstr' throughout the TRs, expressed by the values of $\varepsilon_{\%}$.

5.6 Discussion and conclusions

The work presented in this chapter demonstrates the development of a local SAR monitoring system based on real-time monitoring of RF waveforms using directional couplers that measure the forward and reflect power signals transmitted. The implementation of this RF monitoring system required modifications on both the hardware (Section 5.2) and software end of the pTx system. On the software end, upgrades were performed on the acquisition, and the real-time processing side.

On the acquisition side, the sequence which employs the designed pTx excitation, had to be instructed to record the samples of the RF transmitted – a task that is not needed on any other normal (single-TX) MR acquisition. Secondly, the online image calculation environment had to take the recorded RF samples, do the calculations involved in the threshold algorithm, and stop the acquisition in real time, if needed. While the author of this thesis was heavily involved in the implementation of C++ code needed on the acquisition end, it is important to stress and acknowledge, that the implementation of the developed algorithm in the online calculation environment was done by Siemens engineers involved in the pTx project.

Every new pTx exam session started with the acquisition of a dedicated calibration sequence, with scan time of less than 10s, which estimated the complex-valued 8x8 coupling matrices that transform the transmitted power waveform for each channel set by the digital pulse waveform to the forward or reflected power at each 50Ω matched coil element.

In order to evaluate the intrinsic subject-induced variability in the pTx RF monitoring system, we used 15 subjects with three repeated calibration acquisitions. The calibrated cut-off value (ε_{max} = 5%) was applied in a threshold algorithm, which incorporated worst-case local SAR criteria to derate the applied power based on worst-case local SAR calculations during periods where the waveforms deviated from that expected. Based on the maximum 10g-avg derated local SAR value, a new value of the minimum TR was calculated ($TR_{derated}$), so that the scan would be stopped in real time, if the value of $TR_{derated}$ is bigger than the TR being used in the currently running sequence.

The algorithm was tested for two, most commonly used types of RF pulses (4-spokes and spiral) in disturbed and undistorted conditions. As expected, in the undisturbed acquisitions, the threshold algorithm yielded values for $TR_{derated}$ that did not

trigger acquisition stop. On the other hand, the two disturbed acquisitions (one introduced extra phase in the TX-path of one transmitter, the other changed the tuning of one element of the transmit coil array), caused large error values in the threshold algorithm, yielding values for $TR_{derated}$ that are more than 10 times larger than the minimum TR value. Therefore, in these cases, the acquisitions were rightfully stopped.

Note that this monitoring setup, together with accurate models of local SAR for the given transmit coil and pTx pulse, is critical for reliable and safe *in vivo* acquisitions using parallel transmission. The preliminary results shown in this work demonstrate that the proposed methods can be used to monitor pTx RF waveforms and trigger system shutoff within a 10-ms delay. Future work on larger sample size would be valuable to determine the robustness of the proposed cutoff thresholds.

Chapter 6

7T Parallel Transmit (pTx) Spectroscopic Imaging using Wideband Spokes Excitation and pTx-Optimized CHESS

RF designs for excitation and water suppression using eight independent transmit channels for parallel RF transmission at 7T was used in chemical shift imaging to mitigate excitation inhomogeneity over a 2-cm thick slice selection and a 600 Hz spectral bandwidth. Water suppression preceded the excitation, and was performed with three spectrally-selective RF pulses designed for the 8-channel excitation array. The parallel excitation was demonstrated with a spectroscopy phantom containing physiological concentrations of several major brain metabolites using single-slice, phase-encoded spectroscopic imaging (CSI) acquisitions. The parallel RF excitation was compared with conventional birdcage excitation with equally thick slice selection. For fixed imaging parameters, flip angle and excitation target, the parallel RF excitation outperformed the conventional excitation and provided superior spatial uniformity of the metabolites of interest.

6.1 Introduction

As mentioned in the previous chapters, one of the major challenges in chemical shift imaging (CSI) is the intrinsically low signal-to-noise ratio (SNR) of the metabolites of interest. SNR and chemical shift dispersion are improved at higher field, but at the cost of more severe B_0 and B_1 inhomogeneities [40-42].

Previous attempts to mitigate these excitation field inhomogeneities include the use of adiabatic RF pulses [73-76], RF shimming methods [120-122], or spatially tailored RF excitations [123-124], each of which is associated with tradeoffs. Adiabatic excitation achieves B_1^+ robustness at the cost of high RF power and SAR, and often yields long pulse waveforms which are sensitive to off-resonance effects. RF shimming maintains the short pulse duration of conventional excitation, and is therefore robust for wide spectral bandwidth mitigations, although, some residual excitation inhomogeneity typically remains for large-volume brain excitations at 7T. Spatially-tailored single-channel excitations for mitigation have been demonstrated, but at the cost of significant pulse duration penalty.

As discussed in Section 4.4.1 parallel transmission provides the means to effectively correct for these inhomogeneities. Successful B_1^+ mitigation using pTx excitation at 7T for the purposes of mitigating spatial non-uniformity of the excitation flip angle has been demonstrated with phantom validations as well as *in vivo* for brain excitations by many [104, 109-111, 113]. The *in vivo* studies showed that the proposed "spokes"-based pTx RF design significantly improves the spatial B_1^+ inhomogeneities in the human head compared to conventional birdcage and RF shimming excitation [104]. For CSI related applications however, the RF design needs to provide B_1^+ mitigation over a wider range of off-resonances. As described in Section 4.4.2, [114] proposed an extension to the spokes-based pTx design for slice-selective B_1^+ mitigation (called wideband spokes design) that achieved uniform excitation flip angle for a 5-cm thick slice and 600Hz of spectral bandwidth at 7T. This design incorporated B_0 tracking to improve robustness to spatially-varying main field inhomogeneities, which is important design aspect for band-limited excitation in CSI. This design employed the excitation k-space formalism and is thus limited to the low-flip angle approximation [69].

The goal of the work presented in this chapter is to apply the wideband pTx spokes excitation for B_1^+ mitigation in gradient-recalled-echo (GRE), phase-encoded (PE) CSI

acquisitions using a spectroscopy phantom containing physiological concentrations of the major ^1H brain metabolites, and thus demonstrate the feasibility of these pTx RF pulses for spectroscopic imaging. CHEmical Shift Selective (CHESS) excitation was designed for optimized water suppression with the parallel transmit array via the SLR algorithm [125]. For fixed CSI acquisition parameters, we show that the proposed wideband spokes excitation outperforms conventional birdcage (BC) sinc excitation in terms of B_1^+ mitigation by providing significantly more spatially uniform distributions (75% reduction in spatial inhomogeneities of flip angle) of the major metabolites of interest across the entire in-plane field of view (FOV).

6.2 Methods

All experiments were performed on 7T Siemens Magnetom scanner (Erlangen, Germany) equipped with insert head gradients (80mT/m, 400mT/m/ms) and eight independent transmission channels and power amplifiers used for simultaneous RF excitation (details presented in Section 4.2). Butler matrix transformation of a 16 channel stripline transmit-receive (Tx/Rx) array (shown in Figure 4-1c) was used to drive the 8 brightest orthogonal birdcage (BC) modes for the most efficient usage of the eight available TX channels [101]. The signal was received in a birdcage mode using all of the 16 elements of the Tx/Rx array. All acquisitions were performed on a 17-cm diameter spectroscopy phantom containing physiological concentrations of the following brain metabolites [96]: 12.5 mM N-acytel-L-aspirate (NAA), 10.0 mM Creatine (Cr), 3.0 mM Choline (Cho), 12.5 mM Glutamate (Glu) and 7.5 mM myo-inositol (mI). Magnevist (GdDPTA) was used to shorten the relaxation times of the solution, yielding T_1 = 450 ms.

6.2.1 RF excitation design

The design goal of the excitation was wideband (600 Hz) mitigation of spatial inhomogeneity of B_1^+, with excitation target of the pTx RF pulses defined as the inverse of the measured B_1^+ profile to yield a constant flip angle of ~35^0 degrees across the entire region of interest. Note that the chosen spectral bandwidth of 600Hz is more than enough to properly mitigate the major brain metabolites at 7T ($f_{NAA} - f_{Cho}$ = 1.2ppm at 7T, which is ~356Hz, see Figure 2-1). Non-uniformities due to receive coil sensitivities (B_1^-) are corrected in post-processing based on the measured receive profiles (a by-product

of the B_1^+ estimates, as shown in Section 4.3). Furthermore, by incorporating an estimate of the B_0 field map into the wideband pTx RF design, the algorithm accounts for measured spatial B_0 variations, improving the robustness of the excitation to spatial frequency variations. The B_0 map was estimated following the description given in Section 4.3. However, due to the unavailability of the B_1^+ methods discussed in Section 4.3 at the time when this work was performed, the complex transmit profiles were obtained using a slightly different, more time consuming approach, [104].

In short, two sets of GRE acquisitions were used to estimate the B_1^+ maps. The first set obtained quantitative flip angle maps on the birdcage mode of the Butler matrix mode transformation by acquiring images at six different transmit voltages (10V, 30V, 50V, 70V, 90V and 120V) and fitting a sine curve do the data in each voxel. The second set of acquisitions obtained low flip angle images of each of the other seven transmit modes, used to complete the estimates of all eight B_1^+ maps. Using 3x3 mm^2 in-plane resolution, TR = 2s (with T_1 = 450ms of the facilitated phantom solution, TR is more than $4T_1$, so T_1 weighting is avoided) for the quantitative mapping and TR = 0.5s for the individual modes mapping, the overall time for the mapping was ~17 minutes.

The estimated field maps were then used in the RF pulse design. The spatial-spectral excitation parameters were 2-cm thick axial slab in and 600Hz of spectral bandwidth. A four-spoke excitation k-space trajectory was used, each sinc RF pulse modulated in amplitude and phase on each of the TX channels to mitigate the B_1^+ non-uniformity. Slice selection was obtained by playing z gradient during the sinc sub-pulses. For a magnitude B_1^+ non-uniformity of 2.5-to-1 (maximum-to-minimum), time-bandwidth product of the sinc sub-pulses equal to 2.7, and maximum design gradient strength and slew rate of 30 mT/m and 300 mT/m/ms, the total duration of the RF pulse was 1.75ms. It is important to note that the spectroscopy phantom used was doped enough to roughly match the inhomogeneity of the human head.

For our CSI target excitation, the 1.75 ms-long, four-spoke, slice-selective uniform wideband RF pulse required a peak voltage of 130V (~340W of peak power) to achieve a ~5^0 flip angle. Note that the RF pulse with this peak voltage (power) is played on one TX channel and is the maximum among all the pulses played. As mentioned in Section 4.2), the current hardware constraints on our system limit the maximum transmit voltage on each TX channel to 200V (~800W of maximum power), which consequently limits the excitation to a flip angle of less than 8^0. To increase the flip angle while satisfying the

peak voltage (power) constraint, the VERSE algorithm [126] was applied to the 4-spoke RF pulse to yield a 36^0 flip angle with a penalty of increased pulse duration of 2.71 ms. Figure 6-1a shows a 4-spoke RF pulse and the corresponding gradients that requires 142.5V for 5.73^0 (0.1rad) flip. Keeping the flip angle constant, Figure 6-1b presents its VERSE-ed version, where the VERSE factor of 0.2 lowered the peak RF voltage to ~29V. The new RF duration has been increased to 2.71 ms, which is an acceptable RF length in terms of robustness to B_0 inhomogeneities. Transmitting at 180V (which is ~90% of the imposed hardware limitations of 200V), we were able to achieve a 36^0 excitation flip angle for our experiments.

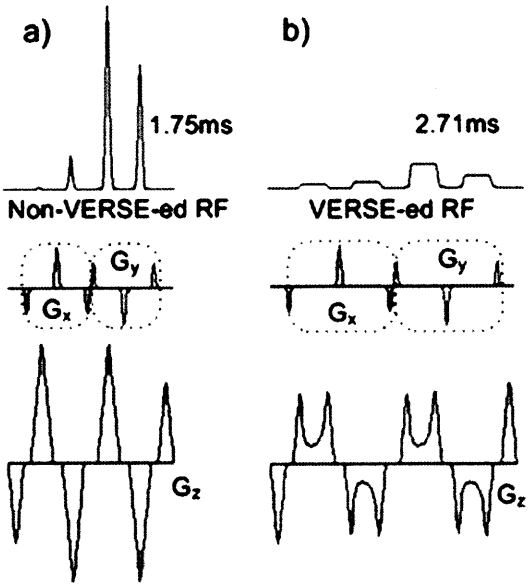

Figure 6-1 a) Four-spoke RF pulse for slice-selective (2cm thick slab) uniform wideband excitation (600 Hz spectral bandwidth). The four sinc sub-pulses (spokes) are placed at chosen (k_x,k_y) in excitation k-space for uniform B_1^+ mitigation. Slice selection is achieved by playing z gradient during the sinc sub-pulses. The RF length is 1.75ms b) Pre-VERSE-ed version of the pulse in a) using a VERSE factor of 0.2. The new RF length is 2.71 ms achieving about ~4 times higher flip angle for a given peak voltage.

6.2.2 Water Suppression Design

A CHESS [31] water suppression with three spectrally-selective RF pulses prior to the excitation was designed for application on the pTx system. The flip angles of these pulses were optimized based on previously estimated composite map, $B_{1,comp}^+$, to minimize the maximum residual M_z across the phantom in the 2-cm thick slice, such that:

$$\theta = \mathbf{min}\left[\mathbf{max}\left(|\mathbf{B_1^+}|\right)/\mathbf{mean}(|\mathbf{B_1^+}|)\right] \quad \textbf{(6-1)}$$

The estimation search of θ was exhaustive, including flip angle ranges between 0^0 and 180^0 with an increment of 2^0. θ is a vector of the flip angle values of N pulses, and $B_{1,comp}^{+}$ is a vector of a composite transmit profile that is to be estimated. Given the $B_{1,ind}^{+}$ profiles of the eight Butler modes and the fact that these pulses are not spatially selective, the composite $B_{1,comp}^{+}$ map used in $\boldsymbol{\theta = \min\left[\max\left(|\mathbf{B_1^+}|\right)/\mathbf{mean}(|\mathbf{B_1^+}|)\right]}$ (6-1), was estimated by finding the set of amplitudes and phases for each of the 8 pulses that minimizes the spatial non-uniformities of $B_{1,comp}^{+}$ with the cost function:

$$(\boldsymbol{\alpha}, \boldsymbol{\varphi}) = \mathbf{min}\left[\mathbf{max}\left(\left|\boldsymbol{B_{1,i}^{+}}\right|\right)/\mathbf{min}\left(\left|\boldsymbol{B_{1,i}^{+}}\right|\right)\right],\ \boldsymbol{i} = [\mathbf{1}, \mathbf{2}, \ldots \mathbf{8}] \qquad \textbf{(6-2)}$$

Here **α** and **φ** are both [1x8] vectors holding the amplitudes and phases of the pulses, respectively, and $B_{1,i}^{+}$ is the transmit profile of the i-th Butler mode. The minimum was selected from an evaluation of $(\boldsymbol{\alpha}, \boldsymbol{\varphi}) = \mathbf{min}\left[\mathbf{max}\left(\left|\boldsymbol{B_{1,i}^{+}}\right|\right)/\mathbf{min}\left(\left|\boldsymbol{B_{1,i}^{+}}\right|\right)\right],\ \boldsymbol{i} = [\mathbf{1}, \mathbf{2}, \ldots \mathbf{8}]$ (6-2) over a range of amplitudes and phases for each channel. The phase range included 8 points equally distributed between 0 and 2π, while the amplitude range included 500 points distributed between 0 and 1.

The θ's in $\boldsymbol{\theta = \min\left[\max\left(|\mathbf{B_1^+}|\right)/\mathbf{mean}(|\mathbf{B_1^+}|)\right]}$ (6-1) express the largest flip angle of the water suppression pulse(s) played on the first, brightest Butler mode (i.e. $B_{1,1}^{+}$) and the flip angles for the rest of the pulses, were simply a scaled version of θ by the relative amplitude amounts given in **α**.

6.2.3 Image acquisitions

In order to demonstrate the feasibility of the 4-spoke wideband mitigation at high SNR, single-slice structural and phase-encoded CSI data was acquired in the absence of water suppression, but with shifts in carrier frequency for the excitation pulse at -300Hz, -150Hz, 0Hz, 100Hz and 250Hz. Images from the CSI were obtained by looking at magnitude of the 1st time sample from each spatial location. All the images were B_1^- corrected, and were acquired using a voxel size of 0.78cc (2cm thick slice and 0.39cc in-plane resolution).

Figure 6-2 shows the pulse sequence diagram on the parallel transmit system. The water suppression module was followed by the pre-VERSE-ed, slice-selective, wideband

uniform 36^0 excitation. The readout section consisted of a single-slice phase-encoded (PE) CSI in a GRE sequence with a TE of 5 ms. The encoded (x,y,f) space was 32 x 32 x 1024 points with 3200Hz spectral bandwidth over a 20-cm in-plane FOV and with a 2-cm thick slice, resulting in a voxel of 0.78 cc. With TR = 1.0 s, the total scan time was ~17 minutes.

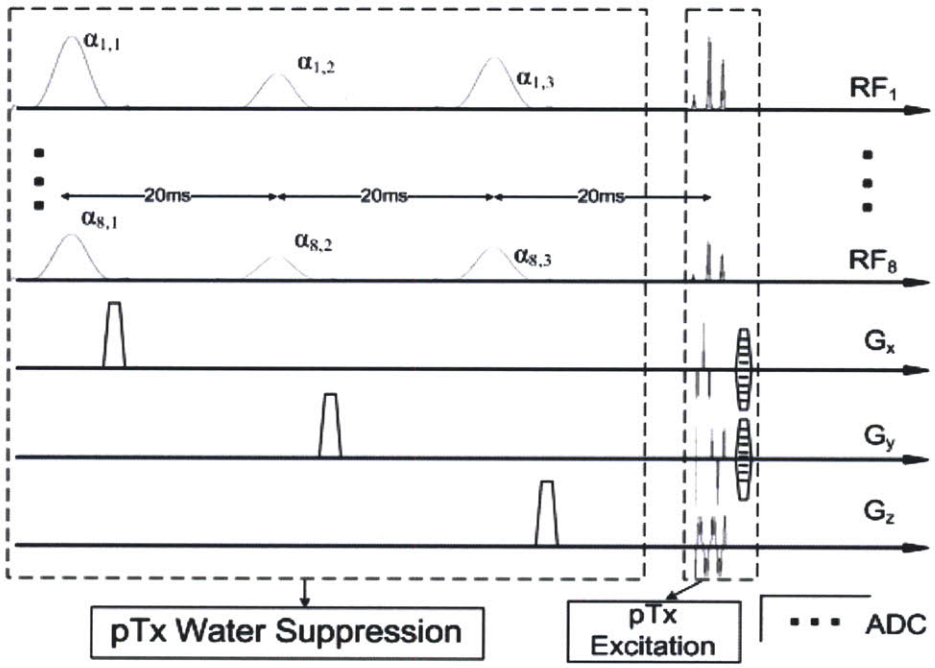

Figure 6-2: The timing diagram for the pTx system. The water suppression consisted of three 12ms long, spectrally selective, minimum phase, Park-McClellan pulses spaced 20ms apart. This was followed by four-spoke slice selective (2-cm thick) wideband (600Hz) uniform RF excitation. Single slice, phase-encoded (PE) CSI readout was appended to this excitation in a GRE sequence with the minimum TE of only 5ms. The readout matrix size was 32x32 encoded over FOV = 20cm for an overall voxel size of 0.78cc. With TR = 1s, the total scan time was ~17mins.

The data from the 16 receive coil elements were combined using a constant phase term for each coil. The resulting combined data set was then corrected for the spatial receive inhomogeneities by division of the previously estimated B_1^- profile. Neither spatial nor spectral apodization was applied. All of the CSI acquisitions were repeated using a BC-sinc excitation, which used a single sinc pulse in a BC mode of the Butler matrix, and served as a comparison case for the pTx four-spoke excitation.

6.3 Results

Figure 6-3 shows the acquired B_0 (Figure 6-3a) and the magnitude and phase of the estimated B_1^+ maps (Figure 6-3b and Figure 6-3c, respectively). The normalized spatial standard deviation of the birdcage mode's B_1^+ (bottom right image in Figure 6-3b) was calculated to be 14.88%, which is comparable to the *in vivo* example presented in [114].

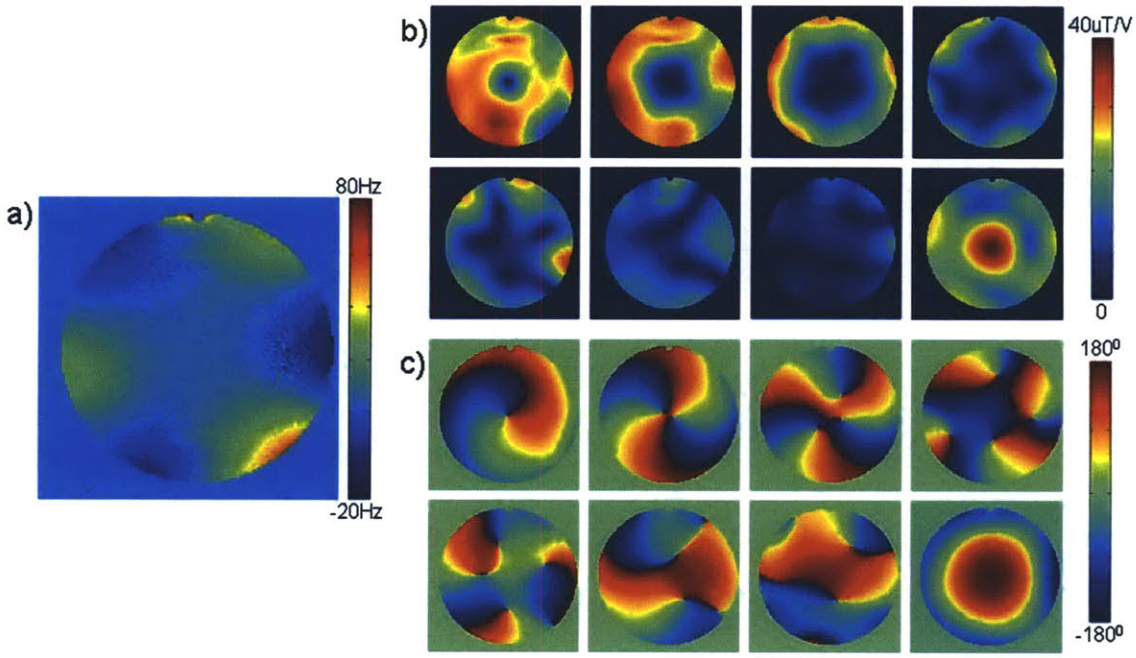

Figure 6-3: Field mapping of the spectroscopic phantom used in all of the experiments; a) Estimate of the B_0 map; b) Magnitude map of the estimated B_1^+ of the eight optimal modes of the Butler matrix transformation; c) Estimated phase maps of the mentioned eight modes.

Figure 6-4a shows the shape and the spectral profile of a 12ms-long, minimum-phase Parks-McClellan (PM) 90^0 RF pulse (designed to excite 300Hz of spectral bandwidth) used in the pTx CHESS design. Figure 6-4b shows a plot simulating the average (circles), and the maximum amount (triangles) of spatial residual M_z left at the time of excitation, for a series of 1, 2, 3 and 4 PM pulses spaced 20ms apart (T_1 used was 450ms) using the optimization described in $\boldsymbol{\theta = \mathbf{min}\,[\mathbf{max}\,(|\mathbf{B_1^+}|)/\mathbf{mean}(|\mathbf{B_1^+}|)]}$ (6-1) and $\boldsymbol{(\alpha, \varphi) = \mathbf{min}\big[\mathbf{max}\,(|B_{1,i}^+|)/\mathbf{min}(|B_{1,i}^+|)\big],\ i = [1, 2, \ldots 8]}$ (6-2). Note that the performance after N > 2 doesn't significantly lower the amount of residual M_z. For the purposes of our experiments, we chose N = 3, where the set of flip angles was [87^0, 57^0, 144^0] with average and maximum residual M_z value of 4.29% and 8.58%, respectively. Figure 6-4c compares the performance of the

pTx-CHESS variant proposed, and the conventional birdcage CHESS by comparing the simulated residual M_z across the phantom after playing the set of 3 pulses 20ms apart. The top image is residual M_z of the conventional CHESS played only on the birdcage Butler mode, while the bottom image represents the residual M_z of the pTx-CHESS using the $B^+_{1,comp}$ obtained from a linear combination of the individual, $B^+_{1,i}$, profiles using α and θ from $(\boldsymbol{\alpha}, \boldsymbol{\varphi}) = \mathbf{min}\left[\mathbf{max}\left(\left|\boldsymbol{B}^+_{\mathbf{1},i}\right|\right)/\mathbf{min}\left(\left|\boldsymbol{B}^+_{\mathbf{1},i}\right|\right)\right],\ \boldsymbol{i} = [\mathbf{1}, \mathbf{2}, \ldots \mathbf{8}]$ (6-2). Compared to the average and maximum M_z values reported above (4.29% and 8.58%, respectively), the pTx-CHESS variant outperformed the conventional CHESS (average and maximum M_z values of 9.71% and 16.29%, respectively).

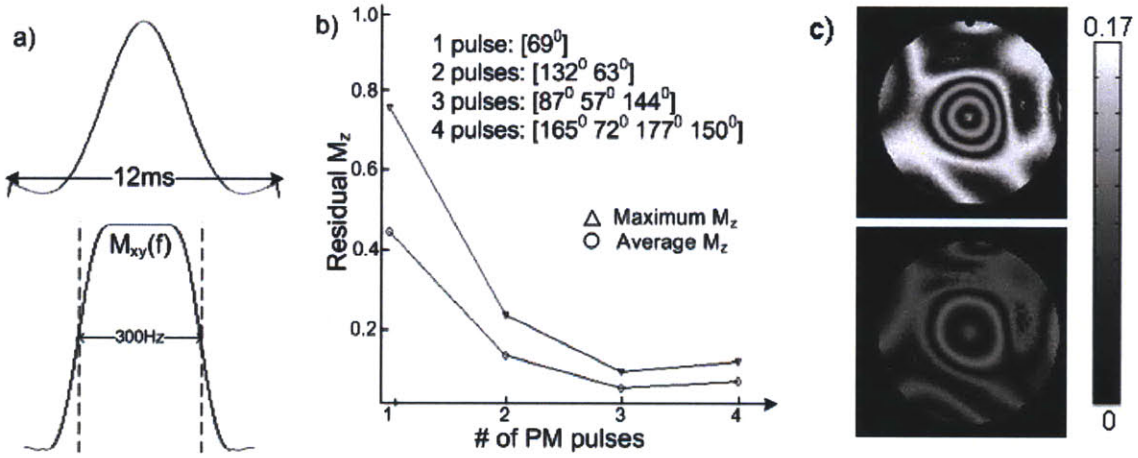

Figure 6-4: a) The 12ms Parks-McClellan (PM) shaped pulse used in the water suppression module (top) and the simulated M_{xy} component as a function of frequency (bottom) for a 90^0 flip. b) The average (circles) and the maximum (triangles) residual longitudinal (M_z) component after simulating 1, 2, 3 and 4 PM pulses (for N > 2, the spacing between pulses is 20ms). The flip angles found for each of the runs are shown. c) Residual M_z as a function of space obtained by conventional CHESS using the B_1^+ of the birdcage mode (top) and the pTx CHESS using the composite B_1^+ map calculated according to $(\boldsymbol{\alpha}, \boldsymbol{\varphi}) = \mathbf{min}\left[\mathbf{max}\left(\left|\boldsymbol{B}^+_{\mathbf{1},i}\right|\right)/\mathbf{min}\left(\left|\boldsymbol{B}^+_{\mathbf{1},i}\right|\right)\right],\ \boldsymbol{i} = [\mathbf{1}, \mathbf{2}, \ldots \mathbf{8}]$ (6-2) (bottom). M_0 was assumed to be 1, both images are on the same scale of 0.17. pTx CHESS outperforms the conventional CHESS when comparing the average and maximum residual M_z (4.29% and 8.58% for the pTx CHESS and 9.71% and 16.29% of the conventional CHESS).

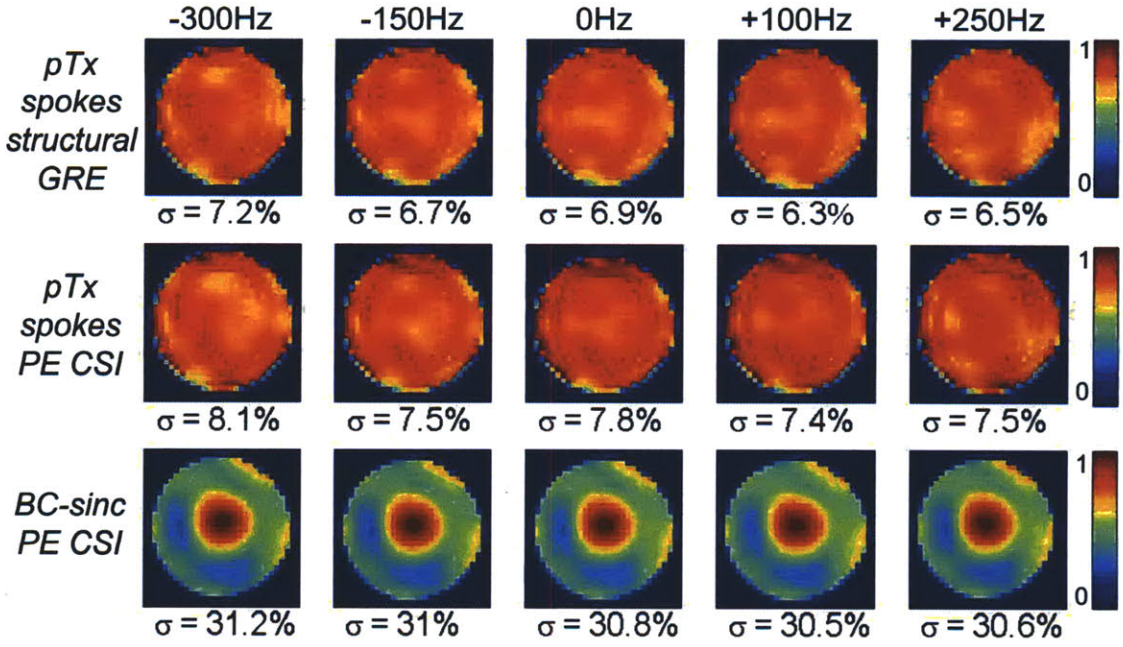

Figure 6-5: Images from single slice phase encoded CSI acquisitions with unsuppressed water using: the 4-spoke uniform wideband (second row), BC-sinc (third row) excitations at -300, -150, 0, 100 and 250 Hz. Images are obtained by looking at absolute value of the first time sample. After dividing out the (receive) B_1^- profile, the 4-spokes design shows successful B_1^+ mitigation in space and frequency, clearly superior to the BC-sinc excitation. The first row shows images from a structural GRE 2DFT using the spokes-based pulse (at the same off-resonances), which are expectedly equivalent to the ones in the second row. The values of sigma (σ) are the normalized standard deviations for each image, and represent a metric of the spatial uniformity. All image intensities are mapped to the same colorbar.

The bottom two rows of **Error! Reference source not found.** show images at 5 different frequencies from PE CSI acquisitions in the absence of water suppression using the spokes-based (second row) and BC-sinc (third row) excitation. These data demonstrate excellent fidelity of the pTx wideband spoke pulse compared to the BC mode. The first row in **Error! Reference source not found.** shows images from structural GRE 2DFT acquisition using the pTx 4-spoke pulse, obtained at the same imaging resolution as the CSI scans. The values of sigma (σ) below each of the images represent the normalized standard deviations of the magnitude of the signal intensity across the FOV, and are reported as a metric of the spatial uniformity of the flip angle. As expected, the first and second rows yield equivalent results.

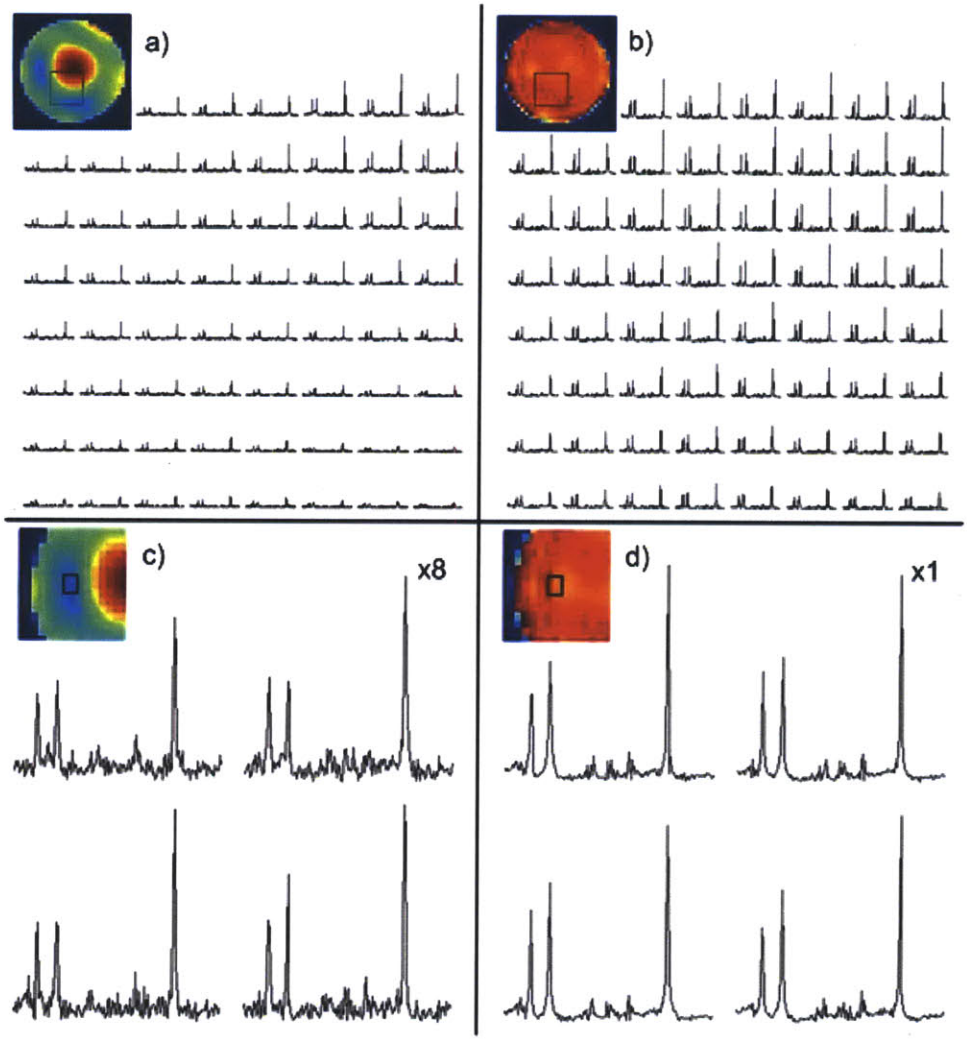

Figure 6-6: Magnitude spectra acquired using phased-encoded CSI readout (TR=1s, TE = 5ms, voxel size = 0.78cc) from particular spatial locations of the spectroscopy phantom containing physiological concentrations of the major brain metabolites. Spectra from the spokes-based design shown in b) demonstrate spatially uniform excitation compared to the sinc BC excitation shown in a). The most dramatic benefit is shown on the bottom two images where the glutamate signals are easily detectable for the spokes-based excitation as shown in d) but are at the noise level for the BC sinc excitation as shown in c). Note that the amplitude in panel c) is scaled up by factor of 8 relative to panel d).

Figure 6-6 shows B_1^+- and B_1^--corrected water suppressed CSI acquisitions using the BC-sinc (Figure 6-6a and Figure 6-6c) and the 4-spoke excitation schemes (Figure 6-6b and Figure 6-6d). A baseline correction was applied in post processing (VB15 Siemens Spectroscopy Toolbox®) and all spectra are displayed over the 1.5 ppm to 3.5 ppm (~600Hz) range. The BC sinc-RF spatial signal dropout due to excitation RF inhomogeneity is clearly demonstrated (Figure 6-6a), as is the excellent mitigation by to the wideband spokes design (Figure 6-6b). The most dramatic benefit is shown on the bottom two images that focus on the region with the most severe B_1^+ inhomogeneity, and

in this case the glutamate signals are easily detectable for the spokes-based excitation (Figure 6-6d), while they are at noise level for the BC sinc excitation (Figure 6-6c).

6.4 Discussion and Conclusions

These results demonstrate successful wideband B_1^+ mitigation in 7T CSI with parallel transmission for a 2-cm thick axial slab over a 600Hz spectral bandwidth. The methods were applied in a spectroscopy phantom containing physiological concentrations of the major ^1H brain metabolites. The 4-spoke design yields greatly improved spatial-spectral uniformity of excitation flip angle across the entire excited slice, and performs significantly better than the standard BC-sinc excitation. B_1 shimming comparison was not performed, since Setsompop et al [104] show that while the B1 shimming slightly improves the spatial uniformity over the birdcage excitation (normalized spatial standard deviation of 14.8% and 12.2%, respectively), the proposed spokes-based design is clearly superior (normalized spatial standard deviation of 6.5%). Furthermore, the associate water suppression was achieved by 3-spectrally-selective pulses in a RF-shim, pTx-optimized version of CHESS for 8 channels.

The results presented show the feasibility of the proposed methods for phantom scanning. However, there still are several issues that need to be addressed prior to *in vivo* imaging. These include larger flip angles, suppression of subcutaneous lipid signals, and online monitoring of specific absorption rate (SAR).

Each of the RF power amplifiers used in our pTx system can physically deliver no more than ~800 W of power, which yields an upper limit voltage of ~200V for RF excitation per channel. Overcoming this constraint would not only facilitate 90^0 pTx wideband excitation designs, but also permit the development of 180^0 refocusing pulse, needed for CSI spin-echo acquisitions. Larger flip angles also offer possibilities for alternate water suppression schemes to employ spokes-based spectral-spatial pulse for more spatially uniform water suppression. Other developments are also enabled by larger flip angles, including an extension of the standard (single-TX-channel) spectral-spatial RF design [127] to pTx RF design, in a way that the sinc sub-pulses of the spectral-spatial RF pulse can be replaced with the spokes-based RF shapes that would mitigate the spatial B_1^+ inhomogeneity.

Estimation of metabolite signals, particularly near the skull, are significantly contaminated by strong lipid bleed due to point-spread function issues. Recently, Avdievich et al [128], proposed lipid suppression methods for a pTx system, by playing pre-saturation pulses on the first gradient mode of a Butler matrix transformation which has an excitation pattern in a shape of a ring, approximating the shape of the head (i.e. the skull). These methods can be combined with the current excitation scheme to enable for in vivo imaging with lipid suppression. Alternate lipid suppression methods include "inner-volume" excitation [129] with parallel transmission to selectively excite brain only, but exclude skull and subcutaneous tissue. Yet another candidate for lipid suppression is spectral suppression, by extending the current pulse design to improve the spectral profile of the RF target excitation, i.e. adding a stop-band over the frequencies of strong lipid signals In addition, one could design for a stop band over 100Hz of spectral bandwidth around 4.7ppm, in order to suppress the water, and therefore exclude any water suppression module. These and related ideas are currently active areas of research.

Finally, it's worth noting that phase-encoded readout schemes prohibit *in vivo* volumetric CSI acquisitions beyond low-resolution single-slice acquisitions due to time constraints. This can be addressed with more efficient CSI readout schemes, such as the spiral CSI algorithm [67] described in **Error! Reference source not found.**, which offers two orders of magnitude decrease in acquisition times. Employment of the spiral CSI package to pTx spectral-spatial designs that simultaneously suppress both the water and lipid signals is presented in the chapter that follows.

Chapter 7

Two-shot Spectral-Spatial 7T Parallel Transmit Spectroscopic Imaging using Spiral Trajectories

Spectral-spatial RF designs using eight independent transmit channels for parallel RF transmission at 7T was used in chemical shift imaging to simultaneously mitigate B_1^+ inhomogeneities over a 2.5-cm thick slab selection and a 450Hz spectral bandwidth, and suppress the water and lipid resonances. The desired 4-dimensional excitation profile was achieved by playing two spectral-spatial (SS) RF pulses in adjacent TR periods, each with full metabolite SNR, followed by a phased combination of the complex-valued data from each excitation. The performance of the design was demonstrated with a spectroscopy phantom containing physiological concentrations of several major brain metabolites and three-dimensional chemical shift imaging (CSI) acquisitions using spiral k-space trajectories to speed up the acquisition times. The parallel (SS) RF excitation was compared with equivalent birdcage excitation having identical spectral bandwidth and slab thickness. For fixed imaging parameters, maximum flip angle and excitation target, the parallel RF excitation outperformed the birdcage excitation by providing ~3.5 times more uniform spatial profile of the metabolites of interest (measured by the normalized spatial standard deviations), while achieving the same signal suppression over undesired water and lipid frequencies.

7.1 Introduction

The work presented in this chapter follows up on the methods described in Chapter 6, in order to further improve the spectral-spatial excitation patterns for pTx CSI applications. As already mentioned, in addition to wideband spectral mitigation, spectroscopic imaging also requires suppression of the strong water and lipid signals, which are the main contamination sources of the metabolites' signals.

The performance of conventional water suppression preparation modules, such as Chemical Shift Selective Imaging, or Water Suppression enhanced through T1 effects [32] (WET), performance is limited at high field strengths due to the inability to reach uniform flip angle across the volume of interest. Section 6.2.2 proposed a pTx-CHESS RF pulse design, which outperformed the conventional birdcage-CHESS scheme.

Lipid suppression preparation modules usually take the form of spectrally- [72], or not spectrally-selective [75, 130] adiabatic pulses, that are played before the excitation and are timed such that the longitudinal component of the lipid is as small as possible. Moreover, spectral-spatial RF excitation schemes [90-93] provide simultaneous selectivity in frequency and one spatial dimension, by playing a train of spatially selective pulses modulated by a time envelope which produces the spectral selectivity. While they can yield excellent water suppression, nulling of the lipid signals is mostly limited by the frequency dispersion (i.e. the field strength) between the NAA and the lipid signals.

The goal of the current work is to further extend the wideband pTx spokes excitation [114] into a spectral-spatial RF design that in addition to the spatial B_1^+ mitigation, it will also incorporate spectral selectivity for simultaneous water and lipid suppression. The feasibility of the proposed excitation for 7T pTx spectroscopic imaging is demonstrated in a 3D volumetric gradient-recalled-echo (GRE), spiral CSI [67] acquisitions using spectroscopy phantom containing physiological concentrations of the brain metabolites. For fixed CSI acquisition parameters, we show that the proposed spectral-spatial wideband spokes excitation outperforms the conventional spectral-spatial birdcage-sinc (BC) excitation by providing more spatially uniform distributions of the major metabolites of interest across the entire in-plane field of view (FOV).

7.2 Methods

All experiments were performed on 7T Siemens Magnetom scanner (Erlangen, Germany) equipped with head insert gradients (80mT/m, 400mT/m/ms) and eight independent transmission channels and power amplifiers used for simultaneous RF excitation. The feasibility of the proposed excitation was shown on a 17-cm diameter spectroscopy phantom containing physiological concentrations of the following brain metabolites [96]: 12.5 mM N-acytel-L-aspirate (NAA), 10.0 mM Creatine (Cr), 3.0 mM Choline (Cho), 12.5 mM Glutamate (Glu) and 7.5 mM myo-inositol (mI). Magnevist (GdDPTA) was used to shorten the relaxation times of the solution, yielding T_1 = 450 ms.

7.2.1 RF pulse design

The design goal of the excitation was to simultaneously achieve: 1. Wideband mitigation of spatial inhomogeneity of B_1^+, with excitation target of the pTx RF pulses defined as the inverse of the measured B_1^+ profile, and 2. Spectral selectivity in order to suppress water and lipid resonances. The RF design algorithm required estimation of B_1^+, B_1^- and B_0 maps for every experimental run based on a single-slice (1-cm thick) measurement. The acquisition time for the B_1^+, B_1^- and B_0 maps was about 2 minutes, and followed the methods described in Section 4.3.

The first step of the RF design was creating the wideband spatial mitigation. The excitation parameters were 2.5-cm thick slab in z and 450Hz of spectral bandwidth, enough to mitigate the major metabolites of interest at 7T. A four-spoke excitation k-space trajectory was used, each sinc RF pulse modulated in amplitude and phase on each of the TX channels to mitigate the B_1^+ non-uniformity. Non-uniformities due to the B_1^- patterns were corrected in post-processing, with the previously measured receive profiles. The estimated B_0 field map was incorporated in the design algorithm to account for B_0 variations. Slice selection was obtained by playing z gradient during the sinc sub-pulses. For a magnitude B_1^+ non-uniformity of 2.5-to-1 (maximum-to-minimum), time-bandwidth product (TBP) of the sinc sub-pulses equal to 3, and maximum design gradient strength and slew rate of 25 mT/m and 200 mT/m/ms, the total duration of the RF pulse was 1.05ms. However, this pulse required a peak voltage of 160 V to achieve a 5^0 flip angle. Current hardware constraints on our system limit the maximum transmit voltage to 200 V, so in order to increase the flip angle while satisfying the peak voltage

constraint, the VERSE algorithm [126] was applied to the 4-spoke RF pulse to yield a ~14^0 flip angle (for 190V of transmit voltage) with a penalty of increased pulse duration of $\tau_{4spokes}$ = 1.44 ms. Figure 7-1a shows the VERSE-ed 4-spoke RF pulse and the corresponding gradients.

The second step in the RF design dealt with the spectral selectivity of the overall excitation. As mentioned previously, spectral-spatial RF pulses are created by a train of spatially selective RF pulses, modulated by a time envelope which forms the spectral selectivity [93]. The extend and the sharpness of the spectral profile is determined by the number of samples and the sampling period of the time envelope, Δt, which in the same time is also the duration of the spatially selective sub-pulse. For 7T CSI, the frequency bandwidth between the choline and the NAA peak is about 360Hz, the water signal is ~620Hz away from the middle of the choline and NAA peak, and the closest lipid signal to the NAA is ~210Hz away. If the metabolite signals were to be in the passband, and the water and lipid signal in the stop band of the spectral window, then $\Delta t < 0.9$ms (for total pulse duration < 30ms and TBWP ≈ 15). Given this constraint and the fact that $\tau_{4spokes}$ = 1.44ms > Δt, an extension of the wideband 4-spokes pulse to the desired spectral-spatial pulse is not straightforward.

In order to meet the Δt constraint, one must divide the spectral-spatial design into two-shot excitation. Separation of excitation k-space into two averages (which are later summed) was shown by [131] in order to reach extra short TE. In that work, half-sinc RF pulses excited two halves of excitation k-space in two separate averages. This type of idea can be applied to the current spectral-spatial design by subsampling the spatial or spectral dimension of the overall excitation k-space. Spatial dimension subsampling means that the wideband 4-spoke pulse is separated into two 2-spoke pulses such that $\tau_{2spokes} = \tau_{4spokes}/2 < \Delta t$, and a straightforward spectral-spatial design is possible. Therefore, the uniform B_1^+ mitigation is produced after summation of the two, spatially non-uniform mitigations from two separate averages. However, the main problem of this approach for spectroscopic imaging is that it is not SNR optimal, *since a two-average acquisition will not produce √2 gain in the signal.* Therefore, this approach was not pursued.

Alternatively, subsampling of the spectral dimension involves modulating a train of the 1.44ms long 4-spoke wideband pulse with different (the even and the odd) subsamples of a time envelope that satisfies the desired spectral bandwidth

requirements. The samples marked with circles (o) and crosses (x) in Figure 7-1b are 1.44/2 = 0.72ms apart and yield excitation with spectral profile that puts the metabolite peaks in its passband, and the water and lipid signals in its stopband for 7T CSI. Hence, the sampling between two o/x samples is 1.44ms, enough to fit the full 4-spokes wideband pulse. Therefore, the spectral-spatial pulse played in the first/second average, is obtained by modulating the train of the wideband 4-spokes subpulse with the o/x samples (Figure 7-1c and Figure 7-1d, respectively). The time envelope shown in Figure 7-1b, has 18 o/x samples, so the total duration of each of the spectral-spatial pulses given in Figure 7-1c and Figure 7-1d was measured to be 18·1.44ms = 25.92ms. In addition, compared to the flip angle of one sublobe (Figure 7-1a), now the overall flip angle has been increased ~2.3 times (due to the modulated repetition of the 4-spoke pulse), yielding a flip angle of ~31^0 for a transmit voltage of 190V.

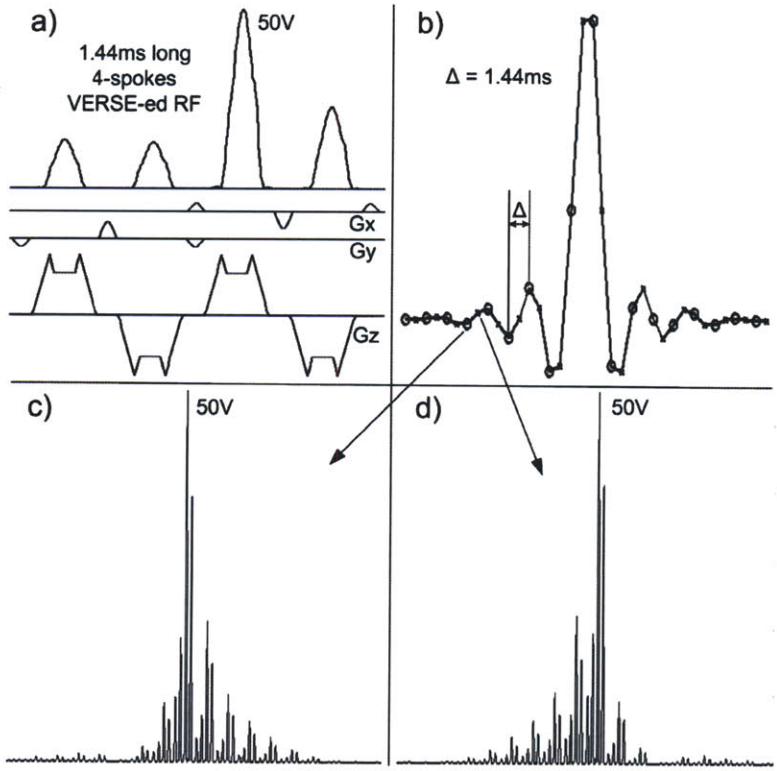

Figure 7-1: a) Example of a four-spoke RF pulse for slice-selective (4cm thick slab) uniform wideband excitation (450 Hz spectral bandwidth) accompanied with the corresponding gradients. The four sinc sub-pulses (spokes) are placed at chosen (kx,ky) in excitation k-space for uniform B1+ mitigation. Slice selection is achieved by playing z gradient during the sinc sub-pulses. All the spokes were VERSE-ed in order to reach higher flip angle, yielding a total RF duration of 1.44ms. b) The shape of the time envelope used to modulate a train of the four-spoke pulse (shown in a)) in order to achieve the spectral selectivity. c) The spectral-spatial pulse composed by the cross-product of the samples marked with circles ('o') on the time envelope shown in b), which is played in the first average. d) The spectral-spatial pulse composed by the cross-product of the samples marked with crosses ('x') on the time envelope shown in b), which is played in the second average. Having 18 circles/crosses samples in the time envelope, the overall time duration of the spectral-spatial RF pulses shown in c) and d) was 18·1.44ms = 25.92ms;

Due to the undersampling that was done on the time envelope, each of the pulses shown in Figure 7-1c and Figure 7-1d has the first spectral sideband (sidelobe) over the water and lipid frequencies, which is off course undesirable. However, the two RF pulses *together* sample all of the desired spectral-spatial excitation k-space, and if properly phased and summed, the desired spectral selectivity (i.e. suppressing the water and the lipids, and mitigating the metabolites) can be reached.

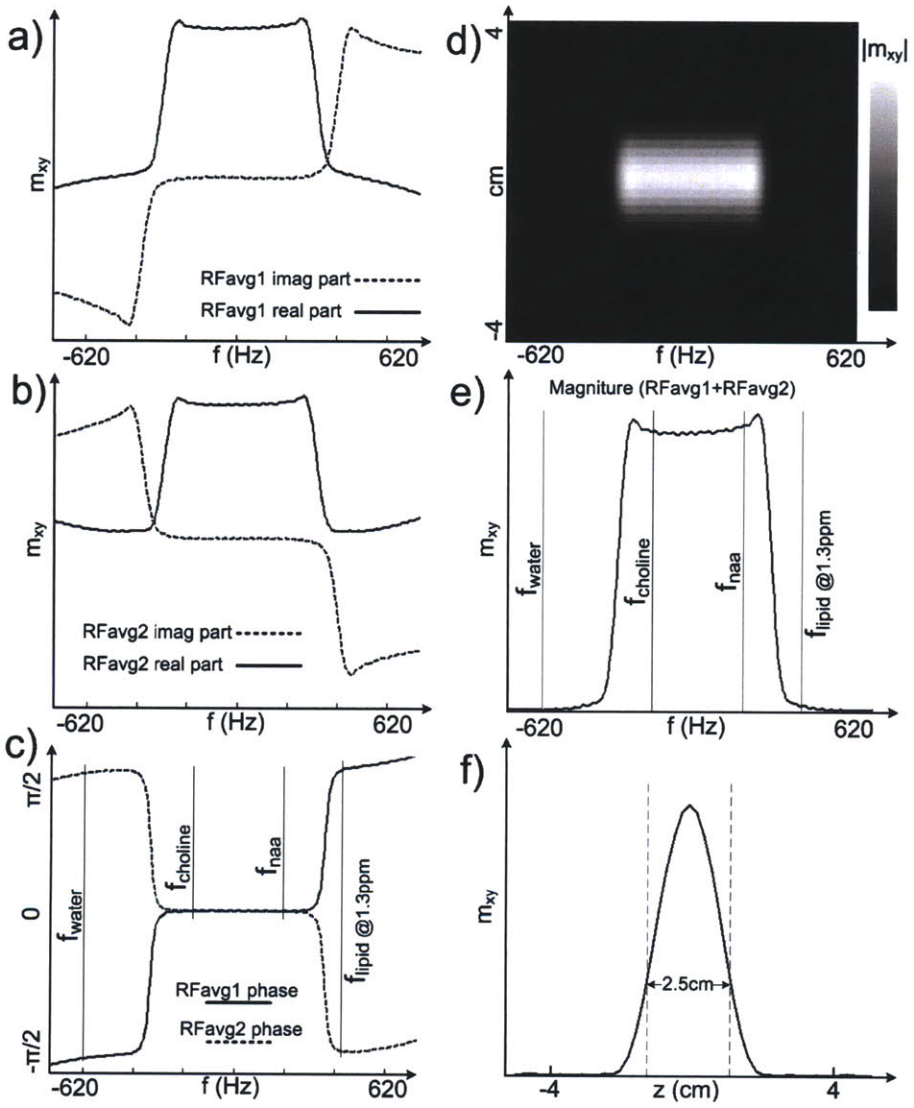

Figure 7-2: Bloch simulations of the one spatial voxel (x = 14, y = 11) capturing frequency bandwidth of ±700Hz. The real (solid lines) and imaginary (dashed lines) part of the simulated frequency profile of the spectral-spatial excitation from the first and second average is given in *a)* and *b)*, respectively; *c)* Each of the spectral profiles is phased with different linear and constant terms such that there is zero phase in their passband. Making the phase in the passpand to have no slope consequently makes the phase around water and lipid frequencies to have the opposite sign; *d)* The simulated spectral-spatial (f-z) profile across ±4cm and ±700Hz. *e)* Summation of the two, properly phased excitations over the middle 1cm thick slice (-0.5cm< z <0.5cm) gives the desired frequency profile, where the water and lipid frequencies are suppressed, and the NAA, creatine and choline resonances are properly mitigated. *f)* The slice selective profile shown over ±4cm for the center spectral frequencies.

Figure 7-2 shows Bloch simulations of one spatial location (x = 14, y = 11, z = 0) capturing off-resonances spanning ±700Hz. Inputs to these simulations (and to all the others shown later) were the eight estimated B_1^+ maps, the estimated B_0 map and the two designed sets of eight spectral-spatial RF pulses. The B_0 for this particular voxel was estimated to be -10.48Hz (measured relative to the main water peak). The real and imaginary parts (solid and dashed lines) of the simulated frequency profile from the first and second average is given in Figure 7-2a and Figure 7-2b, respectively. Each of these profiles has been properly phased with different constant and linear phase terms such that there is no phase (zero radians) in their passband, as shown in Figure 7-2c. Specifically, phase terms in the form of $\exp(2\pi \cdot i \cdot \varphi_{lin\_1} \cdot f - i \cdot \varphi_{const\_1})$ and $\exp(2\pi \cdot i \cdot \varphi_{lin\_2} \cdot f - i \cdot \varphi_{const\_2})$ have been applied to the first and second average excitation, respectively. The linear phase terms (φ_{lin_1} and φ_{lin_2}) have been optimized separately for the two RF pulses such that the slope of each of the excitation phase is zero. The constant phase terms (φ_{const_1} and φ_{const_2}) simply bring the phase of the passband frequencies to zero radians. Note that, if properly optimized, φ_{lin_1} and φ_{lin_2} make the two frequency profiles to be completely out of phase around the water and lipid frequencies, while in the same time being completely in-phase for the metabolites' frequencies (as seen in Figure 7-2c).

Figure 7-2d shows the simulated 2D spectral-spatial (f-z) space after summation of the two, properly phased excitations and extending the Bloch simulations over a range of values along the z axis (±4cm). Looking at the combined spectral profile for a 1-cm thick slice (-0.5cm < z < 0.5cm), one can see that the water and lipid frequencies are suppressed, and the NAA, creatine and choline ones are properly mitigated (Figure 7-2e). An insightful observation here is that $\varphi_{lin\_2} \approx \varphi_{lin\_1} + \tau_{4spokes}/2$. Note that φ_{lin_2} would exactly equal $\varphi_{lin\_1} + \tau_{4spokes}/2$ in the unrealistic case when there are no B_0 drifts, i.e. $B_0(x,y) = [\mathbf{0}]$Hz. Hence, we can say that $\varphi_{lin\_2} = \varphi_{lin\_1} + \tau_{4spokes}/2 + \Delta\varphi_{B0}$, where $\Delta\varphi_{B0}$ is an extra phase term that is directly dependent on the estimated B_0 map. At last, Figure 7-2f shows the slice profile of the overall excitation for the middle frequency of the spectral passband.

Figure 7-3 shows Bloch simulations of the in-plane spatial profiles for a 1-cm thick slice (-0.5cm < z < 0.5cm) and four different off-resonances: -620Hz (residual water), -180Hz (choline), 180Hz (NAA) and 390Hz (the lipid resonance at 1.3ppm). The performance of the 2-shot spectral-spatial 4-spoke design was compared against two alternatives: 2-shot spectral-spatial birdcage (BC) and 2-shot spectral-spatial RF-

shimming designs. In both of these two cases, a train of 1-spoke (i.e. *single* sinc waveform) subpulses were modulated by the same time envelope shown in Figure 7-1b (the length of the 1-spoke subpulse was extended to $\tau_{4spokes}$ = 1.44ms). The values of sigma (σ) shown are the normalized standard deviations for each image, and represent a metric of the spatial uniformity. Comparison of the passband images from **Error! Reference source not found.**a and Figure 7-3b to those from Figure 7-3c, alludes to successful spatial B_1^+ mitigation of the 4-spokes spectral-spatial excitation across all of the metabolites' frequencies, clearly superior to the BC and RF shimming spectral-spatial excitations. In the same time, all of the three excitations suppress more than 99% of the water, and more than 95% of the lipid resonances. Finally, Figure 7-3d shows the phase maps of the 2-shot spectral-spatial 4-spoke excitation, which don't change over the passband frequencies.

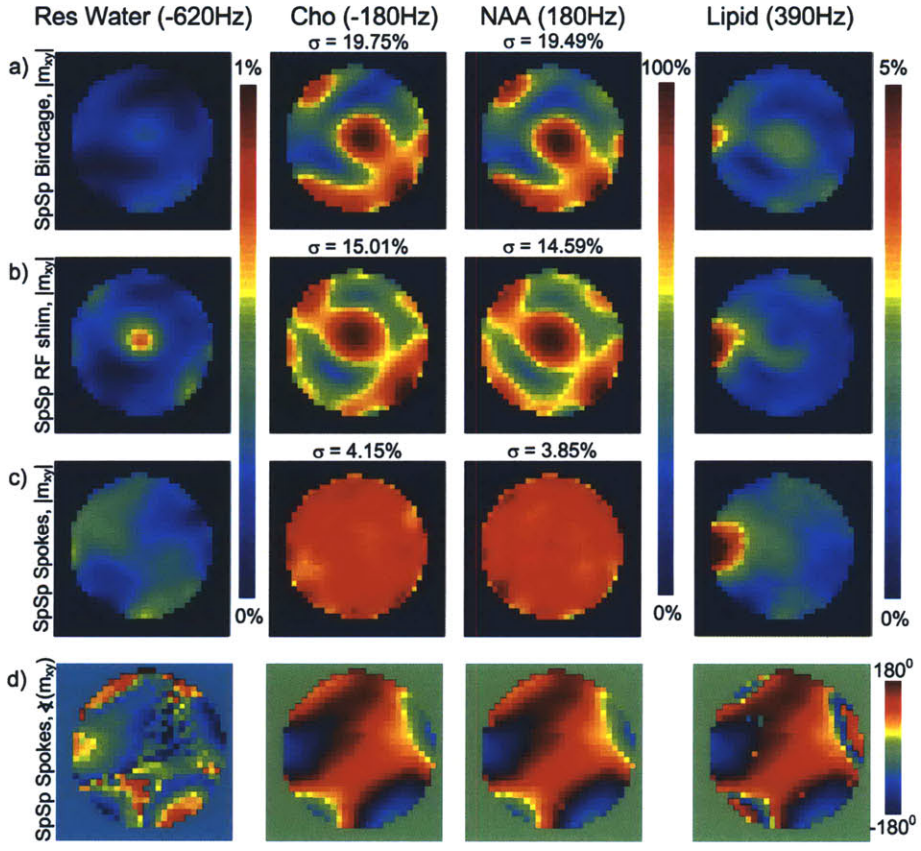

Figure 7-3: Bloch simulations of the spatial excitation profiles for four different off-resonances: -620Hz (residual water), -180Hz (choline), 180Hz (NAA) and 390Hz (lipid signal at 1.3ppm). Magnitude images of the transversal magnetization for: *a)* 2-shot spectral-spatial birdcage excitation; *b)* 2-shot spectral-spatial RF shimming excitation; *c)* 2-shot spectral-spatial 4-spokes excitation. While all of the excitations suppress more than 99% of the water signals and more than 95% of the lipid resonances, the 2-shot spectral-spatial 4-spokes design shows successful spatial B_1^+ mitigation over the spectral passband, clearly superior to the BC-sinc and RF shimming equivalents. The values of sigma (σ) are the normalized standard deviations for each image, and represent a metric of the spatial uniformity. *d)* Phase maps of the 4-spokes spectral-spatial

2-shot excitation, which don't change over the passband frequencies, and are related to the estimate of the B_0 map.

7.2.2 Data Acquisitions

All the data was acquired using a 2-average, gradient recalled echo (GRE) spectroscopic imaging sequence. Figure 7-4 shows the pulse sequence diagram on the parallel transmit system. The spectral-spatial RF pulse design was followed by time-efficient 3D volumetric CSI readout using constant density spiral k-space trajectories [67]. The 4D spectral-spatial (x,y,z,f) space included 26x26x12x640 points (zero-padded to 32x32x16x1024) encoded over FOV_{XY}=20cm and FOV_Z=12cm, resulting in an overall voxel size of 0.59cc. The spectral readout bandwidth was 2000Hz, and the acquisition window was 320ms long (hence the 640 frequency points). The maximum gradient strength and slew limit for the spiral trajectories were set to the conservative 10.5 mT/m and 120 mT/m/ms, respectively, in order to avoid any image artifacts due to gradient imperfections. With a TR = 1.5s, the total scan time of the 2-shot acquisition was 13.5 minutes (6.75min / average). The echo time, defined as the distance between the peak of the RF and the start of the ADC window, was measured to be ≈13ms and (13 - $\tau_{4spokes}/2$) ≈ 12.28ms for the first and second average, respectively.

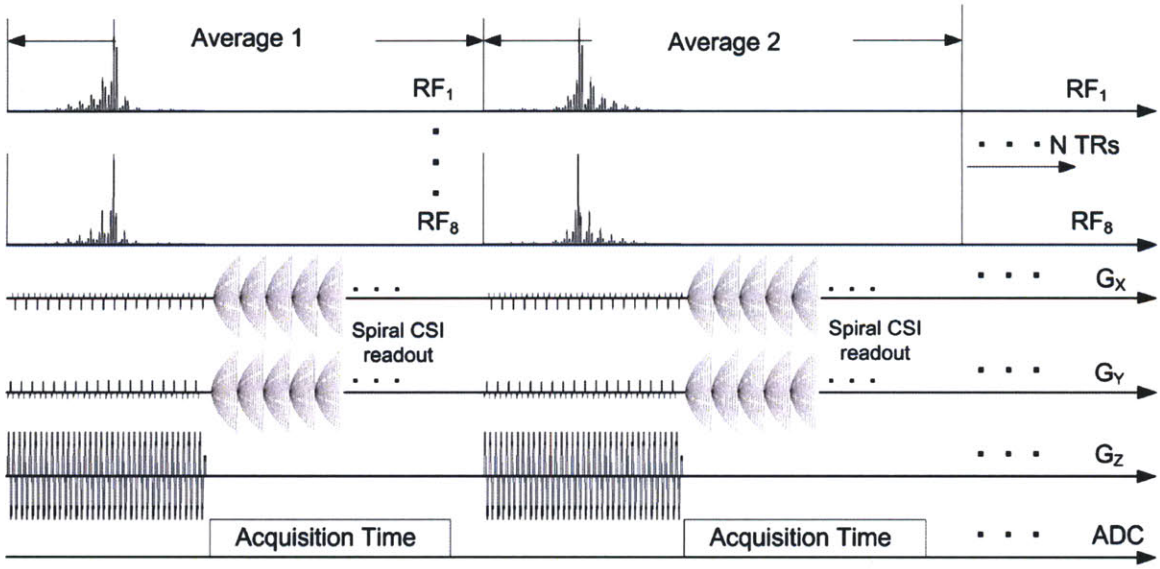

Figure 7-4: The timing diagram for the GRE, spiral CSI, 2-shot spectral-spatial pTx acquisition. The SS RF pulses played on the eight transmit channel were followed by a fast 3D CSI readout using spiral k-space trajectories. The overall voxel sizes was 0.59cc, and with TR = 1s, the total imaging time for the 2-shot acquisition was 13.5 minutes (6.75 / average). The TE (measured from the peak of the pulse to the start of the ADC) was measured to be ~13ms for the first average and ~12.28ms for the second average.

The spectroscopic data for each time point from the 8 coil elements of the dedicated receive array were combined by point wise multiplication of each of the estimated B_1^- profiles' conjugate. The resulting combined data set was then corrected for the spatial receive inhomogeneities by division by the sum of squares of the eight B_1^- profiles. The overall reconstruction was implemented using the spiral CSI package described in **Error! Reference source not found.**. Lastly, all of the CSI acquisitions were repeated using the mentioned 2-shot spectral-spatial BC excitation, which served as a comparison case for the 2-shot spectral-spatial 4-spoke excitation.

7.3 Results

In order to show the feasibility of the 2-shot spectral-spatial 4-spoke excitation at high SNR, spiral CSI data was acquired with different shifts in the carrier frequency for the excitation pulse on a single peak water phantom. Figure 7-5 and Figure 7-6 show the results of these acquisitions. All images shown come from the middle slice of 3D volumetric spiral CSI acquisitions, where the system's frequency was manually shifted to: 1. -180Hz (choline range), -120Hz (creatine range) and 180Hz (NAA range), shown in Figure 7-5; and 2. -620Hz (residual water range) and 400Hz (residual 1.3ppm lipid range), shown in Figure 7-6. All the images were obtained by summing the signals' magnitude in the vicinity (±100Hz) of the said frequencies, followed by correction of the remaining receive inhomogeneities using the previously estimated B_1^- profiles.

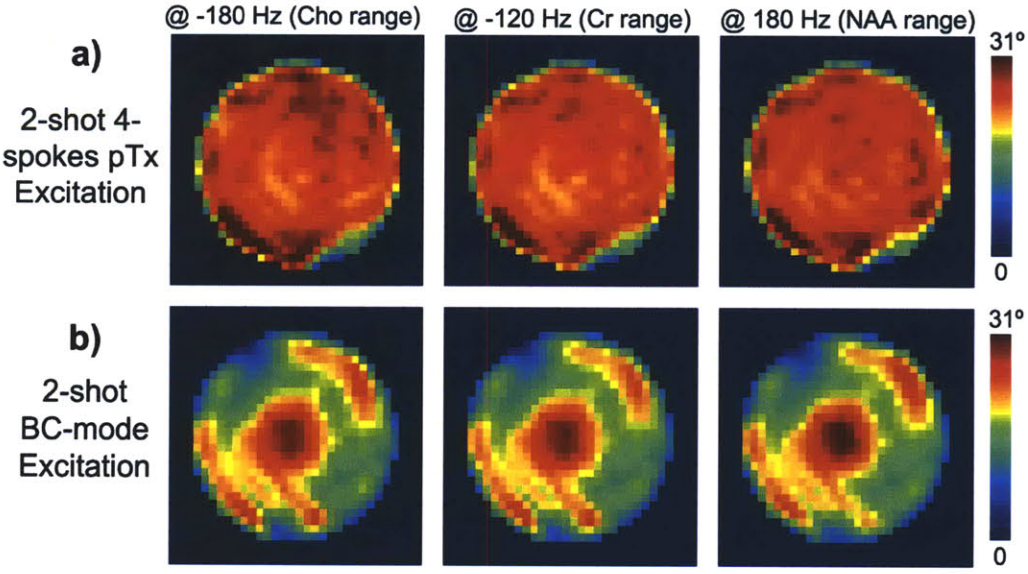

Figure 7-5: Images from the middle slice of a 3D volumetric spiral CSI acquisitions using *a)* the 2-shot spectral-spatial 4-spoke excitation and *b)* the 2-shot spectral-spatial BC excitation, demonstrating dramatically inferior spatial mitigation capabilities of the latter. For each of the acquisitions, the system's frequency was manually shifted to: -180Hz (choline range), -120Hz (creatine range) and 180Hz (NAA range). The Images were obtained by summing the magnitude of signals in the vicinity of the mentioned frequencies followed by division by the (receive) B_1^- profile;

Figure 7-5a and Figure 7-5b show images acquired at the three mentioned off-resonances of the spectral passband using the 2-shot spectral-spatial 4-spoke and BC excitation, respectively, clearly demonstrating the superiority of the former in terms of spatial uniformity. A quantitative measure of their performance is given in **Error! Reference source not found.**, showing the percentages of the voxels that deviate less than 10% and 30% (second and third row, respectively) of each image's mean. Specifically, while ~92% of the voxels in the images shown in Figure 7-5a deviate less than 10% from their (individual) mean, that is the case for ~58% of the voxels in the images shown in Figure 7-5b. The third row gives the values of σ_{norm}, the normalized standard deviation across the entire volume of interest, and represents another metric for spatial uniformity. Note that these values correspond well with the ones shown in Figure 7-3.

	Cho_{Fig7a}	Cr_{Fig7a}	NAA_{Fig5a}	Cho_{Fig7b}	Cr_{Fig7b}	NAA_{Fig7b}
$\varepsilon < 10\%$	91.5%	92.3%	93.2%	56.8%	59.1%	57.5%
$\varepsilon < 30\%$	98.1%	98.4%	98.7%	91.4%	92.5%	91.5%
σ_{norm}	5.91%	5.85%	5.66%	19.59%	19.42%	19.55%

Table 4: Evaluating the B_1^+ mitigation of the metabolites maps acquired with the 2-shot spectral-spatial 4-spoke (Figure 7-5a) and BC (Figure 7-5b) excitation. Comparing the percentages of the voxels that deviate more than 10% and 30% (second and third row, respectively), it can be seen that 2-shot spectral-spatial 4-spoke excitation, clearly outperforms the BC equivalent design. This can also be concluded by looking at the values of the normalized standard deviation (σ_{norm}) for each of the images shown

Figure 7-6 demonstrates the feasibility of the proposed excitation in suppressing the water and lipid resonances. The top images of Figure 7-6a and Figure 7-6b, show the pure sum (i.e. without any phasing) of the two average acquisitions, clearly indicating that if not properly phased, the 2-shot spectral-spatial 4-spoke excitation does not suppress the water signals. Note that the lower intensity around the lipid resonances is due to the fact that 1.3ppm is roughly between the passband and the first sidelobe of the spectral profile of each spectral-spatial pulse (see Figure 7-2a and Figure 7-2b for visual clarification). The seconds rows show exactly the same data, but with the proper phasing

of the first and second average acquisition. Finally, the top and bottom images in Figure 7-6c presents the ratio between the two sets of images in Figure 7-6a and Figure 7-6b, respectifully, showing that at least 96% of the residual water and at least 94% of the residual lipid frequencies have been successfully suppressed. Furthermore, μ_{water} = 2.32% and μ_{lipid} = 3.95% represent the mean values across the phantom for the water and lipid resonances, respectively. All the percentage values mentioned are calculated with respect to the full flip angle of 31^0 (shown in Figure 7-5).

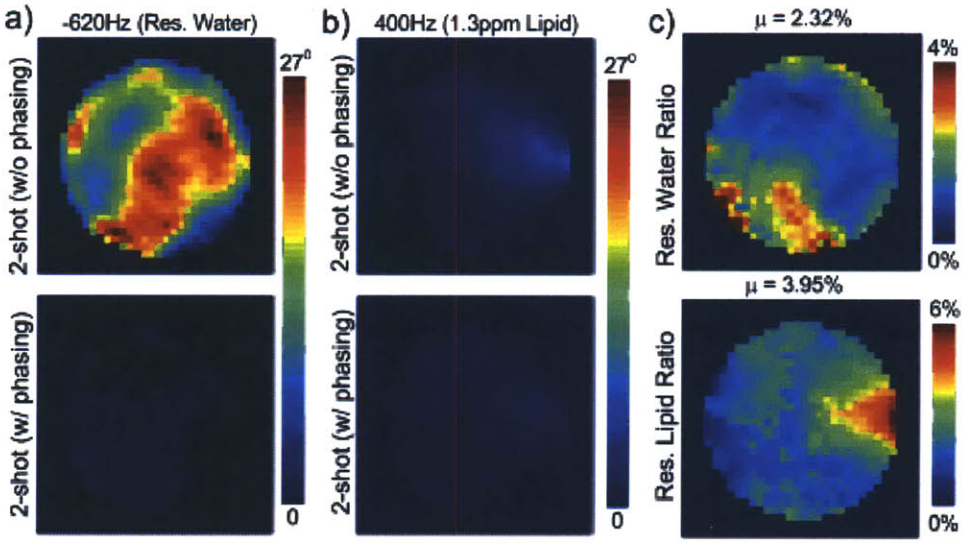

Figure 7-6: Images from the middle slice of a 3D volumetric spiral CSI acquisitions using the 2-shot spectral-spatial 4-spoke excitation. *a)* The system's frequency was manually shifted to: -620Hz (residual water range), and *b)* 400Hz (residual 1.3ppm lipid signals), and images were obtained by summing over the magnitude of the signals in the vicinity of the mentioned frequencies, followed by correction by the (receive) B_1^- profile; Top and bottom images show the simple sum, and the properly phased sum of the two acquired averages, respectively. Note that the lower intensity of the top image is due to the fact that 1.3ppm is roughly between the passband and the stop band of the spectral profile of each spectral-spatial pulse (i.e. from one average). The mean value was calculated to be 3.95%. c) The ratio between the top and bottom images from a) and b), showing more than 96% and 94% suppression of the water and lipid signals, respectively. The mean values of the top and bottom ratio images were 2.32% and 3.95%, respectively.

Verifying the feasibility of the excitation on a high SNR phantom was followed by testing its performance on a spectroscopy phantom containing physiological concentrations of the major brain metabolites. Figure 7-7a shows grids of magnitude spectra from particular spatial locations, displayed over the 1.75 ppm to 3.45 ppm (~500Hz) range. The water suppression was good enough, so that the quality of the metabolite peaks was not compromised. In terms of B_1^+spatial uniformity, the inferiority of the 2-shot spectral-spatial BC-RF excitation's (red spectra on the spectral grid) over the 2-shot spectral-spatial 4-spoke RF design (blue spectra on the spectral grid) is

clearly demonstrated, particularly when looking at the top right part of the phantom (right grid in Figure 7-7a).

Figure 7-7b shows the estimated B_0 map (bottom) and a full-width-half-maximum (FWHM) measure of the spectra from an on-resonance CSI acquisition using the 2-shot spectral-spatial 4-spoke excitation (top). In other words, the latter image shows an estimate of the line broadening of the water spectrum, and represents an indirect measure of the T_2* constant. As it can be seen, parts of the phantom (especially towards the edges) which have greater FWHM (i.e. greater T2* values) suffer from some signal loss, which can be observed in broadened linewidths and lower amplitudes of the metabolites peaks. This can be noticed on the blue spectra shown on the right spectral gird in Figure 7-7a. While the inherently long RF pulses are partly responsible for this signal loss, the major contributor of these effects is the relatively long TE time in combination with the somewhat large voxel sizes (0.59cc). The main point that needs to be made here however, is that these physical effects are present in both excitations, and this doesn't change the fact the 2-shot pTx 4-spoke design provides improved uniform mitigation compared to the 2-shot BC-RF one.

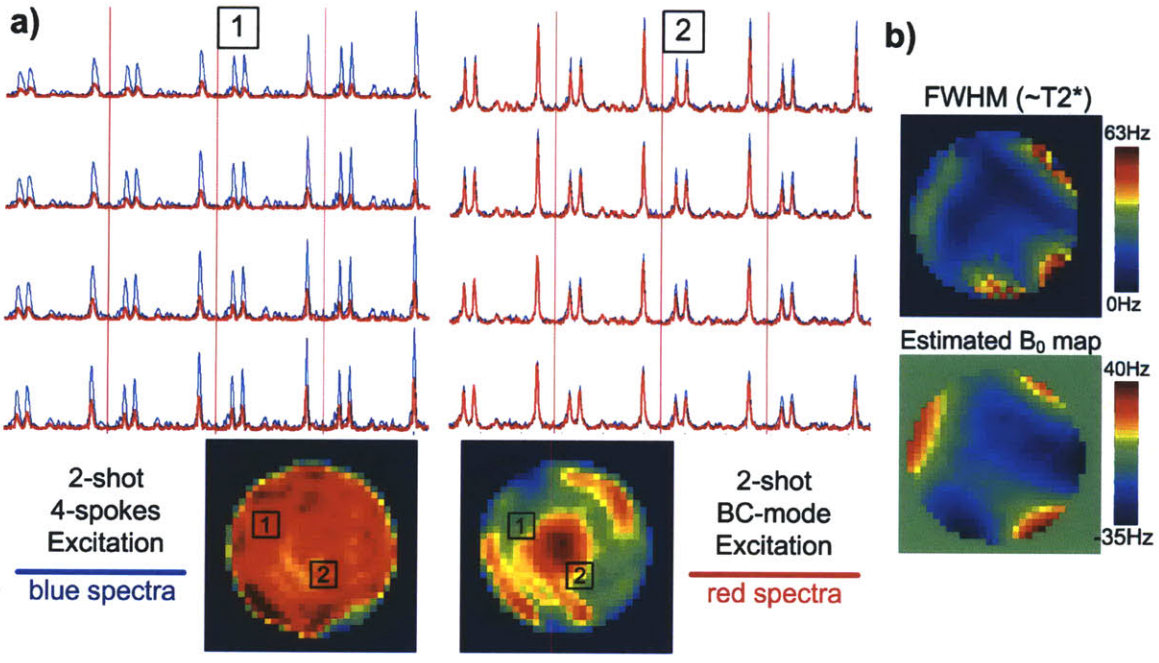

Figure 7-7: a) Magnitude spectra from the middle slice of the 3D spiral CSI acquisitions (TR=1s, TE ~ 13ms, voxel size = 0.59cc) from particular spatial locations of the spectroscopy phantom containing physiological concentrations of the major brain metabolites. Spectra from the 2-shot spectral-spatial 4-spoke design (shown in blue) demonstrate spatially more uniform excitation compared to the 2-shot spectral-spatial BC excitation (shown red); *b) (top)* The full-width-half-maximum (FWHM) measure of an on-resonance CSI acquisition using the 2-shot spectral-spatial 4-spoke excitation; This image shows an estimate of the line

broadening of the water spectrum, and represents an indirect measure of the T2* constant; *b) (bottom)* The estimated B_0 map.

7.4 Discussion and Conclusions

Our results demonstrate successful wideband B_1^+ mitigation in 7T CSI with parallel transmission for the center part of a 2.5-cm thick axial slab over ~450Hz of spectral bandwidth, enough to mitigate the major brain metabolite of interest at 7T. In addition to this, the proposed RF design also suppresses most of the strong water (more than 96%) and lipid resonances (more than 94%). The methods were applied on a high SNR single-peak phantom, and in a spectroscopy phantom containing physiological concentrations of the major brain metabolites. The 2-shot spectral-spatial 4-spoke design yields greatly improved spatial-spectral uniformity across the entire excited slice, and performs significantly better than the 2-shot spectral-spatial BC equivalent excitation.

The proposed RF design presents a novel method for designing spectral-spatial RF pulses, for the case when the duration of the spatially selective sub-lobes violates the Nyquist rate of the temporal envelope that determines the desired spectral excitation bandwidth. In the proposed approach, the given temporal envelope is divided into "even"- and "odd"-sample waveforms, that are then used to create two spectral-spatial pulses, played in two separate averages. When properly phased and summed, the acquired data from the two averages yields excitation that has the spectral profile of the original, not-undersampled time envelope. This benefit of the proposed approach comes at the cost of doubling the acquisition times. However, using the highly time-efficient spiral CSI readout schemes, the overall scan times for 3D volumetric acquisitions can be easily kept well below 15 minutes (TR = 1.5s), which is a reasonable scan time for *in vivo* acquisitions.

It is worth noting that the processing of the data from the two acquired averages included an extra step in addition to the phasing described in Figure 7-2. In order to reach better water suppression, the resonances around the residual water from the two averages have to be the exact opposite of each other. To correct for some of the inherent mismatches from one TR to the next, each spectrum of the second average was multiplied by a term in the form of $\alpha \cdot \exp(i \cdot \Delta\varphi)$, where α = [0.99-1.01] and $\Delta\varphi$ = [-5^0 – 5^0] so that the magnitude of the added signals *around the residual water frequencies* is as small as possible. This post-processing step improved the water suppression

relative to its maximum peak value by at most 1%, and did not alter the quality of the metabolites' distributions. Given the orders of magnitude concentration differences between the water and the metabolites signals, this 1% improvement can, in some cases, realistically improve the quality of the spectra. However, even with this additional step, the water suppression at some spatial locations was measured to be as low as ~4% (Figure 7-6), which is ~7 times worse compared to the sub-1% suppression predicted by the Bloch simulations (Figure 7-3). We believe that this mismatch is due to some higher order effects caused by systems' imperfections (RF and/or gradient). Nevertheless, as seen in Figure 7-7, the quality of the spectra is not hindered by any unsuppressed water signals.

Additional limitations that are beyond the RF design methods include the hardware limitation on each of the eight RF power amplifiers, which are capable of playing at most 200V of RF excitation. Overcoming this constrain would not only allow achievement of full 90^0 flips, but also permit the development of 180^0 refocusing pulse for spin-echo acquisitions. The spin-echo acquisitions are especially important when trying to overcome the signal degradations due to T_2* effects, which as seen in Figure 7-7, can be particularly severe at some parts of the volume of interest. Furthermore, the addition of the refocusing pulse in the excitation scheme will also provide improvement of the suppression of the signals in the stopband of the spectral profile, and therefore achieve superb suppression of the strong water signals.

Moreover, pushing the gradient coils to their limits (maximum gradient amplitude and slew rate limits of 80mT/m and 400mT/m/ms, respectively), would yield additional decrease in the RF durations, enabling spectral-spatial design with spatial sublobes that include more than 4 spokes. Using more than 4 spokes may become necessary at parallel transmission on ultra-high field strength systems for human imaging beyond 7T, e.g. 9.4T or higher. It is fair to note however, that for the cases when the magnitude B_1^+ non-uniformity is less than then 2.5-to-1 (maximum-to-minimum), a robust spatial B_1^+ mitigation is possible with 3 spokes, or in some case with even 2 spokes. Additionally, pushing the gradient limits would also provide the opportunity to achieve thinner and sharper slices, so that single-slice CSI acquisitions are sufficient to encode the excited volume.

As already mentioned throughout this thesis, the dominant constraint that prevents the employment of these techniques to *in vivo* measurement, is the estimation and

monitoring of the specific absorption rate (SAR) for pTx systems. The methods in **Error! Reference source not found.** outline the methods and workflow for future systems of local SAR estimation and real-time waveform monitoring, which we expect to become core elements in the deployment of in vivo spectroscopic imaging with parallel transmission.

THIS PAGE INTENTIONALLY LEFT BLANK

Chapter 8

Summary and Recommendations

8.1 Summary

Spectroscopic imaging at 7T allows for better metabolites' detection due to the intrinsically improved SNR and increased frequency dispersion compared to lower field systems. However, these benefits come at the cost of increased RF inhomogeneities causing undesirable non-uniform image contrast and SNR distribution. Eight channel parallel transmit system at 7T was used to design the RF excitations that, not only corrected for the B_1 non-uniformities, but also enhanced the excitation part of a typical 7T CSI experiment in terms of providing novel means for suppressing both the water and lipid signals. However, employment of these pTx excitations *in vivo* requires estimation and monitoring of the local SAR limits, in order to assure patient safety. Part of the work in this thesis was dedicated to the development and implementation of a real time RF monitoring system capable of detecting sporadic RF mishaps, and stopping the acquisition in real time if the transmission errors observed were estimated to violate assumptions of local SAR estimation. Furthermore, the contributions to the readout design of a CSI experiment included the full implementation of the spiral CSI algorithm [67] on Siemens MR scanners, enabling a routine use of the time-efficient spiral CSI for clinical applications.

More details on the specific contributions are summarizes below. All in all, the work in this thesis presented:

- The full implementation of the spiral CSI algorithm on Siemens's MR platforms, resulting in the release of a Work In Progress (WIP) package (**Error! Reference source not found.**). For a given set of user-defined imaging parameters, this package designed constant density k-space spiral trajectories in real time, acquired the non-uniformly sampled CSI data, and used 2X gridding to reconstruct the spectroscopic data onto Cartesian grids in time efficient manner. Installing this package on clinical Siemens MR scanners, made it possible to acquire volumetric CSI data sets on different patient populations. Preliminary studies are currently underway, exploring metabolite distributions in patients suffering from Late-Onset Tay Sachs (LOTS), X-linked adrenoleukodystrophy (ALD), and brain tumors.
- The development and implementation of real time RF monitoring system for pTx using directional couplers measuring the forward and reflected power to the transmit coil array (**Error! Reference source not found.**). The proposed threshold algorithm triggered acquisition stop (shutdown time ~10ms), if the monitored RF waveforms deviated from the ideal to a level that was considered to compromise patient's safety in terms of local SAR. The cut-off values used in the threshold algorithm were found empirically by monitoring the signals in 15 *in vivo* measurements. It was shown that the monitoring system successfully detected several kinds of purposely induced disturbances, including: 1. random phase jumps on any TX-channel; and 2. Coil tuning change on any transmit coil element.
- The design of a pTx-variant of the conventional CHESS excitation scheme, which compared to conventional CHESS designs, provided a factor of 2 improved suppression of the water signals (Chapter 6). The pTx-CHESS preceded the pTx wideband spokes excitation which provided uniform spatial mitigation over 600Hz of spectral BW, as shown by PE CSI acquisitions applied on a spectroscopic phantom containing the physiological concentrations of the major brain metabolites.
- The design of a 2-shot spectral-spatial pTx RF excitation that simultaneously provided both uniform mitigation over 450Hz of spectral BW, and suppression of the water and lipid signals (Chapter 7). This interleaved excitation scheme comes at a cost of doubling the acquisition time, which is not a big issue when it is followed by the time-efficient spiral CSI readouts. Proper reconstruction, which matches the effective TE time from the two acquisitions of the first and second average, yields

water and lipid signals in quadrature to the desired metabolites, while keeping the metabolites in-phase, *at no SNR cost*.

While realistically, 7T pTx spectroscopic imaging is far from being routinely used in clinical settings, the work presented in this thesis makes fundamental and important contributions towards reaching this goal.

8.2 Recommendations

The methods and concepts presented in this thesis can be extended in several ways. Most of the suggestions for the future work presented below are directed towards additional improvement of the excitation part of the CSI experiment by taking further advantage of the extra degrees of freedom in the pTx RF design provided by the 8 TX-channels. Moreover, the ability to monitor the RF waveforms on each TX-channel in real time can be used not only to monitoring local SAR, but also to predict the quality of the RF excitation.

In general, RF pulse designs for CSI applications are posed as a 4D excitation problems. Achieving the desired spectral-spatial profile can be done with one, or a series of RF pulses in sequential excitations at the cost of increase in the minimum scan time. This approach is particularly well suited to fast spatial encoding via spiral CSI, whereas phase encoded acquisitions suffer from a long minimum scan time penalty. One way to improve the preparation pTx-CHESS module presented in Chapter 6, is by replacing the single-band frequency selective pulse with its dual-band equivalent, such that now the longitudinal components of *both the water and lipid signals* are inverted and properly suppressed prior to the excitation. Compared to the proposed pTx-CHESS, this design is more involved on two levels: 1. It has more complicated frequency profile, including two passbands (one for water, the other for lipid resonances) and one stopband (for the metabolites' spectral band); and 2. It has to account for multiple T_1 constants – several for different brain tissues, and couple for the lipid signals. Once designed, this enhanced, dual-band preparation module is followed by standard wideband excitation schemes [114]. Successful implementation of this idea for single-TX 3T CSI has been shown in [132], but extending it to 7T pTx would require some effort.

Another area of future work involves adding curved saturation-band pulse that precedes the current spectral-spatial excitation and fully pre-saturates the signal from the skull. In other words, the target excitation of this pulse would be the skull itself, and its main purpose would be to help the 2-shot spectral-spatial excitation to better suppress the residual lipid signals. Going back to the concepts presented in Chapter 7, note that minimizing the spectral transition band between the NAA and lipid peak would yield longer RF pulse durations, and therefore delay the effective TE, causing slightly pronounced T_2* effects. Also, shrinking the spectral passband would make the excitation less robust to B_0 inhomogeneities and endanger proper NAA detection and estimation. Therefore, any additional help received from the curved pre-saturation band pulse that suppresses the skull (i.e. lipid signal), would only help the excitation proposed in Chapter 7. It is important to stress however, that this curved saturation band excitation has to be wideband, i.e. it has to maintain the designed spatial profile (at least) around the spectral bandwidth that includes the lipid and metabolite frequencies. Otherwise, metabolites' signals inside the brain might be pre-saturated as well, which is off-course, undesirable.

To some extent, the performance of the pTx RF pulse design of the spatially curve-saturated excitation can be improved if the pTx experiment is conducted using the Butler matrix transformations of the transmit coil array [104]. In this case, the eight measured B_1^+ maps won't have localized patterns (as shown in Figure 4-2b), but rather more circular spatial distribution (as seen in Figure 6-3) [101]. Given the ring-like shape of the human skull, this alternative set of B_1^+ maps (modes) might pose fewer constraints on the pTx RF design, and would therefore potentially improve its performance.

In many cases, the reliability of the spectroscopic data in brain regions that are potentially interesting to explore, is compromised by increased susceptibility artifacts. Examples include CSI of the top part of the spinal cord, which is close to the nasal cavities, i.e. close to the border of air-tissue transition. Therefore, it would be interesting to explore the means to design wideband curved excitation, which would provide a "brain-only" spatial target across wide range of spectral bandwidth (e.g. 450Hz). In other words, the spatial region to be excited would be curved out such that it excludes the regions with high susceptibility. Note that achieving the spectral-spatial profile of this wideband 3D-spatially curved excitation would be extremely demanding on the pTx RF pulse design, even to a level that the desired target is unrealizable. However, successful

designs of even the simpler, 2D-spatially curved wideband excitation would be thought of as a great contribution to the field of pTx RF design, in general.

In terms of future work related to the materials presented in **Error! Reference source not found.**, one can potentially use the capabilities of the real time RF monitoring system as a way to predict the transmission quality of the pTx excitation. It would be interesting to find a correlation measure between: 1. the level to which the Bloch-simulated RF targets match the results obtained from the scanner; and 2. the level of mismatch between the monitored and ideal RF waveforms. More specifically, a hypothetical result of these calculations would for example say that, the quality of final images obtained from the scanner remains high (e.g. >99% of RMSE), as long as, (for example) less than 10% of the RF samples among all the monitored waveforms deviate at most 5% from the ideal pulse. This statistical analysis that links transmission quality to the deviation of the monitored RF waveform could be beneficial in terms of finding the extent to which the RF pulse design algorithms can relax the constraints posed on the RF's amplitude and phase values.

On a pTx system level, several improvements would be beneficial not only for pTx CSI related applications, but for pTx imaging in general. On the hardware side, the RF power amplifiers on our system, are currently capable of delivering 800W of power, resulting in a maximum transmit voltage of only 200V. High flip applications, like spin-echo, are impossible to realize for RF pulse designs like the one presented in Chapter 7, where the maximum duration of the 4-spokes subpulses has an upper limit (i.e. it may be VERSE-ed only to a certain level). On a software side, improvements have to be made on the time-efficiency of the workflow involved in a typical pTx experiment (**Error! Reference source not found.**). While our group has made great progress addressing this issue, RF pulse designs, and SAR calculations for a given pTx excitation can still take a long time, and therefore keep the subject in the scanner longer than needed. Improvements on this end might include implementations on the pTx RF pulse design and SAR calculation on graphical processing units (GPUs). Currently these are done in MATLAB® (MathWorks, Natick, MA, USA) and run on high-end CPUs.

More generally, particular attention should be paid on checking the feasibility of the methods dedicated to simulation of the electric (E) fields using standardized human models. For a given transmit coil array model, the calculated E fields should be fully trusted and cross-checked among the several currently available software packages.

Even if the simulations are thought to return trustworthy E fields, currently, the time needed to tune and match a particular coil array model and simulated the E fields on each transmit elements, is measured in days. Therefore, it would instructive to look into alternative numerical methods to simulate these fields – methods that are different from the two, currently most widely used ones: the finite-difference time-domain (FDTD), and the methods of moments (MoM). This is essential, due to the fact that, at this moment, the management of local SAR during pTx excitation is the biggest obstacle for routine *in vivo* measurements.

Chapter 9

Bibliography

1. Pfefferbaum, A., et al., *In vivo brain concentrations of N-acetyl compounds, creatine, and choline in Alzheimer disease.* Arch Gen Psychiatry, 1999. **56**(2): p. 185-92.
2. Mohanakrishnan, P., et al., *An in vitro 1H nuclear magnetic resonance study of the temporoparietal cortex of Alzheimer brains.* Exp Brain Res, 1995. **102**(3): p. 503-10.
3. Schuff, N., et al., *Changes of hippocampal N-acetyl aspartate and volume in Alzheimer's disease. A proton MR spectroscopic imaging and MRI study.* Neurology, 1997. **49**(6): p. 1513-21.
4. Klunk, W.E., et al., *N-acetyl-L-aspartate and other amino acid metabolites in Alzheimer's disease brain: a preliminary proton nuclear magnetic resonance study.* Neurology, 1992. **42**(8): p. 1578-85.
5. Chard, D.T., et al., *Brain metabolite changes in cortical grey and normal-appearing white matter in clinically early relapsing-remitting multiple sclerosis.* Brain, 2002. **125**: p. 2342-2352.
6. Cifelli, A., et al., *Thalamic neurodegeneration in multiple sclerosis.* Annals of Neurology, 2002. **52**(5): p. 650-653.
7. Adalsteinsson, E., et al., *Gray matter N-acetyl aspartate deficits in secondary progressive but not relapsing-remitting multiple sclerosis.* AJNR Am J Neuroradiol, 2003. **24**(10): p. 1941-5.
8. Rajanayagam, V., et al., *Proton MR spectroscopy of childhood adrenoleukodystrophy.* AJNR Am J Neuroradiol, 1996. **17**(6): p. 1013-24.
9. Tzika, A.A., et al., *Childhood adrenoleukodystrophy: assessment with proton MR spectroscopy.* Radiology, 1993. **189**(2): p. 467-80.

10. Eichler, F.S., et al., *Proton MR spectroscopic imaging predicts lesion progression on MRI in X-linked adrenoleukodystrophy.* Neurology, 2002. **58**(6): p. 901-7.

11. Nelson, S.J., *Multivoxel magnetic resonance spectroscopy of brain tumors.* Mol Cancer Ther, 2003. **2**(5): p. 497-507.

12. Dowling, C., et al., *Preoperative proton MR spectroscopic imaging of brain tumors: correlation with histopathologic analysis of resection specimens.* AJNR Am J Neuroradiol, 2001. **22**(4): p. 604-12.

13. Sijens, P.E., et al., *1H MR spectroscopy in patients with metastatic brain tumors: a multicenter study.* Magn Reson Med, 1995. **33**(6): p. 818-26.

14. Fulham, M.J., et al., *Mapping of brain tumor metabolites with proton MR spectroscopic imaging: clinical relevance.* Radiology, 1992. **185**(3): p. 675-86.

15. Negendank, W.G., et al., *Proton magnetic resonance spectroscopy in patients with glial tumors: a multicenter study.* J Neurosurg, 1996. **84**(3): p. 449-58.

16. Higuchi, T., et al., *Mapping of lactate and N-acetyl-L-aspartate predicts infarction during acute focal ischemia: In vivo H-1 magnetic resonance spectroscopy in rats.* Neurosurgery, 1996. **38**(1): p. 121-129.

17. Bruhn, H., et al., *Cerebral Metabolism in Man after Acute Stroke - New Observations Using Localized Proton Nmr-Spectroscopy.* Magnetic Resonance in Medicine, 1989. **9**(1): p. 126-131.

18. Graham, G.D., et al., *Proton Magnetic-Resonance Spectroscopy of Cerebral Lactate and Other Metabolites in Stroke Patients.* Stroke, 1992. **23**(3): p. 333-340.

19. Graham, G.D., et al., *Clinical Correlates of Proton Magnetic-Resonance Spectroscopy Findings after Acute Cerebral Infarction.* Stroke, 1995. **26**(2): p. 225-229.

20. Graham, G.D., et al., *Proton magnetic resonance spectroscopy of cerebral lactate and other metabolites in stroke patients.* Stroke, 1992. **23**(3): p. 333-40.

21. De Stefano, N., P.M. Matthews, and D.L. Arnold, *Reversible decreases in N-acetylaspartate after acute brain injury.* Magn Reson Med, 1995. **34**(5): p. 721-7.

22. Barker, P.B., et al., *Acute stroke: evaluation with serial proton MR spectroscopic imaging.* Radiology, 1994. **192**(3): p. 723-32.

23. Stanley, J.A., *In vivo magnetic resonance spectroscopy and its application to neuropsychiatric disorders.* Can J Psychiatry, 2002. **47**(4): p. 315-26.

24. Birken, D.L. and W.H. Oldendorf, *N-acetyl-L-aspartic acid: a literature review of a compound prominent in 1H-NMR spectroscopic studies of brain.* Neurosci Biobehav Rev, 1989. **13**(1): p. 23-31.

25. Miller, B.L., *A review of chemical issues in 1H NMR spectroscopy: N-acetyl-L-aspartate, creatine and choline.* NMR Biomed, 1991. **4**(2): p. 47-52.

26. Govindaraju, V., K. Young, and A.A. Maudsley, *Proton NMR chemical shifts and coupling constants for brain metabolites.* Nmr in Biomedicine, 2000. **13**(3): p. 129-153.

27. Ernst, T., R. Kreis, and B.D. Ross, *Absolute Quantitation of Water and Metabolites in the Human Brain .1. Compartments and Water.* Journal of Magnetic Resonance Series B, 1993. **102**(1): p. 1-8.

28. Kreis, R., T. Ernst, and B.D. Ross, *Absolute Quantitation of Water and Metabolites in the Human Brain .2. Metabolite Concentrations.* Journal of Magnetic Resonance Series B, 1993. **102**(1): p. 9-19.

29. Duyn, J.H., et al., *Multisection Proton Mr Spectroscopic Imaging of the Brain.* Radiology, 1993. **188**(1): p. 277-282.

30. Brown, T.R., B.M. Kincaid, and K. Ugurbil, *NMR chemical shift imaging in three dimensions.* Proc Natl Acad Sci U S A, 1982. **79**(11): p. 3523-6.

31. Haase, A., et al., *1H NMR chemical shift selective (CHESS) imaging.* Phys Med Biol, 1985. **30**(4): p. 341-4.

32. Ogg, R.J., P.B. Kingsley, and J.S. Taylor, *WET, a T1- and B1-insensitive water-suppression method for in vivo localized 1H NMR spectroscopy.* J Magn Reson B, 1994. **104**(1): p. 1-10.

33. Hu, X.P., M. Patel, and K. Ugurbil, *A New Strategy for Spectroscopic Imaging.* Journal of Magnetic Resonance Series B, 1994. **103**(1): p. 30-38.

34. Plevritis, S.K. and A. Macovski, *Mrs Imaging Using Anatomically Based K-Space Sampling and Extrapolation.* Magnetic Resonance in Medicine, 1995. **34**(5): p. 686-693.

35. Haupt, C.I., et al., *Removal of lipid artifacts in 1H spectroscopic imaging by data extrapolation.* Magn Reson Med, 1996. **35**(5): p. 678-87.

36. Metzger, G., et al., *A hybrid technique for spectroscopic imaging with reduced truncation artifact.* Magn Reson Imaging, 1999. **17**(3): p. 435-43.

37. Adalsteinsson, E., et al., *Reduced spatial side lobes in chemical-shift imaging.* Magn Reson Med, 1999. **42**(2): p. 314-23.

38. Macovski, A., *Noise in MRI.* Magn Reson Med, 1996. **36**(3): p. 494-7.

39. Edelstein, W.A., et al., *The intrinsic signal-to-noise ratio in NMR imaging.* Magn Reson Med, 1986. **3**(4): p. 604-18.

40. Collins, C.M., et al., *Central brightening due to constructive interference with, without, and despite dielectric resonance.* Journal of Magnetic Resonance Imaging, 2005. **21**(2): p. 192-196.

41. Vaughan, J.T., et al., *7T vs. 4T: RF power, homogeneity, and signal-to-noise comparison in head images.* Magn Reson Med, 2001. **46**(1): p. 24-30.

42. Hoult, D.I. and D. Phil, *Sensitivity and power deposition in a high-field imaging experiment.* J Magn Reson Imaging, 2000. **12**(1): p. 46-67.

43. Howe, F.A., et al., *Proton spectroscopy in vivo.* Magn Reson Q, 1993. **9**(1): p. 31-59.

44. Bernstein, M.A., *Handbook of MRI Pulse Sequences.* 2004: Elsevier Academic Press

45. Nishimura, D.G., *Principles of magnetic resonance imaging.* 1996.

46. Bernstein, M.A., K.F. King, and Z. X.J., *Handbook of MRI Pulse Sequence.* 2004.

47. Gruetter, R., et al., *Localized in vivo 13C NMR spectroscopy of the brain.* NMR Biomed, 2003. **16**(6-7): p. 313-38.

48. Maudsley, A.A., et al., *Spin echo 31P spectroscopic imaging in the human brain.* Magn Reson Med, 1990. **14**(2): p. 415-22.

49. Hugg, J.W., et al., *Lateralization of human focal epilepsy by 31P magnetic resonance spectroscopic imaging.* Neurology, 1992. **42**(10): p. 2011-8.

50. Murphy-Boesch, J., et al., *Proton-decoupled 31P chemical shift imaging of the human brain in normal volunteers.* NMR Biomed, 1993. **6**(3): p. 173-80.

51. Kalinowski, H.O., Berger, S., Braun, S., *Carbon 13 NMR Spectroscopy*. 1991: John Wiley and Sons, New York, NY.

52. Luyten, P.R., et al., *Experimental approaches to image localized human 31P NMR spectroscopy.* Magn Reson Med, 1989. **11**(1): p. 1-21.

53. Mansfield, P., *Spatial mapping of the chemical shift in NMR.* Magn Reson Med, 1984. **1**(3): p. 370-86.

54. Macovski, A., *Volumetric NMR imaging with time-varying gradients.* Magn Reson Med, 1985. **2**(1): p. 29-40.

55. Sepponen, R.E., J.T. Sipponen, and J.I. Tanttu, *A method for chemical shift imaging: demonstration of bone marrow involvement with proton chemical shift imaging.* J Comput Assist Tomogr, 1984. **8**(4): p. 585-7.

56. Matsui, S., K. Sekihara, and H. Kohno, *High-speed spatially resolved NMR spectroscopy using phase-modulated spin-echo trains. Expansion of the spectral bandwidth by combined use of delayed spin-echo trains.* Journal of Magnetic Resonance, 1985. **64**: p. 161-171.

57. Twieg, D.B., *Multiple-output chemical shift imaging (MOCSI): a practical technique for rapid spectroscopic imaging.* Magn Reson Med, 1989. **12**(1): p. 64-73.

58. Guilfoyle, D.N., et al., *PEEP--a rapid chemical-shift imaging method.* Magn Reson Med, 1989. **10**(2): p. 282-7.

59. Bowtell, R., M.G. Cawley, and P. Mansfield, *Proton chemical-shift mapping using PREP.* Journal of Magnetic Resonance, 1989. **82**(3): p. 634-639.

60. Doyle, M. and P. Mansfield, *Chemical-shift imaging: a hybrid approach.* Magn Reson Med, 1987. **5**(3): p. 255-61.

61. Haase, A., *Snapshot FLASH MRI. Applications to T1, T2, and chemical-shift imaging.* Magn Reson Med, 1990. **13**(1): p. 77-89.

62. Haase, A. and D. Matthaei, *Spectroscopic FLASH Imaging (SPLASH imaging).* Journal of Magnetic Resonance, 1987. **71**: p. 550-553.

63. Matsui, S., K. Sekihara, and H. Kohno, *High-speed spatially resolved high-resolution NMR spectroscopy.* Journal of the American Chemical Society, 1985. **107**: p. 2817-2818.

64. Webb, P., D. Spielman, and A. Macovski, *A fast spectroscopic imaging method using a blipped phase encode gradient.* Magn Reson Med, 1989. **12**(3): p. 306-15.

65. Adalsteinsson, E. and P. Irarrazabal, *Spectroscopic magnetic resonance imaging using spiral trajectories* 1997, The Board of Trustees of the Leland Stanford Junior University (Palo Alto, CA) USA.

66. Posse, S., et al., *High speed 1H spectroscopic imaging in human brain by echo planar spatial-spectral encoding.* Magn Reson Med, 1995. **33**(1): p. 34-40.

67. Adalsteinsson, E., et al., *Volumetric spectroscopic imaging with spiral-based k-space trajectories.* Magn Reson Med, 1998. **39**(6): p. 889-98.

68. Adalsteinsson, E., et al., *Three-dimensional spectroscopic imaging with time-varying gradients.* Magn Reson Med, 1995. **33**(4): p. 461-6.

69. Pauly, J.M., D.G. Nishimura, and A. Macovski, *A k-space analysis of small-tip-angle excitation.* J. Magn Reson., 1989. **81**(1): p. 43-56.

70. Moonen, C.T.W. and P.C.M. Vanzijl, *Highly Effective Water Suppression for Invivo Proton Nmr-Spectroscopy (Drysteam).* Journal of Magnetic Resonance, 1990. **88**(1): p. 28-41.

71. StarLack, J., et al., *Improved water and lipid suppression for 3D PRESS CSI using RF band selective inversion with gradient dephasing (BASING).* Magnetic Resonance in Medicine, 1997. **38**(2): p. 311-321.

72. Balchandani, P. and D. Spielman, *Fat suppression for 1H MRSI at 7T using spectrally selective adiabatic inversion recovery.* Magn Reson Med, 2008. **59**(5): p. 980-8.

73. Silver, M.S., R.I. Joseph, and D.I. Hoult, *Selective Spin Inversion in Nuclear Magnetic-Resonance and Coherent Optics through an Exact Solution of the Bloch-Riccati Equation.* Physical Review A, 1985. **31**(4): p. 2753-2755.

74. Rosenfeld, D. and Y. Zur, *Design of adiabatic selective pulses using optimal control theory.* Magnetic Resonance in Medicine, 1996. **36**(3): p. 401-409.

75. Rosenfeld, D., S.L. Panfil, and Y. Zur, *Design of adiabatic pulses for fat-suppression using analytic solutions of the Bloch equation.* Magnetic Resonance in Medicine, 1997. **37**(5): p. 793-801.

76. de Graaf, R.A. and K. Nicolay, *Adiabatic water suppression using frequency selective excitation.* Magnetic Resonance in Medicine, 1998. **40**(5): p. 690-696.

77. Hardy, C.J., W.A. Edelstein, and D. Vatis, *Efficient Adiabatic Fast Passage for Nmr Population-Inversion in the Presence of Radiofrequency Field Inhomogeneity and Frequency Offsets.* Journal of Magnetic Resonance, 1986. **66**(3): p. 470-482.

78. Rosenfeld, D. and Y. Zur, *A new adiabatic inversion pulse.* Magnetic Resonance in Medicine, 1996. **36**(1): p. 124-136.

79. Bottomley, P.A., *Spatial localization in NMR spectroscopy in vivo.* Ann N Y Acad Sci, 1987. **508**: p. 333-48.

80. Frahm, J., et al., *Stimulated Echo Imaging.* Journal of Magnetic Resonance, 1985. **64**(1): p. 81-93.

81. Frahm, J., et al., *High-Speed Steam Mri of the Human Heart.* Magnetic Resonance in Medicine, 1991. **22**(1): p. 133-142.

82. Tannus, A. and M. Garwood, *Adiabatic pulses.* NMR Biomed, 1997. **10**(8): p. 423-34.

83. Near, J., et al., *High-Field MRSI of the Prostate Using a Transmit/Receive Endorectal Coil and Gradient Modulated Adiabatic Localization.* Journal of Magnetic Resonance Imaging, 2009. **30**(2): p. 335-343.

84. Ordidge, R.J., et al., *Frequency offset corrected inversion (FOCI) pulses for use in localized spectroscopy.* Magnetic Resonance in Medicine, 1996. **36**(4): p. 562-566.

85. Kinchesh, P. and R.J. Ordidge, *Spin-echo MRS in humans at high field: LASER localisation using FOCI pulses.* Journal of Magnetic Resonance, 2005. **175**(1): p. 30-43.

86. Sacolick, L.I., D.L. Rothman, and R.A. de Graaf, *Adiabatic refocusing pulses for volume selection in magnetic resonance spectroscopic imaging.* Magn Reson Med, 2007. **57**(3): p. 548-53.

87. Garwood, M. and L. DelaBarre, *The return of the frequency sweep: designing adiabatic pulses for contemporary NMR.* J Magn Reson, 2001. **153**(2): p. 155-77.

88. Andronesi, O.C., et al., *Spectroscopic imaging with improved gradient modulated constant adiabaticity pulses on high-field clinical scanners.* J Magn Reson, 2010. **203**(2): p. 283-93.

89. Moonen, C.T.W., et al., *Proton Spectroscopic Imaging of Human Brain.* Journal of Magnetic Resonance, 1992. **98**(3): p. 556-575.

90. Block, W., et al., *Consistent fat suppression with compensated spectral-spatial pulses.* Magn Reson Med, 1997. **38**(2): p. 198-206.

91. Schick, F., *Simultaneous highly selective MR water and fat imaging using a simple new type of spectral-spatial excitation.* Magn Reson Med, 1998. **40**(2): p. 194-202.

92. Zur, Y., *Design of improved spectral-spatial pulses for routine clinical use.* Magn Reson Med, 2000. **43**(3): p. 410-20.

93. Meyer, C.H., et al., *Simultaneous spatial and spectral selective excitation.* Magn Reson Med, 1990. **15**(2): p. 287-304.

94. Beatty, P.J., D.G. Nishimura, and J.M. Pauly, *Rapid gridding reconstruction with a minimal oversampling ratio.* IEEE Trans Med Imaging, 2005. **24**(6): p. 799-808.

95. Cheng, J.Y., *Gradient Characterization in Magnetic Resonance Imaging*, in *Department of Electrical Engineering and Computer Science*. 2007, Massachusetts Institute of Technology: Cambridge.

96. Schirmer, T. and D.P. Auer, *On the reliability of quantitative clinical magnetic resonance spectroscopy of the human brain.* NMR Biomed, 2000. **13**(1): p. 28-36.

97. Navon, R., Z. Argov, and A. Frisch, *Hexosaminidase A deficiency in adults.* Am J Med Genet, 1986. **24**(1): p. 179-96.

98. Inglese, M., et al., *MR imaging and proton spectroscopy of neuronal injury in late-onset GM2 gangliosidosis.* AJNR Am J Neuroradiol, 2005. **26**(8): p. 2037-42.

99. Mountford, C.E., et al., *Neurospectroscopy: The Past, Present and Future.* Chemical Reviews, 2010. **110**(5): p. 3060-3086.

100. Ratai, E., et al., *Seven-Tesla proton magnetic resonance spectroscopic imaging in adult X-linked adrenoleukodystrophy.* Arch Neurol, 2008. **65**(11): p. 1488-94.

101. Alagappan, V., et al., *Degenerate mode band-pass birdcage coil for accelerated parallel excitation.* Magn Reson Med, 2007. **57**(6): p. 1148-58.

102. Alagappan, V., *RF Coil Technology for Parallel Excitation and Reception*

in High Field MRI, in *Electrical Engineering*. 2008, Tufts University: Medford.

103. Lee, J., *Fast multi-slice B1+ and B1- mapping in Parallel Transmit System at 7T with adaptive optimal data combination.* Magn Res Med, In preparation, 2010.

104. Setsompop, K., et al., *Slice-selective RF pulses for in vivo B1+ inhomogeneity mitigation at 7 tesla using parallel RF excitation with a 16-element coil.* Magn Reson Med, 2008. **60**(6): p. 1422-32.

105. Kerr, A., et al. *Self-Calibrated Transmit SENSE.* in *Proceedings of 14th Annual Meeting of ISMRM.* 2006. Seattle, Washington, USA.

106. Brunner, D.O., S. Schweizer, and K.P. Pruessmann. *Fast mapping of highly inhomogeneous RF fields.* in *Proceedings of 15th Annual Meeting of ISMRM.* 2007. Berlin, Germany.

107. Fautz, H.-P., et al. *B1 mapping of coil arrays for parallel transmission.* in *Proceedings of 16th Annual Meeting of ISMRM.* 2008. Toronto, Canada.

108. Yarnykh, V.L., *Actual flip-angle imaging in the pulsed steady state: a method for rapid three-dimensional mapping of the transmitted radiofrequency field.* Magn Reson Med, 2007. **57**(1): p. 192-200.

109. Katscher, U., et al., *Transmit SENSE.* Magn Reson Med, 2003. **49**(1): p. 144-50.

110. Zhu, Y., *Parallel excitation with an array of transmit coils.* Magn Reson Med, 2004. **51**(4): p. 775-84.

111. Grissom, W., et al., *Spatial domain method for the design of RF pulses in multicoil parallel excitation.* Magn Reson Med, 2006. **56**(3): p. 620-9.

112. Pruessmann, K.P., et al., *SENSE: sensitivity encoding for fast MRI.* Magn Reson Med, 1999. **42**(5): p. 952-62.

113. Setsompop, K., et al., *Magnitude least squares optimization for parallel radio frequency excitation design demonstrated at 7 Tesla with eight channels.* Magn Reson Med, 2008. **59**(4): p. 908-15.

114. Setsompop, K., et al., *Broadband slab selection with B1+ mitigation at 7T via parallel spectral-spatial excitation.* Magn Reson Med, 2009. **61**(2): p. 493-500.

115. *Center for Devices and Radiologic Health, Guidance for the submission of premarket notifications for magnetic resonance diagnostic devices.* Rockville, Food and Drug Administration, 1988.

116. *International Electrotechnical Commission. International standard, medical equipment—part 2: particular requirements for the safety of magnetic resonance equipment for medical diagnosis, 2nd revision.* Geneva: International Electrotechnical Commission, 2002. **601**: p. 2-33.

117. Graesslin, I., et al. *Real-time SAR Monitoring to ensure Patient Safety for Parallel Transmission Systems.* in *Proceedings of 15th Annual Meeting of ISMRM.* 2007. Berlin, Gernamy.

118. Gagoski, B., et al. *Real time RF monitoring in a 7T parallel transmit system.* in *Proceedings of 18th Annual Meeting of ISMRM.* 2010. Stockholm, Sweden.

119. Collins C. M., W.Z., and Smith M. B. . *A Conservative Method for Ensuring Safety within Transmit Arrays.* in *Proceedings of 15th Annual Meeting of ISMRM.* 2007. Berlin, Germany.

120. Mao, W., M.B. Smith, and C.M. Collins, *Exploring the limits of RF shimming for high-field MRI of the human head.* Magn Reson Med, 2006. **56**(4): p. 918-22.

121. Collins, C.M., et al., *Combination of optimized transmit arrays and some receive array reconstruction methods can yield homogeneous images at very high frequencies.* Magn Reson Med, 2005. **54**(6): p. 1327-32.

122. Vaughan, T., et al., *9.4T human MRI: preliminary results.* Magn Reson Med, 2006. **56**(6): p. 1274-82.

123. Saekho, S., et al., *Small tip angle three-dimensional tailored radiofrequency slab-select pulse for reduced B1 inhomogeneity at 3 T.* Magn Reson Med, 2005. **53**(2): p. 479-84.

124. Zelinski, A.C., et al., *Fast slice-selective radio-frequency excitation pulses for mitigating B+1 inhomogeneity in the human brain at 7 Tesla.* Magn Reson Med, 2008. **59**(6): p. 1355-64.

125. Pauly, J., et al., *Parameter relations for the Shinnar-Le Roux selective excitation pulse design algorithm [NMR imaging].* IEEE Trans Med Imaging, 1991. **10**(1): p. 53-65.

126. Conolly, S., et al., *Variable-rate selective excitation.* J. Magn Reson., 1988. **78**: p. 440-458.

127. Balchandani, P., J. Pauly, and D. Spielman, *Interleaved narrow-band PRESS sequence with adiabatic spatial-spectral refocusing pulses for 1H MRSI at 7T.* Magn Reson Med, 2008. **59**(5): p. 973-9.

128. Avdievich, N.I., et al., *Short echo spectroscopic imaging of the human brain at 7T using transceiver arrays.* Magn Reson Med, 2009. **62**(1): p. 17-25.

129. Spielman, D., et al., *Spectroscopic imaging with multidimensional pulses for excitation: SIMPLE.* Magn Reson Med, 1991. **19**(1): p. 67-84.

130. Hardy, C.J., W.A. Edelstein, and D. Vatis, *Efficient adiabatic fast passage for NMR population-inversion in the presence of radiofrequency field inhomogeneity and frequency offsets.* J. Magn Reson., 1986. **66**: p. 470-482.

131. Gold, G.E., et al., *MR spectroscopic imaging of collagen: tendons and knee menisci.* Magn Reson Med, 1995. **34**(5): p. 647-54.

132. Gu, M. and D.M. Spielman, *B1 and T1 Insensitive Water and Lipid Suppression Using Optimized Multiple Frequency-Selective Preparation Pulses for Whole-Brain 1H Spectroscopic Imaging at 3T.* Magnetic Resonance in Medicine, 2009. **61**(2): p. 462-466.